Observing and Manipulating Single Electrons Confined to Silicon Dangling Bond Ensembles with Non-Contact Atomic Force Microscopy

by

Wyatt Vine

A thesis submitted in partial fulfillment of the requirements for the degree of

Master of Science

Department of Physics

University of Alberta

Abstract

Non-contact atomic force microscopy (nc-AFM) is capable of inducing and resolving single-electron charge transitions of surface adsorbates. Here, these techniques are extended by studying the charge configurations of dangling bond (DB) ensembles on the hydrogen-terminated silicon surface. nc-AFM is used to monitor the location of single electrons confined to DB ensembles that are created *via* scanning tunnelling microscopy hydrogen lithography. Electrons are found to remain strongly localized to individual DBs, but occasionally switch sites. The dominant behaviour of these meta-stable charge configurations is a result of the Coulombic interactions between the confined electrons and relaxation of the silicon lattice. The application of charge sensing nc-AFM techniques to the characterization of field-controlled computing devices is explored. At zero applied bias voltage it is found that the charge of individual DBs can be selectively manipulated by controlling the tip's position, resulting in the ability to prepare specific charge configurations of larger DB ensembles. The ability to manipulate the charge state of individual DBs is a direct result of the total tip induced band bending, which has two components at zero applied bias voltage: the contact potential difference between the tip and sample, and the image charge induced in the tip. At small tip-sample separations the image charge component can become dominant, preferentially stabilizing electrons in the dangling bonds beneath the tip. The tip's influence is further characterized by investigating how it can cause unintentional changes to the ensembles' charge configuration, and by looking for evidence of a 'sweet-spot,' where the tip interacts weakly with the charge configurations. In addition to the charge manipulation experiments, sub-surface defects are investigated with $I(V)$ spectroscopy. Notably, negative differential resistance is observed on DBs patterned directly over low-conductance defects, suggesting that the DB and defect may hybridize.

Preface

Figures 4.3 and 8.1 have been taken from references [1] and [2], respectively.

Chapter 5, including figures and text, has been submitted for publication. The included version is available on the preprint server arXiv [3]. M.R., W.V., J.R., K.W., and R.W. conceived the experiments. M.R. and T.D. performed the experiments with input from T.H. and W.V.. W.V. analyzed the data. W.V., M.R. and T.D. prepared the manuscript. L.L. developed the model of the interaction between tip and surface. All authors reviewed and commented on the manuscript.

All other content is original. The experiments contained within Chapters 6 - 8 were performed jointly with M. Rashidi and T. Dienel.

Acknowledgements

My family and friends have routinely supported me, encouraged me, fed me, and made me laugh. I am especially grateful for my parents Fred and Karen. Over the past few years I have enjoyed coming to know them not only as my parents but as friends and mentors.

I am indebted to my former supervisors Tito Scaiano, Simon Trudel, and Belinda Heyne, without whom I would not have made it to grad school. I also sincerely appreciate the constructive feedback of my committee members: Dr. John Beamish, Dr. Frank Hegmann, and Dr. Michael Woodside.

I feel very fortunate to have been part of a great lab group. I owe a great deal to Martin and Mark who have helped me troubleshoot and fix innumerable things, always with a smile. I enjoyed many laughs and successes with my fellow grad students John, Erika, Roshan, Taleana, and Jeremy. I am especially grateful to Moe Rashidi and Thomas Dienel who have been generous with their time and friendships.

And finally I express my sincerest gratitude to my supervisor Robert Wolkow. Among his many great qualities I would be remiss not to highlight his generosity and sense of humour, but what I admire most about Bob is the profound joy he takes from learning. Bob routinely reminds his students that they should be having fun and always leads by example. It has been a true privilege to work with him.

Contents

List of Figures

Abbreviations

ADC	Analog to digital converter
BASiL	Binary atomic silicon logic
CPD	Contact potential difference
CB	Conduction band
DAC	Digital to analog converter
DB	Dangling bond
DFT	Density Functional Theory
DOS	Density of states
FPGA	Field programmable gate array
HOMO	Highest occupied molecular orbital
KPFM	Kelvin probe force microscopy
LDOS	Local density of states
LUMO	Lowest unoccupied molecular orbital
nc-AFM	Non-contact atomic force microscope
QCA	Quantum cellular automata
SPM	Scanning probe microscope
STM	Scanning tunnelling microscope
STS	Scanning tunnelling spectroscopy
TIBB	Tip induced band bending
TR-STS	Time-resolved scanning tunnelling spectroscopy
TSP	Titanium sublimation pump
UHV	Ultrahigh vacuum
VB	Valence band

Symbols

A	Amplitude
B	Bandwidth
ϵ_F	Fermi level
E_{vac}	Vacuum level
f_0	Resonant frequency
ϕ	Work function
Δf	Frequency shift
Q	Quality factor
k	Spring constant
k_B	Boltzmann constant
T	Temperature
V_{RMS}	Root mean square voltage
I_T	Tunnelling current
ρ	Density of states
M	Matrix element
$\hat{H}$	Hamiltonian
$\hbar$	Reduced Planck's constant
ψ	Wavefunction
z	Tip height or tip offset
Γ	Rate

1 Introduction

Scanning probe microscopes (SPM) are now indespensable tools in nanoscience and physics research programs. With the introduction of the scanning tunnelling microscope (STM) in 1982 [4], experimenters were granted unprecedented ability to study single molecules and atoms in real space. As an example of its potential, the inventors of STM, Binnig and Rohrer, quickly dispensed a long-standing problem by directly resolving the atomic structure of the Si(111) surface [5]. In the years since, STM has continued to make an impact across diverse research areas including superconductors [6, 7], magnetic materials [8, 9], and molecular [10] and atomic electronics [11].

In 1990 Schweizer and Eigler made a landmark advance when they demonstrated that the probe can also be used to directly manipulate the position of individual atoms and molecules on the surface [12]. This made it possible to use SPM techniques to directly engineer atomic devices [13, 14] and study tailored physical systems [15, 16].

One significant limitation of STM is that it requires the use of conductive substrates, so that a tunnelling current can be established. To overcome this challenge, Binnig invented the atomic force microscope (AFM) in 1986 [17]. Rather than use a tunnelling current to precisely map the surface, AFM relies upon the physical interactions between the probe and surface. Correspondingly, AFM can be used to study metals, semiconductors, and insulators. Of the several variations of AFM, non-contact AFM (nc-AFM) has emerged as the preferred version for precise atomic scale measurements [18].

It has long been established that AFM is capable of resolving the forces associated with single electron transitions [19]. This has been exploited to great effect, for example, by using the probe to study the transport of a two dimensional electron gas through a point contact [20], mapping the electrostatic potential of a sample by monitoring the occupation of a tip-induced quantum dot [21], and characterizing the Coulomb oscillations corresponding to the charging of a quantum dot [22].

In 2004 Repp *et al.* demonstrated the first controllable manipulation of the charge state of individual adatoms using voltage pulses applied *via* STM [23]. The distinguishing feature of this work was that, because the gold adatoms were supported by

a thin film of NaCl, both the neutral and negatively charged states of the adatoms remained stable. Upon changing the charge state of the adatom, the equilibrium positions of the NaCl atoms supporting the adatom shifted as a result of Coulombic interactions; in the case of a negatively charged adatom the positively charged sodium atoms were drawn towards the adatom, while the negatively charged chlorine atoms shifted away [23]. Recently, SPM was used to directly measure the energies associated with the reorganization of the NaCl lattice upon the charging of a molecule [24].

In 2009 Gross *et al.* demonstrated that nc-AFM could be used to directly distinguish the charge state of gold and silver adatoms [25]. The advance here was that, because charge manipulation and detection could be performed *via* AFM, a net tunnelling current was no longer required as with STM. To date, AFM charge manipulation experiments similar to Repp *et al.* and Gross *et al.* have been performed predominantly on randomly distributed adsorbates, with charge being transferred to or from the adsorbates *via* the probe or bulk. However, a better understanding of intermolecular charge transport would aid the study of molecular and atomic devices. Recently, Steurer *et al.* began exploration in this direction by demonstrating that nc-AFM charge manipulation techniques can be used to used to induce and monitor the transition of single electrons between closely-spaced molecules [26].

The original work of this thesis is mainly focussed on the use of nc-AFM to observe and control single electrons confined to atomically defined surface structures. Single electrons are observed to localize to individual atoms within larger structures as a result of lattice relaxation, but switch sites on the timescale of seconds. In contrast to the works mentioned above, these nanostructures were engineered from silicon dangling bonds on the hydrogen-terminated silicon surface. The motivation behind this material system is that dangling bonds are midgap states [27], and therefore avoid the requirement of thin insulating films to localize individual electrons. In addition, recent advancements in the patterning of dangling bonds [28–30] make it possible to design complex error-free structures *via* SPM.

The thesis is organized as follows: in Chapter 2 we will review the physics underlying STM and AFM. In Chapter 3 the essential components of our STM/AFM are reviewed. In Chapter 4 we will discuss the silicon (100) surface, with an emphasis on the physics of dangling bonds. Chapter 5 is a forthcoming publication we

have submitted on the topic of charge manipulation within dangling bond structures, and Chapters 6 and 7 contain additional discussion and follow-up experiments. In Chapter 8 I motivate the use of these AFM techniques for the characterization of technologically relevant nanostructures, by studying a Binary Atomic Silicon Logic (BASiL) gate. Chapter 9 contains work on a side-project focused on studying sub-surface dopants *via* STM. Finally, Chapter 10 is a conclusion and outlook.

2 | The Physics of Scanning Tunnelling Microscopy and Atomic Force Microscopy

2.1 | Scanning Tunnelling Microscopy

In STM the tip and sample can both be considered reservoirs of electrons connected in a circuit (Figure 2.1). Classically, there is no mechanism for current to flow between the reservoirs while the tip and sample are not in direct contact. Quantum mechanically, when the two are brought close to one another (typically < 1 nm) the overlap of the tip and sample's wavefunctions becomes appreciable, and electrons are capable of tunnelling between the reservoirs. By applying a bias voltage between the tip and sample, the net effect is a tunnelling current that flows from the high-energy system to the low-energy system.

Because the wavefunctions of both the tip and sample decay exponentially quickly over the vacuum barrier, STM is extremely sensitive to the tip-sample separation [4]. Indeed, the classic signature of STM is an expoential increase in the tunnelling current as the tip-sample separation is made smaller [4]. This is captured clearly in the following expression for the tunnelling current at 0 K:

$$I = C \int_{\epsilon_F - eV}^{\epsilon_F} \rho_{tip}(\epsilon)\rho_{sam}(\epsilon)M_{ave}^2(\epsilon)d\epsilon \tag{2.1}$$

where C is a constant, ϵ is energy, ρ_{tip} and ρ_{sam} are the density of states of the tip and sample, and M_{ave} is the average matrix element for the overlap of the tip and sample wavefunctions. The entire expression is integrated over the energy range ϵ_F to $\epsilon_F - eV$, where ϵ_F is the Fermi level of the tip, and V is the applied bias voltage. The exponential relationship between the tunnelling current and the tip-sample separation provides justification for why STM is capable of resolving atomic scale features: a disproportionate contribution of the tunnelling current flows through the tip's apex atom.

There is an important asymmetry present in the tunnelling current: the current flows from the occupied states of the high-energy system to the unoccupied states of

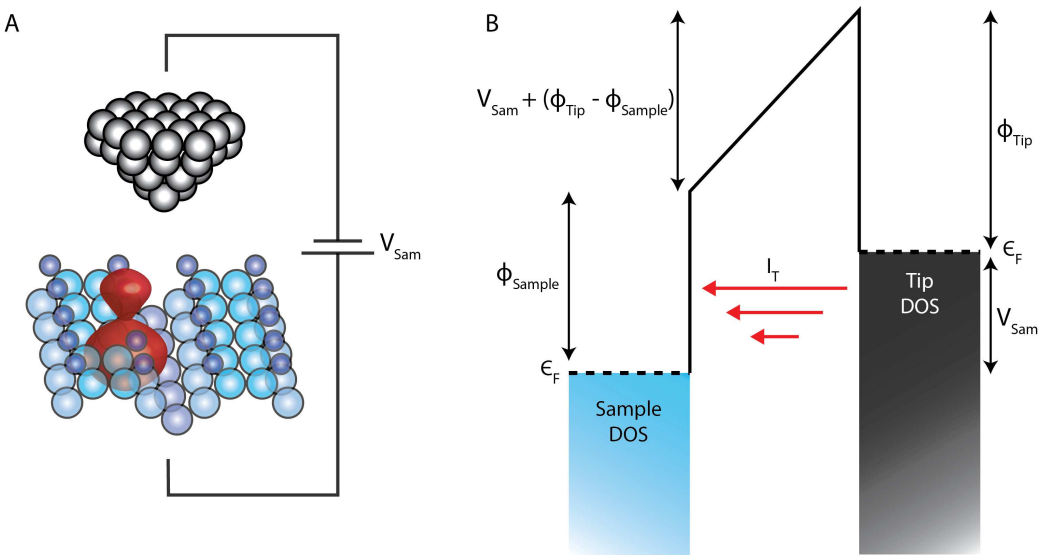

Figure 2.1: Schematic of an STM. (A) The simplest representation of an STM is of an atomically sharp tip held just above an atomic surface with an applied bias of V_{sam} between them. **(B)** The tunnelling current (I_T) arises from the overlap of the occupied states of the tip (those below ϵ_F) and the unoccupied states of the sample (or *vice versa*). The width of this overlap in energy depends on V_{sam} and the difference between the work functions of the tip and sample (ϕ_{Tip} and ϕ_{Sample}).

the low-energy system. In addition, because the number of occupied states can vary as a function of energy this suggests that the current achieved with a bias of +1 V may differ from a bias of −1 V. This is actually a powerful tool. First, it's important to note that when we refer to the bias voltage, it is more common to talk about the bias of the sample with respect to the tip [31]. Therefore, a tunnelling current at negative biases results from electrons in the filled states of the sample flowing to the empty states of the tip, and *vice versa*. Because the nanotips are typically made of metals, which have a large and nearly-constant density of states near the Fermi level, it is often assumed that the tunnelling current reveals information solely about the sample's density of states around its Fermi level [32], *i.e.* STM is sensitive to the HOMO and LUMO states of the sample. These aspects are described much more formally in what is known as Bardeen's Tunnelling Theory, which is described in the next section.

2.1.1 | Bardeen's Tunnelling Theory

Bardeen's Tunnelling Theory was first formulated in 1961, [33] two decades before the first STM was built [4]. It was developed for the more general problem of electrons tunnelling between two conductive materials separated via a thin insulator, a topical problem given the rise of semiconducting and superconducting devices in the preceding decade. Because of the success of Bardeen's Tunnelling Theory, others have since derived it *via* other complementary methods [34–37]. After the demonstration of the STM, Bardeen's theory was quickly applied to the problem by Tersoff and Hamann [38] and used to formalize the theory that describes the tunnelling current. The approach taken in this section is the classic approach, and I follow the tutorial published by Gottlieb and Wesoloski [32].

There are several main assumptions underlying the general approach [32]. 1) Tunnelling is weak so that a first order perturbative approach is sufficient. 2) The tip and sample states are nearly orthogonal. 3) All interactions between electrons can be ignored.[1] 4) The occupations of the tip and sample are independent and don't change as a result of the tunnelling current. 5) Both the tip and sample are in electrochemical equilibrium.

The first two are general assumptions used in perturbation theory. The third approximation is necessary to avoid solving a many-particle wavefunction. The final two permit us to further simplify the calculations by withdrawing the need to account for how the tunnelling current changes the wavefunctions of the tip and sample. This is reasonable given that the reservoir of electrons in both systems are very large relative to the tunnelling current.

The problem can be effectively split into three parts: first we will derive the rate at which an electron in the sample scatters to a given state of the tip. Second, we will sum this rate over all the states of the tip. Finally, we will take Fermi-Dirac statistics into account, and sum over all the eligible electrons to come up with the overall tunnelling current.

[1] This is justified in most cases, with a notable exemption being where single electron charging takes place [32]. Quantitative analysis of the tunnelling current is not undertaken in this thesis, and so reviewing Bardeen's Tunnelling Theory in depth remains helpful for clarifying the underlying physics.

Deriving the Scattering Rate

The general problem is to solve the Schrodinger's equation:

$$i\hbar\frac{\partial}{\partial t}\psi(\bar{r},t) = \hat{H}\psi(\bar{r},t) = \big(-\frac{\hbar^2}{2m}\nabla^2 + V(\bar{r},t)\big)\psi(\bar{r},t) \tag{2.2}$$

where $\psi(\bar{r},t)$ is the electron wavefunction and $V(\bar{r},t)$ is the potential the electron experiences. Because the potential $V(\bar{r},t)$ is in general complicated, Bardeen opted to split the Hamiltonian up piece-wise so that the tip and sample wavefunctions could be considered independently [33] (*ie.* $\hat{H} = \hat{H}_{sam} + \hat{H}_{tip}$). He also simplified the problem by using a static potential (*ie.* $V(\bar{r},t) = V(\bar{r})$).

His approach begins by considering an electron that remains confined to the sample state θ with energy ϵ. The wavefunction at time t is determined from the time-dependent Schrodinger equation:

$$i\hbar\frac{\partial}{\partial t}\theta(t) = \hat{H}_{sam}\theta(t) \tag{2.3}$$

$$\theta(t) = e^{-it\epsilon/\hbar}\theta(0) \tag{2.4}$$

In the case where the electron can scatter but the probability is small (in accordance with assumption 1) equation 2.4 should be a good approximation to the actual wavefunction ($\psi(\bar{r},t)$), but we must also include smaller amplitude components corresponding to the bound states of the tip (ϕ_k):

$$\hat{H}_{tip}\phi_k = E_k\phi_k \tag{2.5}$$

$$\psi(\bar{r},t) = e^{-it\epsilon/\hbar}\theta(0) + \sum_k a_k(t)\phi_k \tag{2.6}$$

Thus we must work to find the coefficients a_k which correspond to the probability amplitudes of the electron tunnelling from the sample state θ to the tip state ϕ_k. Because the electron originates in the sample we know that at $t = 0$ all a_k coefficients are zero.

Using this new form of ψ in the time dependent Schrodinger equation we find:

$$i\hbar\frac{\partial}{\partial t}\psi(\bar{r},t) = \hat{H}\psi(\bar{r},t) \tag{2.7}$$

The right half of equation 2.7 becomes:

$$\hat{H}\psi(\bar{r},t) = \hat{H}e^{-it\epsilon/\hbar}\theta(0) + \sum_k a_k\hat{H}\phi_k \tag{2.8}$$

$$= \epsilon e^{-it\epsilon/\hbar}\theta(0) + e^{-it\epsilon/\hbar}(\hat{H}-\hat{H}_{sam})\theta(0) + \sum_k a_k\big(E_k\phi_k + (\hat{H}-\hat{H}_{tip})\phi_k\big) \tag{2.9}$$

While the left half of 2.7 becomes:

$$i\hbar\frac{\partial}{\partial t}\psi(\bar{r},t) = \epsilon e^{-it\epsilon/\hbar}\theta(0) + i\hbar\sum_k \frac{d}{dt}a_k(t)\phi_k \tag{2.10}$$

By equating equation 2.9 with equation 2.10, taking the inner product of both sides with a tip state ϕ_j, and making use of orthogonality we find:

$$i\hbar\frac{d}{dt}a_j(t) = e^{-it\epsilon/\hbar}\left\langle\phi_j\right|\hat{H}-\hat{H}_{sam}\left|\theta\right\rangle + E_j a_j + \sum_k a_k(t)\left\langle\phi_j\right|\hat{H}-\hat{H}_{sam}\left|\phi_k\right\rangle \tag{2.11}$$

Now we make use of the fact that all a_k coefficients are zero or small for short periods of time (*i.e.* Bardeen's Tunnelling Theory is only valid for short periods of time). Under these conditions the third term of the previous equation drops out, allowing us to solve the differential equation for a_j which takes the form:

$$a_j(t) = \frac{e^{-it\epsilon/\hbar} - e^{-itE_j/\hbar}}{\epsilon - E_j}\left\langle\phi_j\right|\hat{H}-\hat{H}_{sam}\left|\theta\right\rangle \tag{2.12}$$

and therefore:

$$\left|a_j(t)\right|^2 = \frac{4\sin^2\left(t(E_j-\epsilon)/2\hbar\right)}{(E_j-\epsilon)^2}\left|\left\langle\phi_j\right|\hat{H}-\hat{H}_{sam}\left|\theta\right\rangle\right|^2 \tag{2.13}$$

This can be directly related to the transition probability given by $\left|\langle\phi_j|\psi(t)\rangle\right|^2$ by noting that:

$$\langle \phi_j | \psi(t) \rangle = a_j(t) + e^{-it\epsilon/\hbar} \langle \phi_j | \theta \rangle \approx a_j(t) \tag{2.14}$$

because the overlap of the tip and sample states is small according to assumption 2. The result of this part of the derivation is that an electron initially in the sample state θ scatters to the tip state ϕ_j at a rate of $\frac{d}{dt}\left|a_j(t)\right|^2$. The total rate at which this electron tunnels is therefore the sum of these rates for each tip state:

$$\frac{d}{dt}\sum_j \left|a_j(t)\right|^2 = \frac{d}{dt}\sum_j \frac{4\sin^2\left(t(E_j-\epsilon)/2\hbar\right)}{(E_j-\epsilon)^2}\left|\langle \phi_j | \hat{H} - \hat{H}_{sam} | \theta \rangle\right|^2 \tag{2.15}$$

It is important to note that in this derivation the assignment of the tip and sample states was arbitrary, and thus this derivation applies equally to the reverse process where an electron tunnels from the tip to the sample.

Summing Over Tip States - Fermi's Golden Rule

We now need to complete the sum in equation 2.15 to reveal the overall rate at which the electron tunnels to the tip. This can be achieved by using Fermi's Golden Rule[2]. It is important to note that to use Fermi's Golden Rule we must assume that density of states per unit energy is essentially constant on the scale h/t; assuming that this is true on the energy range of ~ 10 meV means that Bardeen's Tunnelling Theory will be accurate only on the timescale of a few picoseconds [32].

The sum in equation 2.15 can be reformulated as follows:

$$\sum_k P_t(E_k - \epsilon) M^2(\phi_k, \theta) \tag{2.16}$$

where $P_t(x) = \sin^2(tx/2\hbar)/x^2$ and $M^2(\phi_k, \theta) = \left|\langle \phi_k | \hat{H} - \hat{H}_{sam} | \theta \rangle\right|^2$. The latter quantity is known as the matrix element. It is essentially an integral that conveys the overlap of the tip and sample wavefunctions under the action of the Hamiltonian.

The function $P_t(x) \approx 0$ except in the small energy range $-2h/t < x < 2h/t$. This means that only states close in energy to ϵ will have appreciable contributions,

[2]Fermi's Golden Rule is a classic result which describes the transition rate of one energy eigenstate scattering into a continuum of other energy eigenstates.

allowing us to restrict the range of tip states we must sum over in equation 2.16. Note that this has a very significant physical interpretation: electrons tunnel elastically between the tip and sample.[3] Over such a small energy range the density of states the tip ($\rho_{tip}(E)$) will be approximately constant. Therefore the total number of tip states we must consider is:

$$N(\epsilon) = \int_{\epsilon-2h/t}^{\epsilon+2h/t} \rho_{tip}(E)dE \approx \frac{4h}{t}\rho_{tip}(\epsilon) \tag{2.17}$$

Let us now set:

$$\sum_k M^2(\phi_k, \theta) \approx \frac{1}{N(\epsilon)} \sum_{k\nmid |E_k-\epsilon|<2h/t} M^2(\phi_k, \theta) = M^2(\theta) \tag{2.18}$$

It follows that equation 2.16 can be rewritten as an integral over the small energy range of interest:

$$\sum_k P_t(E_k - \epsilon)M^2(\phi_k, \theta) \approx M^2(\theta) \sum_{k\nmid |E_k-\epsilon|<2h/t} P_t(E_k - \epsilon) \tag{2.19}$$

$$\approx M^2(\theta)\rho_{tip}(\epsilon) \int_{\epsilon-2h/t}^{\epsilon+2h/t} P_t(E)dE \tag{2.20}$$

$$\approx M^2(\theta)\rho_{tip}(\epsilon)\frac{2\pi t}{\hbar} \tag{2.21}$$

Returning this result back to equation 2.15 we find that the rate at which any given electron tunnels is constant and given by:

$$\Gamma_i = \sum_k P_t(E_k - \epsilon)M^2(\phi_k, \theta) \approx \frac{2\pi}{\hbar}M^2(\theta)\rho_{tip}(\epsilon) \tag{2.22}$$

Summing Over Eligible States - Fermi Dirac Statistics

To end up with the total tunnelling current we must sum Γ_i for all the electrons in the sample, but before completing this we must address two points. First, just as

[3] This is not strictly true, and inelastic tunnelling spectroscopy is used in STM (*e.g.* reference [39]), however, because in most situations the inelastic tunnelling accounts for only a small portion of the tunnelling current this assumption is often made in the derivation [32].

there is a tunnelling current flowing from the sample to the tip there is a tunnelling current flowing in the opposite direction. The net tunnelling current is therefore $I = I_{s\to t} - I_{t\to s}$.[4] Second, until now we have assumed that an electron tunnelling from the sample can end up in any eigenstate of the tip (or *vice versa*), but clearly this cannot be true because electrons must obey the Pauli Exclusion principle and therefore transitions to the occupied states of the tip are strictly forbidden.

$$F_{\mu,T}(E) = \frac{1}{e^{(E-\mu)/k_B T} + 1} \tag{2.23}$$

To account for this second point we must utilize the Fermi-Dirac distribution ($F_{\mu,T}(E)$), the function that describes the occupation of the energy eigenstates of a system with a given chemical potential (μ) and temperature (T) as a function of energy (E). Multiplying the tip's density of states by $1 - F_{\mu_t,T}(\epsilon)$ allows us to account for the number of unoccupied states available to the electron tunnelling from the sample. $F_{\mu_s,T}(\epsilon)$ can similarly be used to determine the number of occupied states of the sample, and therefore the number of electrons that may tunnel in the first place.

Combining these points we end up with an expression for the net tunnelling current:

$$I = \frac{2\pi e}{\hbar} \sum_n [F_{\mu_t,T}(\epsilon_n)\big(1 - F_{\mu_s,T}(\epsilon_n)\big) - \big(1 - F_{\mu_t,T}(\epsilon_n)\big)F_{\mu_s,T}(\epsilon_n)]\rho_{tip}(\epsilon_n)M^2(\theta_n) \tag{2.24}$$

Here we see reflected that the net tunnelling current is the difference between $I_{s\to t}$ and $I_{t\to s}$. The sum is carried out over all the eigenstates of the sample and takes into account all of the eigenstates of the tip *via* ρ_{tip}. The matrix element carries the information regarding rate of transitions for any given eigenstate of the sample. Finally, the multiplication of this large expression by the unit charge e converts it to a current.

This expression greatly simplifies when we consider the low temperature limit. At absolute zero $F_{\mu,0}(E)$ is a step function, with all the states $E < \mu$ occupied and all those greater in energy unoccupied.[5] Therefore the only states which contribute to

[4] By the bias convention mentioned earlier a positive conventional current flows from sample to tip

[5] This is of course the definition of the Fermi energy, μ_F.

the tunnelling current have an energy that lies between the chemical potentials of the tip and sample. In experiments, this difference is directly controlled by applying an electrical bias to the tip or sample (ie. $eV = \mu_s - \mu_t$). This allows us to rewrite equation 2.24 as:[6]

$$I = \pm\frac{2\pi e}{\hbar}\sum_{n:\mu_t\rightarrow\mu_t+eV}\rho_{tip}(\epsilon_n)M^2(\theta_n) \tag{2.25}$$

An equivalent but more intuitive form replaces the sum over each eigenstate of the sample with an integral over energy. This requires that we substitute $M^2(\theta_n)$ with an average of $M^2(\theta_n)$ for a small energy range around ϵ_n multiplied by the sample's density of states:

$$I = \pm\frac{2\pi e}{\hbar}\int_{\mu_t}^{\mu_t+eV}\rho_{tip}(\epsilon)\rho_{sam}(\epsilon)M^2_{ave}(\epsilon)d\epsilon \tag{2.26}$$

This expression clearly reveals the three main components that dictate the magnitude of the tunnelling current: the applied bias; the density of states of both the tip and sample; and the effective overlap of the tip and sample states. While equation 2.26 is only valid at 0 K it remains an excellent approximation for our low temperature experiments because the number of free carriers in a semiconductor at low temperatures is small.

2.1.2 | Modes of Operation

There are two natural modes of operation for STM [31]. The first and most intuitive is constant height mode. Here, the tip is scanned in a plane parallel to the surface and the signal is captured in the time-varying magnitude of the tunnelling current. The second is constant current mode. Here, the feedback control electronics remain engaged as the tip scans so that the signal is captured in the time-varying height of the tip. In both cases the signal is the convolution of the atomic-scale topography and local variations in the electronic density of states.

Constant current mode is safer because the tip is protected from crashing into the surface as a result of thermal drift, piezo-creep, or large changes in surface topography [31]. This mode is typically used to acquire large area scans which often take

[6] This sum assumes the sample is positively biased but the limits of the sum can easily be switched.

several minutes to acquire. Constant height mode is preferred for sensitive measurements for several reasons. First, our group works on a semiconductor. We routinely make measurements where the Fermi level of the tip is momentarily aligned within the band gap of our substrate; with the feedback control electronics engaged the tip would crash into the sample attempting to re-achieve the current setpoint. More fundamentally, constant height mode is preferred because it greatly simplifies interpretation. Consider bias-spectroscopy ($I(V)$), for example. Aside from taking 2D scans of the surface, this is the most common measurement taken with an STM. It involves holding the tip over a single location on the sample surface, sweeping the bias, and measuring changes in the tunnelling current. If the tip is held at a constant height, the changes in tunnelling current can be attributed solely to changes in the overlapping energy window of the tip and sample [31]. If the measurement were performed in constant current mode, however, the tip's height and therefore the tunnelling barrier would also be constantly changing, making it difficult to disentangle the changes in the electronic density of states.

There are two other common forms of scanning tunnelling spectroscopy (STS). In $I(z)$ spectroscopy the bias is held constant but the tip-sample separation is swept. In most cases this simply results in an exponential increase to the tunnelling current as the tip approaches due to the decreasing width of the tunnelling barrier [31]. In some cases, however, it can reveal very interesting physics (*e.g.* reference [40]). Differential conductance spectroscopy ($dI(V)/dV$) is performed by applying a small amplitude AC component to the bias during $I(V)$ spectroscopy and measuring the corresponding AC response in the tunnelling current using a lock-in amplifier.[7] The reason for this is clear when examining equation 2.26:

$$dI/dV \propto \rho_{sam}(V) M^2_{ave}(V) \tag{2.27}$$

In STS the tip is typically assumed to have a constant density of states, such that the two sides of equation 2.27 are equal up to a multiplicative constant. Over small bias ranges near 0 V the matrix element may often also be approximated as a constant [32], in which case $dI(V)/dV$ spectroscopy can be used as an approximate

[7] It can also be obtained by numerically differentiating an $I(V)$ measurement, although the sensitivity is less.

method to directly measure the sample's density of states. Because the tunnelling current is localized directly beneath the apex of the tip, this in fact reveals the local density of states (LDOS). As a result, STS can be considered a family of powerful techniques allowing one to study the intricate relationship between atomic and electronic structure.

2.2 | Non-Contact Atomic Force Microscopy

There are many variations of AFM. For brevity and clarity only frequency-modulated non-contact AFM [41] is discussed in this thesis because it was the mode used in the lab.[8]

2.2.1 | Underlying Principles

In AFM a nanotip is mounted to a stiff cantilever and driven at its resonant frequency (f_0). Upon bringing the tip close to a surface, interactions between the tip and sample influence the cantilever's oscillation (Figure 2.2A). There are many different types of forces that can exist between the tip and surface. While the London dispersion force is short range ($F_{LD} \propto z^{-7}$) it nevertheless results in a large portion of the total interaction between the tip and sample because of the large number of atoms comprising both objects [18]. Longer range forces including ion-dipole, electrostatic, and magnetic forces can also be present depending on the materials of the tip and sample and the applied bias voltage [18]. One common qualitative description of the interaction between two neutral atoms is the Lennard-Jones potential, (Figure 2.2B) which has terms proportional to z^{-6} and z^{-12}, corresponding to London dispersion and chemical forces, respectively. At long ranges the overall potential is attractive, but with small interatomic separations the potential becomes highly repulsive, which is commonly attributed to the overlapping of the atomic orbitals.

Forces between the tip and sample can be classified as either conservative (elastic) or non-conservative (inelastic) [18]. The latter can arise from a number of distinct physical processes [42] including magnetic hysteresis [43] and resistive losses from the modulation of space charge in a semiconductor [44]. Present in all AFM experiments

[8] The interested reader is directed to a comprehensive review of AFM by Franz Giessibl in reference [18].

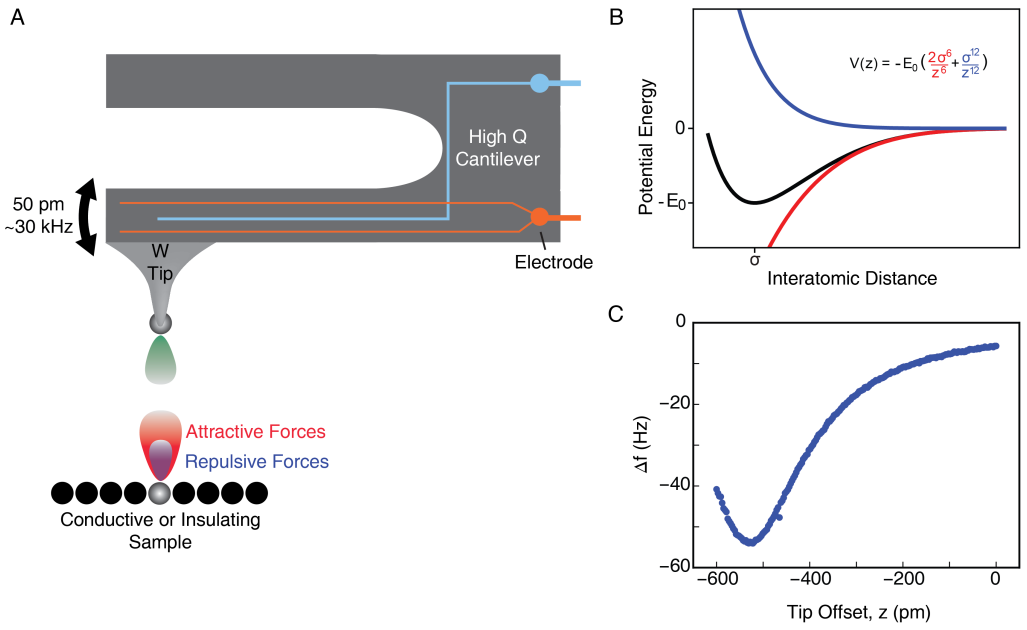

Figure 2.2: Schematic of an AFM. (A) An atomically sharp probe is affixed to a high Q cantilever and brought close to the surface. A Δf signal is produced due to the interactions between the probe and sample as the tip oscillates at a high frequency. **(B)** The Lennard-Jones potential is often used to model the potential energy associated with both short (blue) and long range (red) forces. E_0 is the bond energy, z is the tip-sample separation, and σ is the equilibrium bond distance. **(C)** An experimental $\Delta f(z)$ curve taken with a tungsten tip over H-Si. Note the similarity between the (B) and (C).

is internal dissipation of the cantilever. By using cantilevers with a high Q-factor ($Q = 2\pi E/\Delta E$) these losses can be safely ignored when using feedback controllers to control the oscillator's amplitude [18]. The experiments within this thesis were performed with q-Plus sensors with $Q > 10^4$. Furthermore, dissipative channels like those mentioned above are not expected to be present in the experiments here, and were not observed in the dissipation signal recorded. Consequently, we only need to consider the effect of conservative forces.

The effect of conservative forces can be modelled as a change in the effective spring constant of the cantilever, resulting in a shift of its resonance frequency (f). This frequency shift ($\Delta f = f - f_0$) is the primary signal used in nc-AFM. Figure 2.2C shows the Δf signal obtained as a tungsten nanotip was made to approach a hydrogen atom on the hydrogen-terminated silicon surface. There is a clear resemblance between this

measurement and the Lennard-Jones potential.

There are several aspects of AFM that make it more difficult to use than STM [18]. First and foremost is the technique's distance sensitivity. As we have already reviewed, in STM the tunnelling current drops off exponentially as the tip-sample separation grows. As a result, the signal in STM is localized almost exclusively to the tip's apex atom. In AFM, however, the Δf signal is a result of several different force components, each with a different strength and distance dependence. As a result, atoms on the tip and surface that are far from the apex can still contribute a measurable signal, making it more difficult to obtain a good SNR with AFM. The long range contributions can be seen directly in Figure 2.2C as the long tail in Δf, corresponding to the integration of the van der Waals forces between the tip and sample.

Second, in STM the tunnelling current always grows as the tip approaches, while in AFM the force gradient exerted on the tip can be positive, negative, or even first-order insensitive depending on the tip-sample separation. As a result, it is much more difficult to create a feedback control system to regulate the tip-sample separation in AFM [18]. To circumvent this issue we operate our AFM in constant height mode and intermittently recalibrate its height *via* STM.[9].

2.2.2 | Interpreting Δf

To establish a quantiative interpreation of the Δf signal we will begin by modelling the AFM cantilever as an ideal harmonic oscillator [45]. The corresponding Hamiltonian is:

$$\hat{H} = \frac{p^2}{2m^*} + \frac{kq'^2}{2} \tag{2.28}$$

where m^* is the effective mass of the cantilever, k is its spring constant, and q' is the position of the tip relative to its equilibrium position. The ground state solution of this equation is simply $q'(t) = A\cos(2\pi f_0 t)$, where A is the amplitude of the tip's oscillation.

As mentioned above, the conservative interactions between the tip and sample can

[9] This still requires the use of two control loops to regulate the oscillation amplitude and driving frequency.

be modelled effectively as a modification to the cantilever's spring constant ($k_{eff} = k+k_{int}$). The challenge with this approach, however, is that because there are multiple types of forces, each with different characteristic distances, k_{int} is in most cases not a simple correction term. Rather, k_{int} can vary orders of magnitude over a single oscillation cycle [18]. To account for this, many are forced to turn to approximate, methods like the perturbative approach developed by Giessibl [45].

An alternative approach is to purposefully restrict oneself to operating with small oscillation amplitudes ($A \approx 50$ pm) at a constant height. In this case, the change of k_{int} over the tip's range of motion is small, and k_{int} can be considered constant. In this case a simple form of Δf can be derived:

$$\Delta f = \frac{1}{2\pi\sqrt{m^*}}\left(\sqrt{k + k_{int}} - \sqrt{k}\right) \tag{2.29}$$

$$\Delta f = f_0\left(\sqrt{1 + k_{int}/k} - 1\right) \tag{2.30}$$

$$\Delta f \approx f_0 \frac{k_{int}}{2k} \tag{2.31}$$

Equation 2.31 clearly states that Δf is directly proportional to the force-gradient acting on the tip because $\partial F_{int}/\partial q' = -k_{int}$ [18]. This great simplification doesn't come for free though. In choosing to avoid functionalizing each interaction force's contribution we are prevented from quantitatively estimating their independent contributions to F_{int}. These estimations are possible when a more rigorous approach to functionalizing Δf is taken, but will not be necessary for this thesis.

In this thesis, the most important use of AFM is in sensing changes to the charge state of atoms beneath the tip, corresponding to changes in the electrostatic forces. By performing these experiments at a constant height and looking at variations in Δf we can confidently assign contrast in Δf to changes in the electrostatic force exerted on the tip; Van der Waals forces contribute to the magnitude of Δf but essentially remain constant and magnetic interactions between the tip and sample can be safely neglected.

Our ability to sense changes in the electrostatic environment is clearly dependent on the levels of noise suppression we can achieve. To set a theoretical upper-bound

on our sensitivity we consider two sources of noise to Δf: thermal noise ($\delta f_{thermal}$) and detector noise ($\delta f_{detector}$) [18]. The former is commonly estimated as the ratio between the thermal energy of the cantilever and the mechanical energy it stores, taking the form [41]:

$$\delta f_{thermal} = f_0 \sqrt{\frac{k_B T B}{\pi k A^2 f_o Q}} \tag{2.32}$$

where B is the bandwidth of the measurement. With typical operating parameters ($B = 100$ Hz, $k = 2$ kN/m, $A = 50$ pm, $f_0 = 30$ kHz, $Q = 25$ k) the thermal noise is approximately 0.02 Hz at 4.5 K and 0.2 Hz at 300 K. Detector noise arises from the amplification of the Δf signal by the pre-amplifier and has the form [46]:

$$\delta f_{detector} = \frac{n_{q'}}{\pi A} B^{3/2} \tag{2.33}$$

where $n_{q'}$ is the deflection noise density (100 fm $\text{Hz}^{-1/2}$) giving $\delta f_{detector} \approx 0.6$ Hz. The unfavourable scaling of $\delta f_{detector}$ with B means that even at room temperature detector noise is typically dominant [18, 46]. Because both noise contributions are independent they can be combined to create a total noise estimate (δf) [18], which for our operating conditions at 4.5 K is:

$$\delta f = \sqrt{\delta f_{thermal}^2 + f_{detector}^2} \approx 0.6 \text{ Hz} \tag{2.34}$$

This upper-bound on our sensitivity does not include contributions from vibration but it does agree well with the noise levels we see experimentally (≈ 1 Hz). Interestingly we note that both contributions to the noise scale with $1/A$. In our experiments, however, the sensitivity we could gain by operating with larger oscillation amplitudes is not worth sacrificing the benefits previously described.

2.2.3 | Kelvin Probe Force Microscopy

Kelvin Probe Force Microscopy (KPFM) [47] is the most common AFM spectroscopic technique used for mapping changes to the local electrostatic environment [48]. The basis of KPFM is that materials have different work functions ($\phi = E_{vac} - \epsilon_F$). When brought close to one another (but not necessarily into direct contact) the contact potential difference ($\phi_{CPD} = \phi_i - \phi_j$) causes charge to accumulate on both surfaces,

creating an electric field between the materials. Because AFM is sensitive to the electric field gradient, it can be used to map the local contact potential difference by recording Δf as a function of the bias between the tip and sample [49]. When the applied bias is equal and opposite to the contact potential difference there is no charge accumulation and Δf is minimized. The force is:

$$F_{es}(z) = \frac{(V_{sam} - \phi_{CPD})^2}{2} \frac{\partial C(z)}{\partial z} \tag{2.35}$$

where $C(z)$ is the capacitance between the tip and sample. Because $\Delta f \propto (V_{sam} - \phi_{CPD})^2$, KPFM measurements typically appear as parabolas whose apex corresponds to when $V_{sam} = \phi_{CPD}$.[10]

The reason KPFM is utilized so frequently in nanoscience is that it can be used to investigate single electron charging events [48, 49]. Consider placing the tip over a nanostructure and sweeping V_{sam}. At the point where the Fermi level of the tip sweeps past a discrete state of the nanostrucutre an electron will tunnel to or from the tip. This single electron charging event results in a change to the local CPD. Consequently the Δf signal jumps vertically from one parabola to another allowing one to measure the charge transition levels of the nanostructure.

[10]Note: we perform DC KPFM measurements. Another common method to measure the CPD is by superimposing an AC component on top of V_{sam} and using a lock-in amplifier to isolate the time-varying signal.

3 | Essential Components of a Low-Temp UHV Scanning Probe Microscope

Scanning probe microscopy has a rich history of innovation. Indeed, its emergence in 1981 [4] was only possible due to the confluence of many areas of research including physics, materials, and control electronics [31]. This chapter serves to review the most important technologies underlying the operation of our group's custom microscopes.

3.1 | Nanotips

Nanotips are, in essence, simply sharp pieces of wire. Despite their apparent simplicity, however, nanotips are among the most important components of a scanning probe microscope. For application in SPM nanotips are most-often made from tungsten or platinum iridium [31], but in recent years our group has also explored other materials [50]. Among the many methods to create nanotips [51–54] we use chemical etching [55] because of its reliability and simplicity. To chemically etch the tungsten nanotips used throughout this thesis, tungsten wires were situated as the cathode in an electrochemical circuit. Upon dipping the wire into into a solution of sodium hydroxide and establishing a DC current the tungsten is chemically removed from the shank of the wire. Crucially, the material is most efficiently etched at the surface of the solution, gradually thinning the wire near the meniscus to a waist. Eventually the weight of the submerged wire becomes too great for the thinning waist to sustain and it snaps, likely extruding the wire as it does so.

Before the nanotips can be used for SPM they must undergo further processing. To achieve this the nanotips are clamped to a tip holder (Figure 3.2A) and admitted to a dedicated chamber of the UHV system. First, they are resistively heated to approximately 800 °C in order to degas the tip and remove its oxide surface. Any organic contaminants either desorb or carbonize during this step. Second, the tips are subject to electron bombardment (e-beam). This is achieved by placing the tip close to a metal filament, resistively heating the filament so that electrons are thermionically emitted, and attracting them to the tip by applying a positive voltage

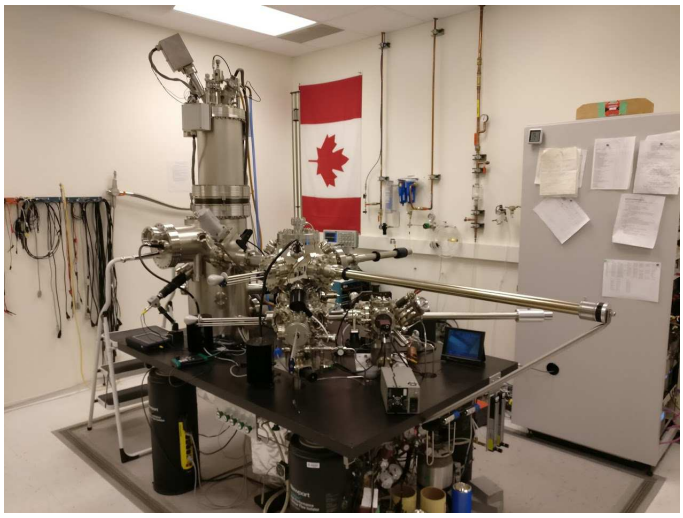

Figure 3.1: A customized Omicron LT STM-AFM.

to it. Because the electrostatic field is greatest at the sharp apex[1] it sources a large portion of the current. This results in intense local heating of the apex, which is used to ensure its cleanliness.

The quickest way to characterize a nanotip is to perform field emission, which is essentially the reverse process of e-beam. A positive voltage is applied to the filament and a negative voltage to the tip. Sharper tips emit current with smaller applied biases because the field is greater. Occasionally sustained field emission at small currents (< 10 nA) is found to further sharpen the tip, as evidenced by an increase in the field emission current while maintaining a constant bias voltage on the tip. This suggests that the large applied field may lead to a restructuring of the tip's apex.

A more robust characterization method frequently employed by our group is field ion microscopy [56]. The tip is positioned in front of an assembly of a micro-channel plate (MCP) and a phosphor screen. The former acts as an amplifier and the latter a spatially resolved detector for the ion current. An imaging gas with a high ionization energy (we use helium [57]) is admitted to the chamber at a modest pressure (1×10^{-6} Torr) and a large positive bias is applied to the tip. With sufficient field strengths the imaging gas is ionized by the tip and is subsequently accelerated by the field towards

[1] This is the key principle underlying the use of nanotips in most applications.

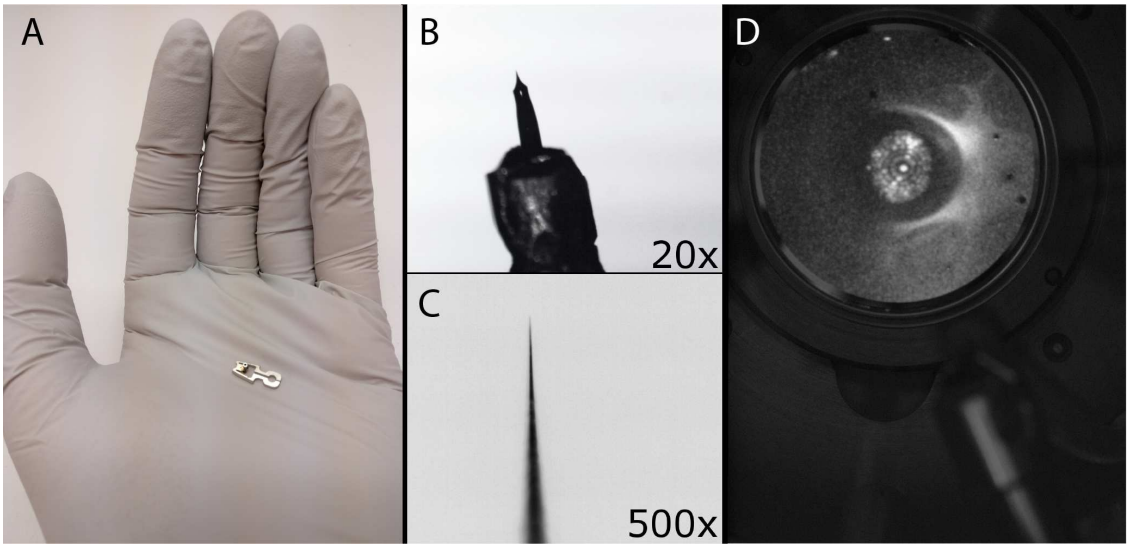

Figure 3.2: A tungsten nanotip. **(A)** An STM1 tip holder. **(B,C)** Optical micrographs of the nanotip. **(D)** A photograph of the MCP-screen assembly during field ion microscopy of the nanotip. A single predominant apex atom can be clearly seen.

the MCP-screen assembly. The image produced on the screen can be captured with a camera positioned outside the vacuum chamber (Figure 3.2D). There are three principles that combine to provide atomic resolution [58]. First, there is a constant supply of imaging gas, because it is adsorbed on the tip's shank and is continuously funnelled towards the apex. Second, because the field is most intense at sharp edges the imaging gas ionizes almost exclusively near the apex and preferentially over single atom steps. Finally, the ion beam is highly focused, such that the beams originating at each apex atom do not cross. The resulting ion beams reveal the atomic structure of the apex, permitting characterization of the predominant crystal facet and estimation of the tip's apex radius.

Admission of a suitable second gas can be used to controllably sharpen the tip through a process known as field assisted etching [57]. In the case of a tungsten tip we admit nitrogen gas. It has a lower ionization energy than helium and therefore never reaches the apex. It does, however, chemically etch the shank [59], resulting in a slow controlled etch of the tip. Field assisted etching can be used to consistently sharpen nanotips to a single apex atom, if desired [57]. Progress of the tip's sharpening is evidenced by the gradual acceleration of field emission of the apex atoms while a

constant bias voltage is maintained on the tip.

After performing field assisted etching a nanotip rarely images perfectly without *in-situ* processing [60]. There are two techniques we typically utilize while in STM mode: applying short voltage pulses (3 V, $\sim$ 20 ms) to the tip while it is close to the surface to generate large perturbative fields, and gently touching the tip to the surface (controlled-contact). In both cases one hopes that the apex atoms rearrange themselves to be more stable and sharp but the outcome of any individual action is uncertain to improve or worsen the tip. *In-situ* processing therefore requires equal parts luck and patience, which is why the group has recently moved to automating it with machine learning techniques. [60] One important consequence of these techniques is that when we scan we cannot have precise knowledge of the atomic structure or composition of the tip because tip atoms are rearranged and sample atoms may be picked up.

3.2 | Piezoelectric Motors

The two sets of motors used to position the tip are both based on piezoelectric materials. A coarse motor moves the tip in steps of roughly one hundred nanometers by action of a 'stick-slip' mechanism, while a fine motor is used to control movements with picometer resolution [31]. To approach the tip to the sample the two are used in tandem: the coarse motor takes a step or two and the fine motor sweeps its full range. This process repeats until a tunnelling current is achieved.

Piezoelectrics are materials that physically deform when a bias is applied across them. A number of designs have been presented over the years to exploit this property for scanning. The simplest is the three-leg scanner, in which the tip is held in a mount supported by three piezoelectric legs [4]. Applying biases across the three legs can be used to move the tip in all three dimensions (although there is no ability to rotate the tip). Another clever design is the tube scanner [61]. In this design several electrodes are patterned around the circumference of a single cylindrical crystal. The tip is mounted on top of the cylinder, and can be moved across the surface as the tube stretches and bends under electrical control.

One important experimental consequence of piezoelectrics is that their displacment due to an applied bias voltage is non-linear becuase they are ferrorelectrics [62].

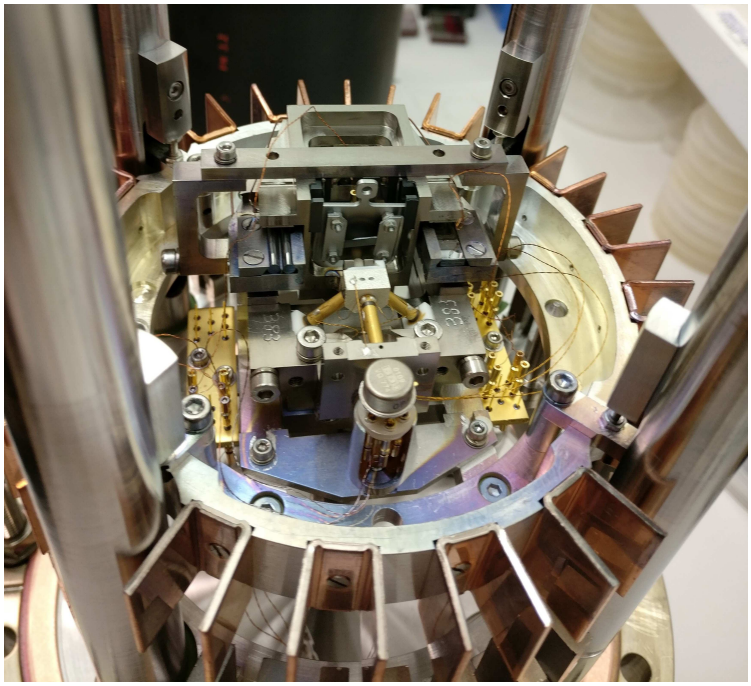

Figure 3.3: The stage of an Omicron STM1, a room-temperature scanning tunnelling microscope. The tip is mounted in the center of the stage where the three piezoelectric legs of a three-leg scanner can be clearly seen. Directly opposing the tip is a small sliver of silicon which was scanned. Copper fins mounted around the circumference of the stage aid in damping vibrations by inducing eddy currents in steel inserts when the stage is hung from its supporting springs.

When a step change in the bias voltage is applied to a piezoelectric in order to reposition the tip there are two distinct periods of the response. The first period is known as the dynamic repsonse, [62] which is short (several milliseconds) and accounts for the majority of the piezo's overall response. The second period is piezo creep and during this period the remaining displacement of the piezo is achieved logarithmically in time, often with a slow time constant [62]. Consequently, large movements of the scanner result in slow uncontrolled movements of the scanner. This can contribute to the tip moving towards the sample or away from the atom of interest mid-experiment.

3.3 | Ultrahigh Vacuum

All of the microscopes used in our group operate in ultrahigh vacuum (UHV) ($<$ 1×10^{-10} Torr). This is required to ensure samples remain clean from adsorbates

that would interfere with our studies.[2] The strong relation between absolute pressure and surface contamination has lead to the widespread adoption of the Langmuir unit by the surface science community [63]. One Langmuir (L) is defined by the exposure of a surface to 1×10^{-6} Torr for one second and corresponds approximately to the formation of one monolayer of adsorbed gases assuming that all the molecules that meet the surface stick to it. At the pressures achieved in our systems this often permits samples several days before they've had an equivalent dose of one Langmuir. Furthermore, because the specific surface we work with (Si(100)-H) is relatively inert the sticking coefficient is small [64]; in practice we can often scan the same sample for several weeks or months, saving us a great deal of effort in not having to continually prepare new samples.[3]

To achieve these pressures our group uses a combination of pumps and commercial vacuum chambers. For roughing pumps we utilize Tri-Scroll pumps because of their cleanliness. These typically back turbo pumps which are used to cycle the load lock, gas lines, and FIM chamber. Our main pumps are a combination of ion pumps and titanium sublimation pumps. These are essential because they pump extremely effectively without contributing any vibration.

3.4 | Vibration Isolation

Thoughtful engineering is required to isolate scanning probe microscopes from vibration [4]. Several of the machines rest on thick concrete pads that are separated from the foundation via a rubber lining, thus damping the low frequency vibrations present in any structure. The microscopes are constructed on thick steel tables that rest on legs that are filled with a steady supply of compressed air. Active air legs, which are used for several of the machines, are also equipped with accelerometers that constantly inform piezoelectric actuators on the legs to compensate vibrations and level the table. Close to the head of the microscope there are two more critical components. The stage, which holds both the nanotip and sample, is suspended on springs. Also attached to the periphery of the stage is a series of copper fins which

[2] There are research areas where scanning probe techniques are used under ambient conditions or with the surface submerged in solution.

[3] This depends on which microscope we use. Because the inner shields of the low-temperature machines act as a cryopump samples remain clean much longer than in room temperature machines.

overlap anchored magnets; when the stage is hung, vibrations induce eddy currents in the copper fins and damp the motion of the stage. With these controls we are able to achieve ~ 0.1 pm/$\sqrt{\text{Hz}}$, with < 50 Hz frequencies limiting further isolation.

3.5 | Low Temperature

The second critical component ensuring the stability of our microscopes is temperature. While the group has previously worked on room-temperature machines the two newest additions are both consistently cooled to 4.5 K. Two jackets line the inside of the head of the microscope to cool the critical components. The outer jacket is filled with liquid nitrogen that cools the microscope to 77 K. The inner jacket is filled with liquid ^{4}He which maintains it at ~ 4.5 K for two to three days per fill.

Low temperatures greatly improve the stability of the microscope by minimizing thermal drift. Thermal drift is the result of small fluctuations in temperature which cause corresponding expansions or contractions of the materials in the machine, and thereby uncontrolled movements of the scanner. Coupling the machine directly to a large thermal bath also means that the heat generated from use of the piezoelectric scanners is efficiently dissipated. These two factors combine to make scanning at low-temperatures so stable that individual atoms can be tracked over the course of days or weeks.

3.6 | Control Electronics and Signal Acquisition

Scanning probe microscopes rely heavily upon a system of feedback control electronics. The physical origin of the signal used for control varies depending on the type of microscope or its mode of operation, but in the Wolkow lab the primary mode we use is scanning tunnelling microscopy, in which case the control signal is the tunnelling current. Typically the goal is for the microscope to maintain a constant tunnelling current by adjusting the height of the tip via the piezoelectric motors. To achieve this, the tunnelling current (which is often < 100 pA) is first amplified by a preamp positioned close to the tip. The signal is then digitized by an analog to digital converter (ADC) and fed into a field programmable gate array (FPGA). A copy of this digital signal is sent to a workstation for display and record. Depending on

the settings applied by the operator (*e.g.* maintain 50 pA tunnelling current) the FPGA returns commands to a digital to analog converter (DAC) which is continuously feeding control signals (including the voltage applied to the piezoelectric motors) back to the microscope. A similar flow of signals is used to record all the relevant experimental parameters, and the reverse process can be used to impose a series of signals on the microscope to perform spectroscopy (*e.g.* vary the bias). Control and signal acquisition is implmented *via* commercial control electronics.

A similar system is used to regulate the control of the AFM. We utilize q-Plus sensors which were introduced by Franz Giessibl in 1998 [65]. Due to a clever design they can also be used for STM, such that we can dynamically switch between STM and AFM operation. The main component of these sensors is a quartz tuning fork, which when operating in AFM mode is driven at (or near) its resonant frequency (f_0). Due to interactions with the sample the cantilever oscillates off resonance (f). Because quartz is a piezoelectric material, the oscillating cantilever produces a time-varying voltage across it which can be captured by electrodes patterned directly on the cantilever's sides. This weak signal is quickly amplified by a preamplifer mounted close to the sensor before being filtered and sent to the ADC-FPGA-DAC stack. Splitting the signal into several branches allows one to control multiple feedback control loops. We typically operate two: one that controls the driving amplitude from the V_{RMS} of the response signal; and one that controls the driving frequency from the phase shift between the driving and response signals (ϕ). Both control systems act in conjunction to maintain a constant oscillation amplitude of the tip.[4] The primary signal used for recording AFM images is the frequency shift $\Delta f = f - f_0$. This is readily obtained by sending one copy of the response signal through a phase-locked-loop [46].

[4] A third controller can be used to regulate the tip-sample separation while in AFM mode. To avoid complications with this third controller we typically operate the AFM with this control loop off and periodically set the height *via* STM.

4 | The Silicon Surface and Dangling Bonds

4.1 | Surface Reconstructions

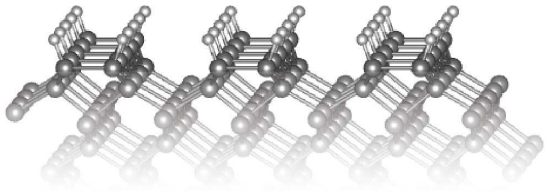

Figure 4.1: The H-Si(100)-(2×1) reconstruction. Silicon atoms in dark grey, H atoms in light grey.

There are many ways to cleave a crystal, and doing so creates a new vacuum-facing surface on which we can scan. Crucially, however, this new surface is often not stable. On a microscopic level, cleaving is the process by which bulk atoms are torn apart from one another, resulting in the creation of orbitals which remain unsatisfied at the vacuum interface. These orbitals are known as DBs. To minimize the total free energy, crystals will often spontaneously reorganize several layers of atoms near their surface, often in a direct effort to minimize the number of DBs [66]. While these layers must bond directly to the bulk atoms, their atomic structures are distinct from those of the bulk. It is therefore important in SPM experiments to specify the surface reconstruction being studied.

There are many surface reconstructions of silicon. They can often be controllably created by cleaving the crystal along a specific orientation and following an annealing protocol. Heating the crystal provides it with the energy necessary to traverse the energy landscape defined by the different reconstructions. The two most commonly studied reconstructions of silicon are $\mathrm{Si}(111) - (7 \times 7)$ and $\mathrm{Si}(100) - (2 \times 1)$.[1] In the Wolkow lab we generally focus on the latter.

To create the $\mathrm{Si}(100) - (2 \times 1)$ reconstruction we begin by selecting crystals cleaved along the 100 plane. Because Si is a fourth group element and has a diamond bulk crystal structure this symmetrically severs two bonds of each surface atom, creating

[1] These follow Wood's notation for naming surface reconstructions. The first half of the name indicates the direction on which the crystal was cleaved. The second half indicates the size of the new surface unit cell in comparison to the the unrelaxed surface by providing the scaling factors for the two unit vectors.

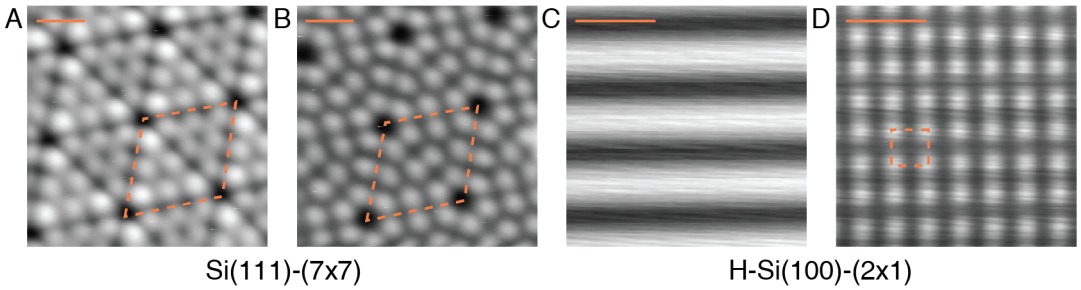

Figure 4.2: STM images of the Si(111)-(7×7) and H-Si(100)-(2×1) surfaces. (A,B) Constant current images of the Si(111)-(7×7) surface at -2.0 V and $+2.0$ V, respectively. **(C)** A constant current image of the H-Si(100)-(2×1) surface at -1.8 V. **(D)** A constant height image of the H-Si(100)-(2×1) surface at $+0.5$ V. Scale bars are 1 nm. Dashed boxes indicate the surface unit cell.

two DBs. This arrangement is unstable. Adjacent silicon atoms pinch together and bond to one another, eliminating one of their two DBs and forming what is known as a silicon dimer [66, 67]. To relieve strain on the crystal lattice, dimers form along a series of long parallel rows. The orientation of the dimer rows shift by ninety degrees upon traversing step edges as a consequence of silicon's diamond crystal structure. Crucially, each surface atom is equivalent but the overall structure of the surface is anisotropic.

4.2 | Donors and Surface States

Silicon is a semiconductor. In a pure sample at 0 K the Fermi level would lie directly in the middle of the band gap. Introducing group three (acceptors) or group five elements (donors), *aka* doping, can be used to lower or raise the Fermi level, respectively. At low temperatures donors 'freeze out' because they lie approximately 50 meV below the conduction band, so there is insufficient thermal energy for them to ionize [68]. As a result, silicon typically has poor electrical conductivity at low temperatures. To study them at low temperatures we use highly n-doped samples. At high enough concentrations ($> 10^{18}$ atoms per cm^3) the donor wavefunctions overlap, creating a conductive band approxmiately 50 meV below the conduction band [69].

Interestingly, we can selectively vary the concentration of donors as a function of depth in the lab *via* our annealing protocols [70]. In preparing Si(100)$-(2\times1)$ we must

heat the crystal to temperatures > 900 °C in order to remove the surface oxide layers. At these elevated temperatures silicon also begins to evaporate slowly. Previously the group has used secondary ion mass spectrometry to provide measurements of samples' compositions as a function of depth [70]. It was found that samples heated to 1050 °C had a consistent concentration of donors, while those heated to 1250 °C had up to two orders of magnitude lower concentrations of donors in the near surface. This indicates that at high temperatures the donors evaporate preferentially. At 1250 °C this dopant depletion region was found to extend 100 nm. Controlling the extent of dopant depletion provides us with a mechanism to vary the strength of coupling between surface states (*ie.* DBs) and the bulk. Small local variations in the proximity to dopants also explains why individual DBs often have unique $I(V)$ characteristics [71,72]. In general, because the surface dopant concentration is higher for 1050 °C samples we typically find DBs to behave more uniformly compared to those found on 1250 °C samples [71].

Of paramount importance to SPM experiments are electronic states that exist at the surface of the crystal. Surface states can be broadly assigned to one of two types: those arising from imposing boundary conditions on the Bloch states that describe the bulk, *ie.* Shockley states, and those that arise from the overlap of atomic states on the surface *ie.* Tamm states [73]. Surface states of semicondcutors often lie within the bulk bandgap and are highly conductive [74]. In the context of SPM surface states dramatically alter $I(V)$ characteristics [75]. First, they give rise to large tunnelling currents where one would otherwise expect to be within the bulk bandgap. Second, they often drown out signals arising from less conductive pathways. Thus, many SPM studies of semiconductors require the elimination of surface states [75]. With the Si(100) $-$ (2×1) surface this can be achieved by terminating the surface with hydrogen [74], effectively replacing the DBs which form the surface states with an inert monolayer [64]. Molecular hydrogen is leaked into the vacuum chamber, cracked to atomic hydrogen by a hot filament, and left to covalently bond with the surface atoms [76]. This results in the H-Si(100) $-$ (2×1) surface, whose $I(V)$ characteristics closely match those of the bulk crystal [74].

4.3 | Band Bending

The physics of materials at their interfaces often differ drastically from their bulk. One significant example of this is band bending in semiconductors [77]. Consider that when calculating the effect of an electric field on a metal it is assumed that the potential across the metal is zero; this is because there is a high concentration of free carriers in metals, such that the external field can draw charge to the surface counteracting its effect. Because the concentration and mobility of free carriers is drastically lower in semiconductors, this cannot occur. As a result, electric fields penetrate the surface, charging a finite volume, which then screens the external field. Put another way, the electronic bands at the surface can be shifted up or down in energy relative to the bulk. This effect is clearly exacerbated when performing experiments at low temperatures where the concentration of free carriers is much lower.

Numerical solutions to Poisson's equation can be used to evaluate the the field strength throughout a semiconductor. To this effect Randall Feenstra has made freely available a software package known as SemiTip that is designed specifically for SPM experiments [78]. What is crucial to note is that such calculations can only provide qualitative evidence to support experiment. This is because numerical solutions for band bending require one to specify parameters including the geometry of the tip's apex, the concentration of near surface donors, and the exact tip sample separation, which are typically unknown. Nevertheless, in order to correctly interpret SPM experiments on semiconductors it is essential to carefully consider the contributions to and the effects of band bending.

The first contribution is due to the contact potential difference (ϕ_{CPD}) [1, 78]. This is the field between the tip and sample that exists at zero applied bias voltage (even when the tips are not in direct contact), and is due to the difference in the work functions of the two materials.

$$\phi_{CPD} = \phi_{tip} - \phi_{sample} \tag{4.1}$$

In our experiments we use tungsten tips and silicon samples for which $\phi_{tip} \approx 5$ eV

and $\phi_{sample} \approx 4.1$ eV [1].[2] Thus the contact potential difference is on the order of 0.9 eV and shifts the bands of the sample up in energy.

The second main contribution is due to the applied bias voltage [1, 78]. As was described earlier, the applied bias voltage can be used to directly counteract the contact potential difference. This is known as flat band conditions [1,78]. By applying a positive (negative) sample bias one can also further shift the bands up (down) (Figure 4.5). Because the tip's Fermi level must be aligned with the conduction or valence band of the sample to generate a tunnelling current the applied bias is often ≥ 1 eV. The combined effects of the contact potential difference and the applied bias typically dominate overall band bending and for this reason the community often refers to the sum of their contributions as Tip Induced Band Bending (TIBB) [78].

The third contribution is due to local surface charges [1]. For example, if TIBB is great enough to ionize a donor ($D \rightarrow D^+$) one must consider the downward contribution of the positive charge to the local bands. Typically these effects are small but they are often required to accurately describe the charging of surface nanostructures [72, 79, 80]. The final contribution to band bending is essentially a second order effect of these local charges: they create a small electric field which imposes new boundary conditions on the metallic tip [78, 81]. The classical way of solving this problem is to produce an image charge in the tip such that the electric field is perpendicular to and does not extend beyond the surface of the tip. In this way, a positive charge on the surface produces a negative image charge, shifting the bands up (or *vice versa*). Crucially, this effect is typically negligible, but it can become significant with small tip sample separations [78, 81].

4.4 | Dangling Bonds

Despite the fact that the silicon surface has now been studied for decades there is still fundamental and applied physics to be explored. Of the numerous surface defects that exist our group is focused on studying one: silicon DBs.

[2] The work function of the tip depends on the crystal structure of the apex. The work function of a semiconductor depends on the temperature and doping level. In both cases these cannot be known precisely during experiment but can be reasonably estimated from bulk values.

4.4.1 | Defining Characteristics

DBs are sp^3 hybridized atomic orbitals whose lobes are oriented roughly perpendicular to the surface. While there are many interesting properties of DBs most are derivative of two key characteristics.

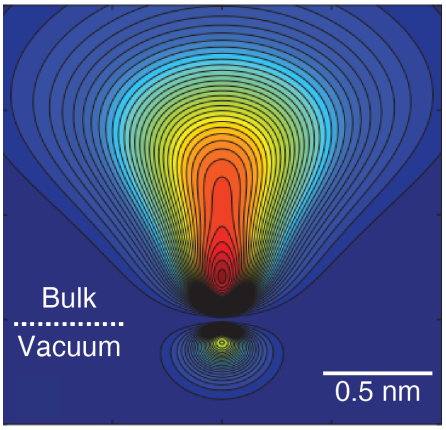

Figure 4.3: Normalized charge density of a DB The lobes are unequal in size because of the greater permittivity of the bulk. Figure taken from [1].

In the context of condensed matter physics dimensionality refers to the number of angular degrees of freedom for a wavefuntion to spread. By this definition, a gas of electrons confined to the interface of two crystals is considered to be two dimensional. Because DBs are single atomic orbitals, they are effectively zero dimensional [27]. This gives experimenters the great freedom to design one or two dimensional potentials by making larger patterns of DBs [2, 27, 82–84].

The second key characteristic is that DBs display several charge states. The DB^+, DB^0, and DB^- charge states correspond to when the atomic orbital hosts 0, 1, or 2 electrons, respectively [27]. What is crucially important is that the energies at which isolated DBs transition between these charge states lie within the bulk bandgap, such that they are electronically decoupled from the bulk [27], though the exact energies of the charge transition levels are disputed [83, 85, 86]. The energy difference between these charge transition levels is due to the on-site Coulomb repulsion between the electrons (often referred to as the Hubbard U) [86]. Of fundamental importance to the experiments described in this thesis is that because of the mutual electrostatic interactions between DBs, and also due to the applied bias voltage, DBs may be neutral or negatively charged [27]. This means that the charge occupation of larger DB structures cannot be predicted by simply counting the number of constituent DBs.

At this point it is important to disambiguate the DB charge states (DB^+, DB^0, DB^-) from the DB charge transition levels ($DB^{+/0}$, $DB^{0/-}$). The former can be observed directly by AFM, [80] while the latter are what are observed indirectly by

STM [71, 79]. This can be rationalized by noting that a tunnelling current only occurs when the DB is repeatedly ionized and reduced. Therefore the DB is only capable of sourcing a tunnelling current while the Fermi level of the tip sweeps through a charge transition level. Note this also implies that the $DB^{+/0}$ and $DB^{0/-}$ levels are mutually exclusive, because a DB^{+} must be reduced before the $DB^{0/-}$ level may exist.

The dimensionality and charging characteristics of DBs and structures derived from them make them equivalent to atomic-sized quantum dots [27]. Notably, they have several distinct advantages compared to traditional nanoscopic quantum dots. Firstly, the energy splitting of the electronic levels is on the order of 100 meV [85] which is orders of magnitude larger than $k_B T$ at 4.5 K (~ 0.04 meV). This contrasts traditional quantum dots which typically require mK temperatures to avoid thermal excitation. Second, they can be fabricated with digital fidelity because the DBs are restricted to the periodic spacing of the silicon lattice. This means that the electronic structure of quantum dots formed from DBs can be precisely crafted [83], and ensembles of quantum dots can be fabricated with tunable couplings [2]. Finally, structures derived from silicon DBs are extremely stable because the energy required to break the H-Si bond is ~ 3.3 eV [87].

4.4.2 | Patterning

There is a natural abundance of DBs on the hydrogen-terminated silicon surface, but they can also be deterministically created. The use of STM to selectively remove H-atoms from the silicon surface was first demonstrated on H-Si(111) in 1990 by Becker *et al.* [88], and extended to H-Si(100) by Lyding *et al.* in 1993 [87]. These techniques were quickly framed as atomic-scale lithography, permitting the study of surface reorganization and surface chemistry restricted to atomically defined domains. Two desorption mechanisms were found to describe the process [89, 90]. The first is electronic excitation of the H-Si bond by individual free electrons. This occurs when the tip is withdrawn a short distance from the surface and made to field emit high-energy electrons (> 6.5 eV). This is a 'shotgun' approach that one can use to quickly create large patches of bare silicon ($\sim 5 \times 5$ nm^2 or larger). The second mechanism is vibrational excitation of the H-Si bond by many low-energy inelastic tunnelling electrons. The tip is left within tunnelling distance and short voltage pulses ($\sim$ 20

ms, ~ 2.0 V) are used to briefly enhance the tunnelling current. Because tunnelling electrons are used it is far more precise, and can be used to controllably desorb individual H-atoms.

Two advancements by our group in the past few years have greatly improved our patterning proficiency. Firstly, group members have successfully designed an automated patterning program (Møller *et al.* have also published on a similar program [28]). Based in LabView for integration with our microscopes' commercial control software, a user may specify an arbitrary pattern of DBs on a two dimensional grid that can be overlaid on a scan. The program then automatically moves the tip to the prescribed locations, and at each location applies a train of voltage pulses. The amplitude of the voltage pulses is slowly increased until a feedback signal indicates the successful formation of a DB (a step change in the current while operating in constant height mode). The feedback controller is then re-engaged before the tip moves to the next location, repeating this process until the pattern is complete. The periodicity of the lattice is utilized to ensure the tip is correctly positioned over the correct atom, such that the software can create large patterns with only $\sim 5\%$ error (limited by tip irregularities).

The second advancement is the ability to selectively re-passivate individual DBs [29,30]. The procedure for doing so is simple and can be performed in AFM or STM mode: a hydrogen-functionalized tip is positioned above a DB and brought close enough that the hydrogen atom may form a covalent bond with the surface silicon atom. The reason that this procedure was only recently discovered is that it was previously unknown how to functionalize the tip. As it turns out, tips often pick up hydrogen from the surface while scanning or creating DBs. The key is identifying when a hydrogen atom is at the tip's apex, for which the group has identified two signatures [29,91]. First, hydrogen-terminated tips often scan with enhanced contrast, such that the individual atoms in dimer rows can be resolved. Second, the $\Delta f(z)$ spectra of hydrogen-functionalized tips often show two local minimums. The first minimum is attributed to the hydrogen atom at the tip's apex being physically bent out of position as the tip approaches the surface [29, 91]. The significance of this advancement is that we can now create atomically precise patterns of arbitrary size by patterning DBs on high-quality regions of the sample and repairing any errors we

make in the process.

4.4.3 | Imaging

DBs can be discriminated from other surface defects by their unique appearance in STM images. At negative sample bias (filled-states, Figure 4.4A) DBs appear as bright protrusions on the surface. Typically, even as larger structures of DBs are created, each individual DB retains its distinct atom-like appearance in filled-state images (Figure 4.4D). At positive sample biases (empty states, Figure 4.4B) the appearance of isolated DBs depends on their local environment and the imaging bias. At modest biases (*eg.* < 1.5 V) the DB itself remains brighter than distant H-Si, but the H-Si in the region immediately surrounding the DB is dark (often referred to as a dark halo) [1]. This is because the DB is negatively charged, such that the local bands are pushed up in energy, thereby lowering the tunnelling current. As the imaging bias is increased, however, TIBB increases and eventually raises the $DB^{0/-}$ level above the Fermi level [1]. Under these conditions, the halo disappears because when the tip is not directly over the DB it is neutral.[3] Even at high positive bias, however, the DB remains negatively charged while the tip is directly over it. This is because the rate at which the tip can inject electrons into the DB is greater than the rate the DB can empty [1]. This information is clearly contained within $I(V)$ curves taken over the DB and H-Si. As larger structures of DBs are patterned their empty-states appearance change dramatically (Figure 4.4E). Unlike filled-state images, empty-state images of larger structures demonstrate complex molecular-like orbitals [83].

Empty-state STM images of isolated DBs also contain information about the single-electron charging dynamics of the DBs [79]. The area at the edge of a DB's halo often has a speckled appearance. Analysis of the current measured in constant height mode over the speckled region reveals telegraph noise, with apparently random fluctuations between three states, corresponding to the three charge states of the DB [79].[4] When imaging at positive bias the overall TIBB is upwards, thus the DB^- and DB^0 states are unstable, and electrons confined to the DB are capable of

[3] On 1050 °C samples, which do not have a dopant depletion region, this requires very large biases. Therefore DBs appear dark in nearly all empty-state images on these samples [1].

[4] The DB^- state pushes the local bands up, reducing the tunnelling current. The DB^0 state doesn't influence local bands. The DB^+ state pushes local bands down, enhancing tunnelling current.

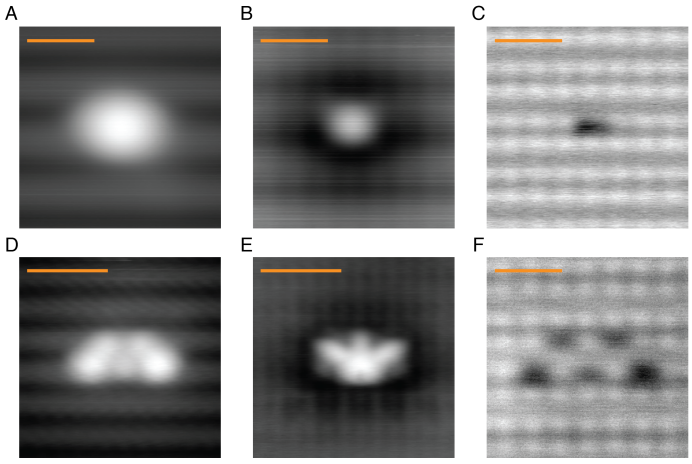

Figure 4.4: STM and AFM images of a DB and a DB ensemble. (A,D) Constant current STM images at −1.8 V and 50 pA (filled states). DBs appear as bright atom-like protrusions. **(B,E)** Constant current STM images at +1.3 V and 50 pA (empty states). Individual DBs appear as bright protrusions with a dark halo due to local band bending. Larger DB structures reveal complex molecular-like orbitals. **(C,F)** Constant height Δf AFM images with $A = 50$ pm and $z = -300$ pm. DBs appear as dark depressions among the lightly coloured hydrogen atoms. Scale bars in A-C,F are 1 nm, and 2 nm in D,E.

tunnelling to the conduction band. One must also consider that the nearby tip is constantly injecting charge into the sample. When the tip is very close to the DB the rate at which electrons are injected into the DB^+ and DB^0 levels is fast enough that the DB is essentially always negatively charged. As the tip is moved away from the DB, however, these rates rapidly diminish, such that the emptying and filling rates are comparable, and the tunnelling current shows telegraph noise indicating that all three states can exist on a millisecond timescale.

The contrast observed over hydrogen, neutral and negatively charged DBs when imaged with AFM at zero applied bias voltage depends on the exact tip-sample separation, as a result of the complex interplay between short and long range forces [2,3]. With small tip sample separations (< 400 pm absolute tip height) both neutral and negatively charged DBs appear dark relative to hydrogen (larger $|\Delta f|$). This is because at short ranges the tip experiences some repulsive short range forces over hydrogen (Figure 4.4C,F). Negatively charged DBs appear darker than neutral DBs because the image charge they induce in the tip creates an attractive electrostatic interaction [3]. Occasionally, when larger structures of DBs are imaged at zero bias

with AFM they appear streaky [3], not unlike the telegraph noise observed in empty states STM. This is the focus of a Chapter 5.

4.4.4 | Transport

As a naive approximation one might expect DBs to have a similar conductance to H-Si. As they exist within the bulk bandgap, DBs should not be able to mediate a tunnelling current between the tip and the bulk. In addition, because DBs are discrete states (*i.e.* atomic orbitals) rather than energy bands, one might expect that tunnelling current could only be drawn through a DB over a very sharp energy range. Both of these expectations turn out to be false [40, 79].

In the first case, in the absence of band bending it is true that DBs would be incapable of sustaining large tunnelling currents. Filling DBs with electrons from the conduction band would be an inelastic process, and electrons injected to the DB from the tip would need to be thermally excited to the conduction band before another could take its place. However, because band bending shifts the near-surface energy levels with respect to the bulk, it is possible to bring the the DB charge transition levels into energetic alignment with both the conduction and valence bands [40,72,80]. In this case, electrons can tunnel elastically between the bulk and the DB. As a result, the DB charge transition levels can act as 'stepping stones' to source a tunnelling current (Figure 4.5B,C).

In the second case, the energy states of an atom are discrete only when it is completely isolated. Because DBs are in close proximity to the bulk, and also to the tip while we study them, their energy levels acquire a finite width [92]. This phenomenon is known as level broadening and is well studied in mesoscopic and nanoscopic physics where single electron transport is of fundamental importance [93]. The complete quantum mechanical treatment of level broadening is very involved, but one clear result is the following [92]:

$$D(E) = \frac{\gamma/2\pi}{E^2 + (\gamma/2)^2} \tag{4.2}$$

Here $D(E)$ is the density of states of a single level at energy E and γ is the coupling strength between the level and the two reservoirs it bridges (*i.e.* the tip and sample). The density of states of the level spreads from a delta function when γ is zero to a

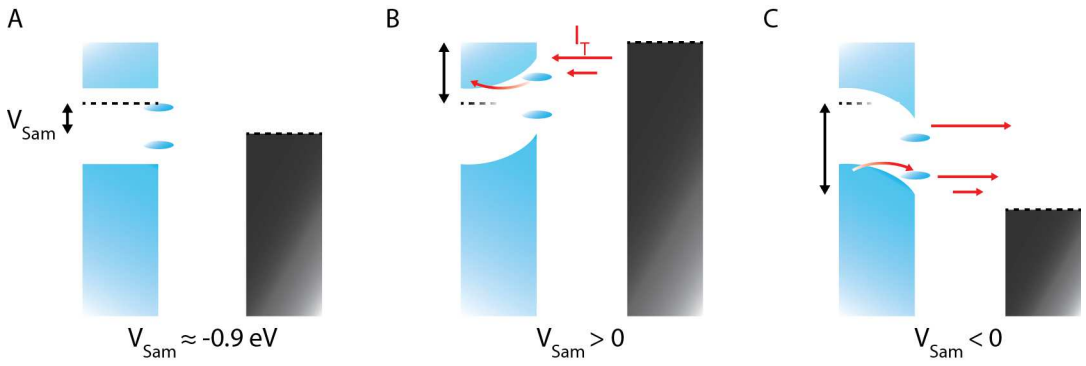

Figure 4.5: Band diagrams for a silicon DB and a metallic tip. **(A)** Flatband conditions occur when the the applied bias (V_{Sam}) directly counteracts the contact potential difference between the tip and sample. In this case, negligible tunnelling current is sourced *via* the DB. **(B)** Upward band bending occurs when a positive bias is applied to the sample. **(C)** Downward band bending occurs when a negative bias is applied to the sample. In both (B) and (C) the DB acts as a 'stepping stone' for the tunnelling current. Black dashed lines indicate the Fermi level. DBs are depicted as ellipses due to level broadening.

broad Lorentzian when γ is large. This can be understood as the discrete level of the DB mixing with the continuum of states in the bulk and tip. Because the integration of $D(E)$ over the full energy range always remains one, level broadening does not give rise to new states, but simply smears out the range of energies over which the DB can be used to channel current between the bulk and the tip [92]. As such, even though DBs may only channel electrons through the $DB^{+/0}$ and $DB^{0/-}$ levels, they can do so over a range of energies that depends on how strongly the DB is coupled to the two reservoirs. This coupling strength can be controlled to some extent, for example, by the DB's proximity to dopants [72].

4.4.5 | Applications

In the previous section we considered transport between the bulk and tip *via* DBs, but there is also the potential to transport charge across the surface through the DBs. Indeed, there has been extensive theoretical study supporting the idea that densely packed DBs can be used to carry current. [94, 95] Because the density of states of DB wires are anticipated to reside within the bulk bandgap they would be naturally electronically isolated from the bulk. At present several different wire designs have been proposed, the simplest of which is to simply remove all the H atoms from a dimer

row [94, 95]. There are two paths currently being pursued to prove this technology. The first is to perform multiprobe experiments, where current is injected to one end of the DB wire and sensed on the other with two STM tips. While multiprobe measurements have been performed on H-Si(100)-(2x1) before [96], it is extremely challenging to integrate multiple tips into a low-temperature machine. Both tips must be capable of atomic resolution imaging and must be arranged on either side of an atomically defined wire (likely within < 100 nm of one another). The second approach is to connect both ends of the wire to traditional lithographic leads (so called 'macro-to-atom contacts') [97]. This is challenging because the lithography must be performed such that the surface remains atomically flat and clean. In either case, upon realizing functional DB wires a host of interesting physics is immediately foreseeable, including the ability to study Coulomb Blockade phenomena and single atom/molecule transistors.

Beyond wires, DBs have been used as the fundamental building block in several future-facing computing technologies. Our group originally explored DBs for Quantum Cellular Automata (QCA) [27, 98]. In this family of technologies, quantum dots are arranged into four-dot unit cells. Within each unit cell charge can freely tunnel between each dot. Unit cells are then spaced far enough apart that their interactions can be explained classically *via* electrostatics. The central idea is that each unit cell will take on one of two orthogonal electronic polarizations. By varying the spacing and 2D arrangement of the unit cells they can be used to transmit binary information, compute classical logic functions (*eg.* AND, NOT), and build other advanced computational devices (*eg.* shift registers) [98]. In addition to their natural electron isolation, DBs are pursued in computing contexts because they can be patterned with digital fidelity. In theory, this should eliminate any dispersion in the operating character of devices derived from them.

Another approach to classical computing is Quantum Hamiltonian Computing which is being developed by Christian Joachim [99, 100]. Large structures are patterned from individual DBs to form logic gates. Unlike QCA, the logical states of the gates are not encoded in the electronic polarization of the structure, but in the conductance of a specific region of the gate. This conductance can be modified by patterning additional DBs at specific locations, or leaving them as H-Si, to serve as

the logical inputs. Also unlike QCA and classical computing, in this approach gates are not designed to cascade to achieve more complex logic functions. Rather, logical complexity is achieved by creating larger atomic gates with additional inputs.

More recently our group has developed a derivative of QCA called Binary Atomic Silicon Logic (BASiL) that utilizes two DBs as the unit cell [2]. While it remains preliminary, BASiL has successfully demonstrated a reversible binary wire and an OR gate. Current efforts with this line of research are to demonstrate more logic functions, fanout, and cascading multiple gates using binary wires to transmit the signal between them.

Several other applications of DBs have been explored. These have included using them to define charge qubits, [85, 101, 102] and for deterministic donor placement, [103].

5 Controlling Individual Electrons with Non-Contact Atomic Force Microscopy

Atomic manipulation [12, 104] has emerged as a powerful strategy to fabricate novel atomic physical-systems [16, 105, 106] and devices. [2, 14, 107][1] An important addition to this experimental toolkit would be the ability to design and control functional atomic charge configurations with single electron precision. To this end, several studies have demonstrated the ability to create, move, and controllably switch charged species on a surface with scanning probe techniques [23, 25, 26, 108–111]. While elegant, these studies have relied on large perturbative fields applied by the probe naturally impeding their use in the investigation of systems where charge states are loosely bound and prevents the generalization of results to systems in the absence of a probe. Here, we use atomic manipulation to design symmetric and asymmetric confining potentials and demonstrate methods to controllably position and track single electrons within these structures. With these techniques we prepare specific charge states of atomically engineered structures and non-perturbatively observe their field-free temporal evolution. Combining our approach with existing atomic manipulation techniques presents new opportunities for simulating designer Hamiltonians.

We investigate atom defined charge configurations composed of patterned silicon DBs on a hydrogen-terminated Si(100)-2x1 surface [87]. The charge states of DBs are isolated from the host silicon because their energy levels reside within the band gap, [40] eliminating the need for an insulating film between structure and substrate, which was essential in previous studies [23, 25, 26, 108, 112, 113]. The crystalline lattice of the substrate and the ability to selectively re-hydrogenate DBs ensures the perfect spacing of substituent atoms and the ability to create error free designer structures [29, 30, 114]. Recent non-contact atomic force microscopy (nc-AFM) measurements [2, 80] have confirmed that the negative to neutral charge transition of isolated dangling bonds occurs at energies on the order of approximately 300 meV below the bulk Fermi level. This enables their charge state to be selectively modified

[1] This chapter has been submitted for publication in the form presented here. It is currently listed on the preprint server arXiv [3]. A detailed account of author contributions is included there.

by shifting this charge transition level above or below the bulk Fermi level. By performing a series of nc-AFM experiments we study and control the charge states of the engineered atomic structures with single electron charge sensitivity. All experiments are performed with no applied bias between the tip and sample. With the tip-sample separation as our key experimental parameter we uncover two interaction regimes: a strongly interacting regime where we can controllably position single electrons within the structures; and a weakly interacting regime, approximating field-free conditions, where we can nonperturbatively track the position of charge within the structures over time.

In Fig. 5.1, two dangling bonds are patterned with two intervening hydrogen atoms using hydrogen lithography. Figure 5.1a and 5.1b display filled and empty states scanning tunnelling microscope (STM) images of the pair. In a constant height frequency shift (Δf) image of this structure (zero bias, Fig. 5.1c) the dangling bonds appear dark due to additional Coulombic attraction. Two closely-spaced negatively charged dangling bonds experience Coulombic repulsion great enough that one electron is ejected to the conduction band. Consequently, images of the pair appear streaky, as the single remaining negative charge is shared between the pair, switching sites multiple times over the time it takes to acquire an image. This is seen clearly in individual Δf line scans across the structure (Fig. 5.1d) which reveal the localization of charge to one dangling bond, with subsequent line scans demonstrating that this charge occasionally switches to the other dangling bond.

Changes in the distribution of charge within the pair can be followed over time by stacking sequential Δf line scans (Fig. 5.1e). Previous theoretical estimates for the tunnelling rate between two closely-spaced dangling bonds have ranged from THz to GHz, depending on the spacing [85]. Surprisingly, the bistable signal for each dangling bond extracted from Fig. 5.1e demonstrates that the charge states often remain trapped for seconds (Fig. 5.1f), indicating that elastic tunnelling between the paired atoms is not occurring. Recent studies have revealed that charged species are often stabilized by a lattice relaxation of the supporting substrate [23, 115]. Density functional theory has similarly shown that negatively charged silicon dangling bonds experience approximately 200 meV stabilization due to a relaxation of the lattice which raises the nuclear position of the host atom by approximately 30 pm [83, 85]

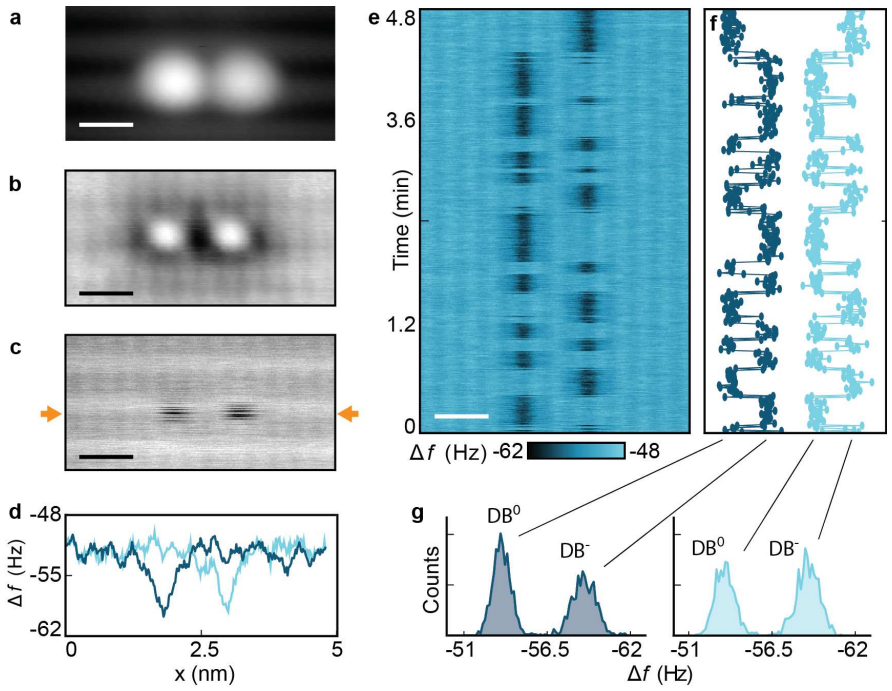

Figure 5.1: Fluctuating charge states of two closely-spaced dangling bonds. **(a)** Constant current filled state STM image of the structure recorded at -1.8 V and 50 pA. **(b)** Constant current empty state STM image recorded at 1.3 V and 50 pA. **(c)** Constant height Δf image of the structure taken at 0 V. The initial tip height is set on a hydrogen atom at -1.8 V and 50 pA before moving the tip 300 pm towards the surface. **(d)** Two individual line scans made in constant height AFM mode along a line indicated by the orange arrows in (c) with a tip offset of -300 pm from the setpoint and at 0 V. The change of peak position is attributed to the electron jumping from one side of the DB pair to the other. **(e)** Combined map of 400 constant height Δf line scans taken sequentially over a five minute period. **(f)** Time dependent bistable signal for the two individual DBs. **(g)** Histograms extracted from the signals in (f). Labels indicate the charge state assignment of each peak. Scale bar is 1 nm (a-c, e).

which in this case prevents elastic tunnelling of the electrons between neighboring dangling bonds. To reliably assign the position of the charge in each Δf line scan, the two dangling bond-centered features were fit with Gaussian profiles. Histograms of the determined Δf show two well-separated maxima, which can be reliably assigned to the negative and neutral charge states of each dangling bond (Fig. 5.1g and Fig. 5.4 and Fig. 5.6). This permits a binary number to be assigned to the charge configuration in each line scan.

We noticed that the occupation of the structure appeared to depend on tip-sample spacing, motivating further study. We performed a series of constant height line scan maps on a symmetric structure composed of six dangling bonds (Fig. 5.2a-d), each with different tip-sample separations. The average occupation of each dangling bond at each height can be inferred from histograms of the Δf measured over each dangling bond (Fig. 5.6). More simply, the average occupation of the entire structure can be inferred by counting the number of dark bars in each line scan map, which is observed to decrease as the tip-sample separation is increased (Fig. 5.2e).

To understand this trend we modelled the interaction between the tip and dangling bonds with a 3D finite-element numerical model, [1, 116] which reveals the height-dependence of the band bending beneath the tip (Fig. 5.2f). Two contributions to the total tip induced band bending (TIBB) at zero bias must be considered: (i) the contact potential difference between the tip and substrate; (ii) a contribution by the image charge induced in the AFM tip. Because the work function of our tungsten tip is $\sim$ 1 eV greater than that of the substrate the contact potential difference results in an upward band bending contribution to the surface. When the DB is negative, the image charge induced in the tip produces a counteracting contribution, which has an approximate 1/z dependence on tip height (z). At small tip-sample separations, the effect of the image charge can exceed that of the contact potential difference, rendering the total potential energy negative. Under these conditions, an electron is stabilized in the dangling bond directly beneath the tip (for simulation details see Fig. 5.5) permitting the tip to be used as a means to manipulate electrons confined to the atomic structure. This effect vanishes with increasing tip-sample separation (Fig. 5.2f). Furthermore, as the tip is retracted the true occupation of the structure is observed (Fig. 5.2e). In this regime, the charge configuration of the

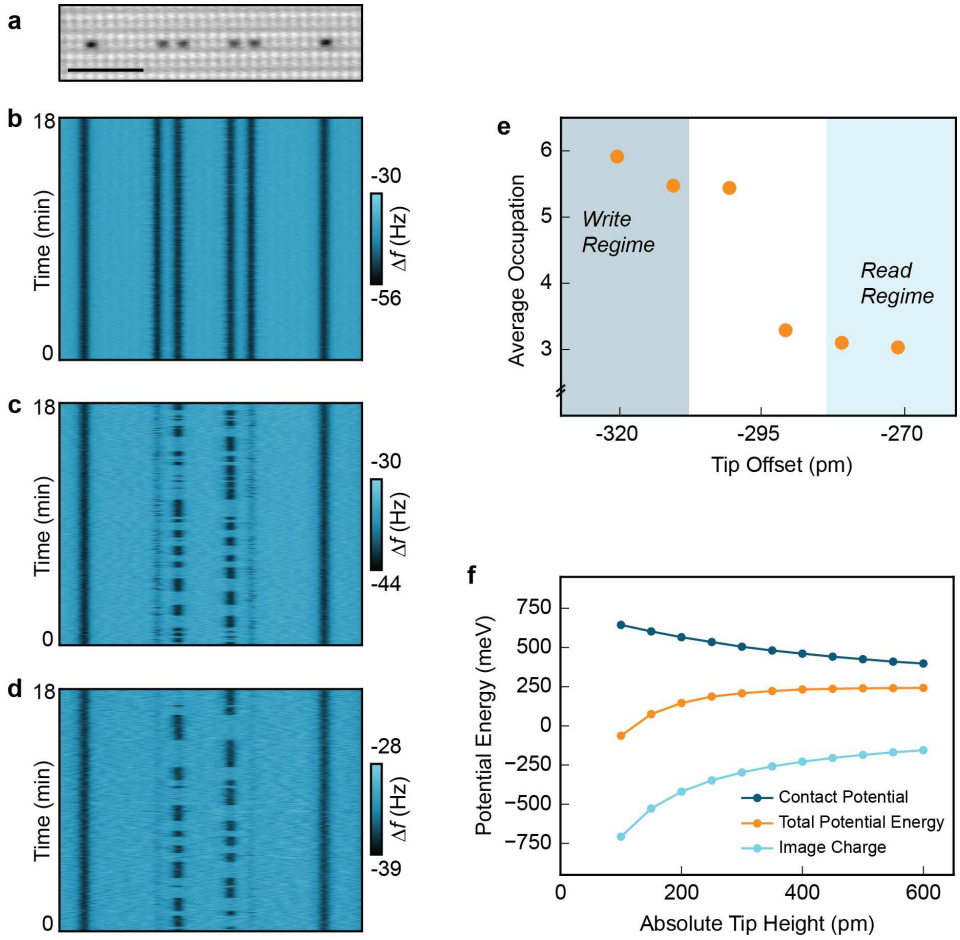

Figure 5.2: Charge state evolution of a symmetric six dangling bond structure at different tip heights. **(a)** Constant height Δf image of the symmetric six dangling bond structure taken at -300 pm and 0 V. The scale bar (a-d) is 3 nm. **(b-d)** Eight hundred constant height line scans at -320 pm (b), -290 pm, (c) and -270 pm (d) reveal the evolution of the system's charge states in time. Tip heights are in reference to an STM setpoint of -1.8 V and 50 pA measured over H-Si. Images contain sweeps in both directions across the sample. Histograms of the Δf extracted over each dangling bond in (b) and (d) are available in Fig. 5.7. **(e)** The average occupation of the structure, inferred from digitizing the charge state of 1600 constant height Δf line scans at different tip offsets, decreases from six to three negative charges as the tip sample separation is increased. Two interaction regimes: read and write are indicated. **(f)** Modelling of the total tip-induced potential energy of the DB electron as sum of two components at zero bias: the contact potential difference between tip and sample and the image charge induced in the AFM tip. The tungsten AFM tip was assumed to have a work function of 5 eV and an apex radius of 5 nm as observed during field ion microscope imaging of tip. The sample's work function was taken to be 4.1 eV. Additional modelling information is available in the Supplementary Information.

system appears to remain unchanged for many measurements (> 15 s on average for both states), suggesting that the tip is nearly non-interacting with the system. From this we conclude that there are two interaction regimes (Fig. 5.2e): a strongly interacting regime with small tip-sample separations where the charge is controllably manipulated by the tip (the *write regime*), and a weakly interacting regime where we can observe the natural charge occupation of the structure (the *read regime*).

Analysis of the charge states observed in the read regime can be used to infer their relative energies. Inspection of Fig. 5.2d reveals that the outermost dangling bonds are continuously charged, however, only a single negative charge is electrostatically confined to the interior of the structure, where it occasionally switches between the two central dangling bonds. By observing that the total amount of time the central charge spends in the left dangling bond (50%) is roughly equal to the right (46%), we confirm the degeneracy of these two charge states.

To further validate our assignment of the *write* and *read* regimes we performed the experiments depicted in schemes Fig. 5.3a-c on the symmetric structure (Fig. 5.3d, the same structure as in Fig. 5.2) and an asymmetric structure (Fig. 5.3i). First, we restricted the measurements to the *read regime* (scheme Fig. 5.3a, Fig. 5.3e,j), allowing us to characterize the intrinsic charge states of the structures and assess their relative energies based on their rate of occurrence (Fig. 5.3h,m). Subsequent experiments contain two associated phases: in the *write phase*, the tip is scanned across the structure at close proximity; in the *read phase*, the tip is retracted 50 pm with respect to the *write phase* and scanned back across (depicted in schemes Fig. 5.3b,c). It might be expected that any charge state prepared by the *write phase* should be observed in the *read phase*. Indeed, Fig. 5.3f,g and 5.3k,l confirm that charge in the interior of both structures can be manipulated. On the symmetric structure (Fig. 5.3d) we could consistently initiate charge to the right (Fig. 5.3f, 85%) or left (Fig. 5.3g, 79%) central dangling bond, corresponding to preparation of the degenerate ground states observed in Fig. 5.3e and Fig. 5.2d. On the asymmetric structure (Fig. 5.3i), measurements restricted to the read regime (Fig. 5.3j) demonstrate that this system has three negative charges, again only the charge confined to the inner pair fluctuates, and because the structure is asymmetric these two charge states are non-degenerate. Although we expected this charge to favour the left dangling bond

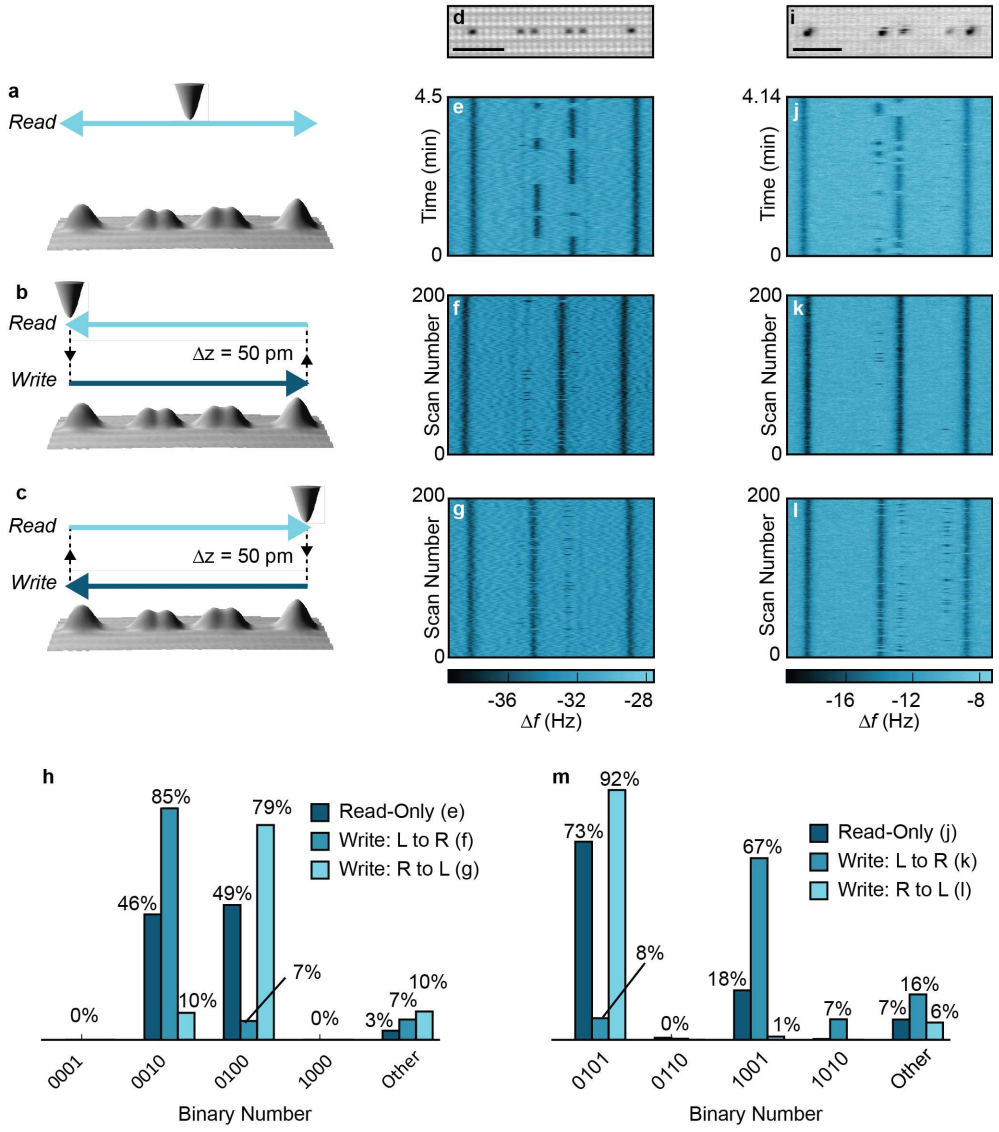

Figure 5.3: Controlled preparation of charge states in symmetric and asymmetric dangling bond structures. Visualization of the scan modes: **(a)** all measurements are restricted to the *read regime*; **(b)** the tip is scanned from left to right in the *write regime*, retracted 50 pm to the read regime, and scanned back across; **(c)** the same process as (b) with directions reversed. **(d)** Constant height Δf image of the symmetric six-dangling bond structure taken at -300 pm and 0 V. **(e-g)** 200 line scans across structure in (d) corresponding to scheme (a) (e), scheme (b) (f), and scheme (c) (g) (*write regime*: -320 pm, *read regime*: -270 pm). **(h)** Histograms of the binary numbers determined from digitization of the line scans in (e-g). 0's and 1's correspond to neutral and negatively charged dangling bonds, respectively. Only the four interior dangling bonds are considered. **(i)** Constant height Δf image of the asymmetric five-dangling bond structure taken at -350 pm and 0 V. **(j-l)** Maps of 200 line scans across structure (i) corresponding to scheme (a) (j), scheme (b) (k), and scheme (c) (l) (*write regime*: -370 pm, *read regime*: -320 pm). **(m)** Histograms of the binary numbers determined from digitization of the line scans in (j-l). The scale bars in (d) and (i) are 3 nm. Tip heights are in reference to an STM constant current setpoint of -1.8 V and 50 pA measured over H-Si.

of the pair we observe the opposite (Fig. 5.3j,m 18% *vs.* 73%, respectively). This indicates that other charged species (*e.g.* dangling bonds or ionized donors) act as an additional electrostatic bias on this structure, however, these hidden biases can be counteracted by patterning additional dangling bonds in the structure's surrounding area (Fig. 5.8). Using the techniques previously described the central charge could be manipulated to selectively occupy the right (Fig. 5.3k, 92%) or left (Fig. 5.3l. 67%) dangling bond of the pair, corresponding to the ground and excited states observed to occur in Fig. 5.3j, respectively. These results demonstrate that ground states can be prepared with high efficiency and the occurrence rate of excited charge states can be strongly enhanced. We note that the charge in the right-hand pair of the asymmetric structure could not be manipulated. We hypothesize this is because the other two charges in the structure act as strong electrostatic biases, and that to observe the excited charge states corresponding to its manipulation would require greater time resolution than was available to us (~ 1 s between write and read phases).

These results demonstrate that charge states in atomic structures can remain trapped for periods on the order of seconds. This is because dangling bonds are electronically isolated from the bulk and lattice relaxation induces an asymmetry in the confining potential. As a result, thermal fluctuations are required to provide the activation energy required for electrons to tunnel or thermionically hop between dangling bonds. This motivates a temperature-dependent study of these phenomena. Our results can be interpreted via electrostatic arguments suggesting atomic systems could serve well as the building blocks for field controlled computing devices. We identify the height dependence of tip induced band bending in AFM experiments at zero bias as the key factor to manipulate and non-perturbatively monitor single electrons confined to atomic structures. The techniques presented here expand the scanning probe toolkit with the ability to position charge within atomic structures and initiate desired charge states, opening the door for future investigations of tailor-made atomic charge configurations and hardware systems modelling designer Hamiltonians.

5.1 | Methods

Experimental Setup: All experiments were performed on a home built system incorporating an Omicron LT STM/AFM operating at 4.5 K and ultrahigh vacuum

($< 1 \times 10^{-10}$ Torr). The tip was created from polycrystalline tungsten wire that was chemically etched and installed to a qPlus sensor [117]. The tip was driven with an amplitude of 50 pm at a resonance frequency of 28 kHz and Q-factor of 14×10^3. An additional electrode on the sensor is used to supply tunnelling current. Tips were further processed with electron bombardment to remove the surface oxide, and sharpened by nitrogen etching while performing field ion microscopy [57]. In-situ tip processing was performed by controlled contacts with the tip to the sample surface. Samples were cleaved from (100)-oriented Si crystals that are highly As-doped (1.5×10^{19} atom cm^{-3}). After degassing at 600 °C for $\sim$ 12 hours, samples were flash annealed to temperatures as high as 1250 °C before passivating the surface with hydrogen while maintaining a sample temperature of 330 °C. These high flash temperatures have been previously shown to induce a dopant depletion region extending as far as 100 nm below the sample surface [70].

5.2 | Supporting Information

Error Rate: Throughout measurements restricted to the *read regime* we occasionally observed negative charges occupying both dangling bonds in a pair, despite this being unlikely due to Coulombic repulsion. We define these line scans as errors. While it was typically several percent we have achieved error rates of $< 1\%$ (Fig. 5.5). We have identified several contributing factors. (i) The *read* and *write* regimes are sensitive to the tip height (Fig. 5.3). Accordingly, we find that small changes in tip height can occasionally result in unintentional dragging in the *read regime* causing the same negative charge to be measured twice, or influence our ability to control the negative charge in the *write regime*. (ii) Sharp tips were found to more clearly resolve the two charge states of each dangling bond. This reduces the number of incorrect charge state assignments, which are performed in a digital fashion. Similarly, with H-terminated tips, which can be effectively identified via force distance spectroscopy, [29] it was more difficult to discriminate the two charge states each dangling bond.

Data Processing: Minimal data processing was performed and raw data was used whenever possible. All experiments with repeated line scans were performed in constant height mode. For experiments performed entirely in the read regime, forward and backward line scans, which are saved in separate files by the control

software, were aligned manually by removing an equal number of pixels at the start of both scans and zipped together (step 1, Fig. 5.4b). Measurements often exceeded 30 minutes, over which time the tip would inevitably drift towards or away from the surface due to piezo creep and thermal drift. To account for this, a linear drift was subtracted from all measurements with repeated line scans by fitting the average Δf for each line scan over the course of an experiment (step 2, Fig. 5.4c). In experiments where Δf drifted by more than 2 Hz the entire run was rejected.

The Δf value measured over each dangling bond was extracted by independently fitting each dangling bond associated peak in the line scans (defined by pixels) with a Gaussian function (step 3, Fig. 5.4d). When dangling bonds were neutral, this corresponded to fitting the Δf associated with the background noise/hydrogen, and therefore the peak of each Gaussian was constrained to a 30-pixel window centered on each dangling bond. Supporting Figure 5.4e,f shows the extracted Δf values for two dangling bonds. The bistable behavior of each dangling bond is clearly visible.

Binary numbers were assigned to the charge states by making a single cut in Δf (Fig. 5.4e,f demonstrate cuts). Dangling bonds with Δf more negative than the cut (larger absolute Δf) were assigned a negative charge state, while those with Δf more positive than the cut (smaller absolute Δf) were assigned a neutral charge state (Fig. 5.4e,f). Two additional steps were used to create the histograms in Fig. 5.6 and 5.7. First, the largest Δf in the set of the Δf extracted for all the dangling bonds in an experiment (corresponding to a fit of the background) was set to 0 (step 4). Thus, the normalized Δf for all the dangling bonds would be positive. Second, each Δf was normalized by setting the average Δf to 1.0 (step 5). Because the isolated dangling bonds were always negatively charged, a normalized Δf of 1.0 corresponds to the average Δf for a negatively charged dangling bond. Similar to the process above a single common cut in Δf was used to assign charge states to the normalized data (step 6).

Potential energy of DBs during AFM imaging: The eigenenergies of a single DB in neutral and negative states are estimated to be E(DB) = −320 meV and E(DB0) = −770 meV with respect to the bulk conduction band maximum (CBM) at flat band conditions [27]. The valence band minimum (VBM) in silicon is −1.17 eV with respect to the CBM at temperatures close to 0 K. We therefore identify

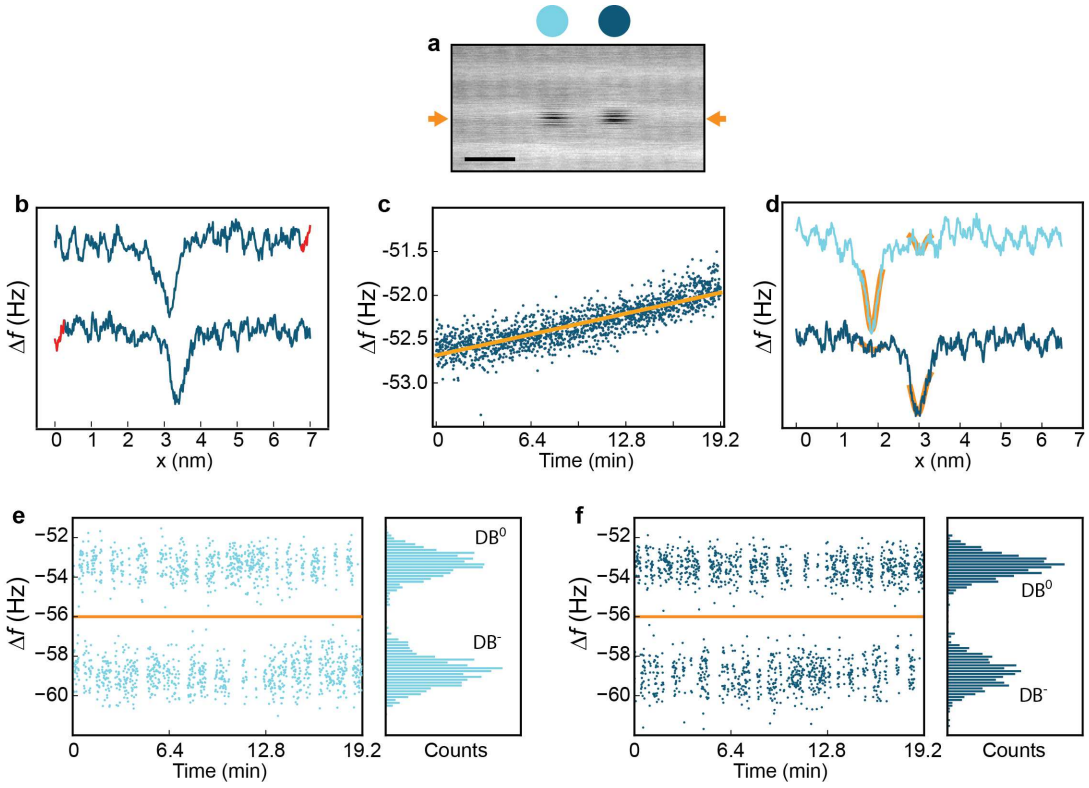

Figure 5.4: Illustration of data processing routine. **(a)** Constant height Δf image of a dangling bond structure taken at 0 V. The initial tip height is set on a hydrogen atom at -1.8 V and 50 pA before moving the tip 300 pm towards the surface. The scale bar is 1 nm. **(b)** Two sequential Δf line scans demonstrate negative charge confined to the righthand dangling bond (line scan width is larger than the window shown in (a), line scans are offset for clarity). The peaks are not aligned because they correspond to forward (top) and backward (bottom) line scans, which typically have a fixed offset due to piezo creep. The red tails on both line scans demonstrate the data that is chopped to align the scans. **(c)** The average Δf of each line scan over the course of the entire experiment demonstrates that the tip was slowly drifting away from the sample. A linear fit of this data (orange line) is subtracted from the dataset. **(d)** Each line scan is fit with two gaussian peaks to extract the Δf over each dangling bond (colour legend indicated above (a)). Note that for neutral dangling bonds this corresponds to a fit of the signal associated with hydrogen/noise. **(e,f)** The Δf extracted for each dangling bond clearly displays two distinct states, which we assign to the negative and neutral charge states of each dangling bond. Each histogram has 75 equal width bins between $\Delta f = -62$ and -51 Hz, and has an integrated area of 1.0.

the ways in which the tip contributes to the potential energy of DBs during non-contact AFM imaging at zero bias: (i) a shift in energy landscape due to the tip-sample contact potential, known as tip-induced band bending (TIBB) and (ii) an image charge contribution to the potential energy, dubbed image-charge-induced band bending (ICIBB). The AFM tip was assumed to have a work function of 5 eV and an apex radius of 5 nm while the sample work function was taken to be 4.1 eV. A 3D finite-element Poisson equation solver was employed to calculate TIBB [1]. The image charge was calculated using a dielectric constant of 6.35, equal to the average of vacuum and silicon dielectric constants because the lobes of the dangling bonds extend into both mediums. The results are summarized in Fig. 5.2f, showing the two energy components at zero bias as a function of tip height. The numerical results in Fig. 5.2f show that the TIBB (contribution of contact potential difference between the tip and the sample) is upward and is counteracted by the image charge component, which remarkably has an approximately 1/z dependence on tip height z and becomes very important at small tip-sample separations where it can locally exceed TIBB, thus rendering the total potential energy felt by the electron to be negative. Therefore, the electron on a negative dangling bond can be greatly stabilized by the ICIBB as depicted in Fig. 5.5a. As a result, these combined energy shifts render the level of the single negative dangling bond state lower than the Fermi level of the tip by about 170 meV and, as the tip is within the tunnelling range of the dangling bond, the latter acquires a net negative charge. However, as tip height is increased, the total potential energy of the DB electron increases (even though TIBB decreases) to the point where the DBstate is brought above the tip Fermi level and the localized DB electron tunnels into the tip rendering the DB neutral. As a side note: the effect of coating the AFM tip with silicon material (as some reports have indicated occurs due to *in-situ* tip preparation via controlled contacts with the surface) results in a lower work function of the tip, and therefore a reduced TIBB. It also decreases the image charge potential by increasing the effective separation between the metal and the dangling bond charge center.

However, when a few dangling bonds are assembled in a system such as those in Fig. 5.2 and Fig. 5.3, their charging states become selective according to the mutual repulsion among them in order to minimize the total energy of the system. For

example, in experiments conducted in the *read regime*, excessive Coulomb repulsion between two close dangling bonds (0, 1, or 2 H atoms apart) prohibits equal charging of these dangling bonds, and only one extra electron is allowed in such a pair. This situation is depicted in Fig. 5.5b where two dangling bonds are assumed to be separated by one H atom, as are the two dangling bond pairs in Fig. 5.1. If one of the two dangling bonds were negatively charged, the repulsion energy at the site of the other dangling bond (which we dub the perturber-induced band bending, PIBB) amounts to $\sim$ 280 meV, as calculated by simple electrostatics using point charges and a dielectric constant of the surface of 6.35. In addition to this, the PIBB from the far dangling bonds increase the potential energy of middle dangling bonds even more by a few tens of meV. This brings the total potential energy at that site to above the Fermi level by about 100 meV, such that the dangling bond is neutral. Note that, importantly, in the write regime the ICIBB can increase in magnitude by more than 100 meV if the tip height is below 200 pm (Fig. 5.2f). This has the effect of bringing the negatively charged dangling bond level below the Fermi level of the tip and both dangling bonds are seen to harbor a negative charge during this phase (Fig. 5.2b).

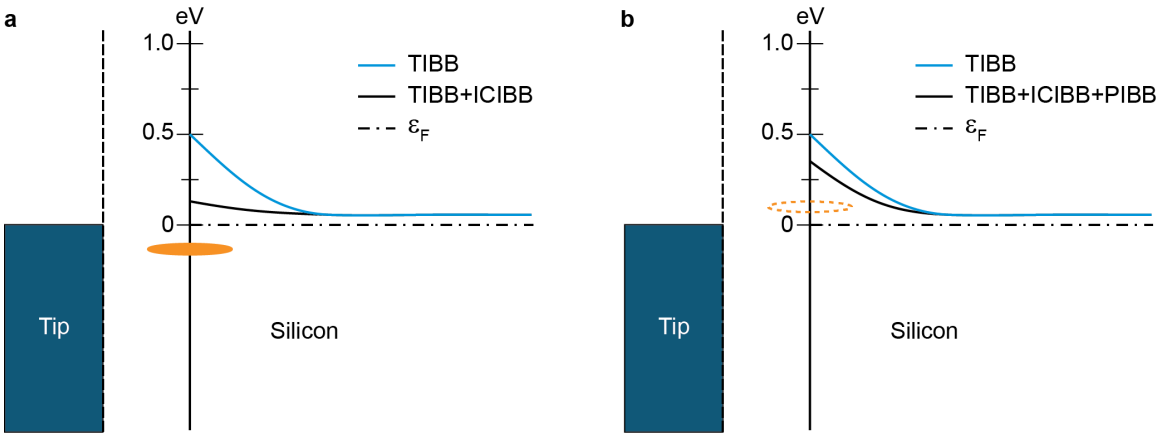

Figure 5.5: Potential energy diagram for an isolated dangling bond at zero bias and with a small tip-sample separation. **(a)** At small tip height, the electron is stabilized on a DB by the effect of the ICIBB counteracting the TIBB, such that the level of the DB state (filled orange oval) is lower than the Fermi level of the tip (upper edge of the blue rectangle) and thus is stably occupied. The graph also shows potential energy variations (band bending) as a function of sample depth (horizontal axis), where the dash-dotted line is the sample Fermi level and the solid curves represent the CBM. **(b)** If a DB is located near some other DB, already negative, there is another component (PIBB) to the total potential energy coming from the Coulomb repulsion. This renders the total energy of the DB- level (empty orange oval) above the Fermi level of the tip and the sample, therefore keeping that DB neutral.

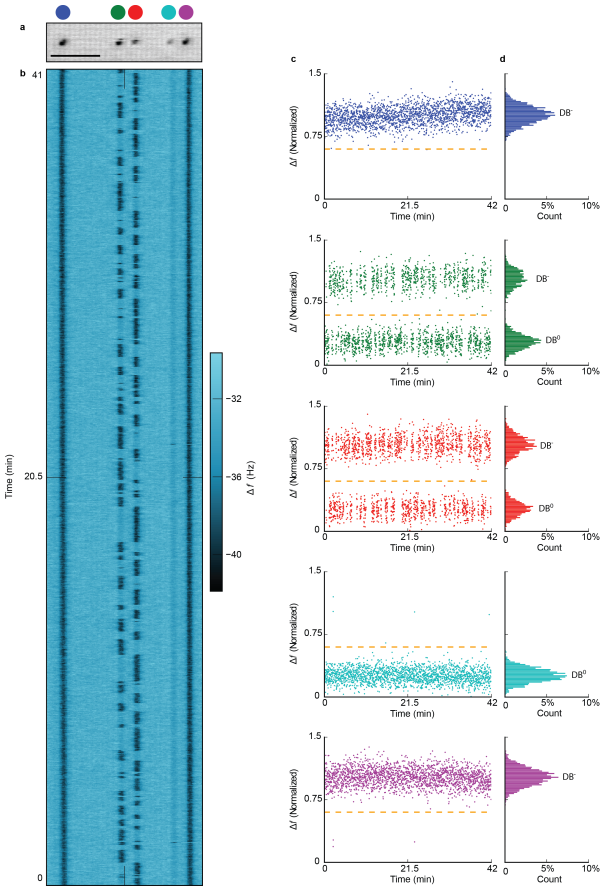

Figure 5.6: Digitization of line scans of an asymmetric structure composed of five dangling bonds. **(a)** Constant height Δf image of the dangling bond structure at 0 V. **(b)** A line scan map composed of 2048 Δf line scans acquired in the read-regime (-300 pm) over the structure. **(c)** The normalized Δf acquired over each dangling bond throughout the course of the experiment demonstrates clearly that there are two charge states of each dangling bond (although only the green and red dangling bonds appear to fluctuate between them). With the normalizing procedure described above the negative dangling bond charge state is normalized to a Δf of 1.0, and the Δf of the neutral dangling bond state is centered approximately at 0.25. The orange dotted lines demonstrate that a single common cut of $\Delta f = 0.6$ in the normalized data can be used to digitize the charge state of the structure with each line scan. **(d)** Histograms of the normalized Δf for each dangling bond reveal that the Δf corresponding to the two charge states of each dangling bond have a Gaussian distribution. Upon assigning binary numbers to this dataset it was found that in $< 1\%$ of the line scans the charge configuration corresponded to having a third negative charge in the four paired dangling bonds. Each histogram has 75 equal width bins between $\Delta f(\text{normalized}) = 0$ and 1.5, and has an integrated area of 1.0.

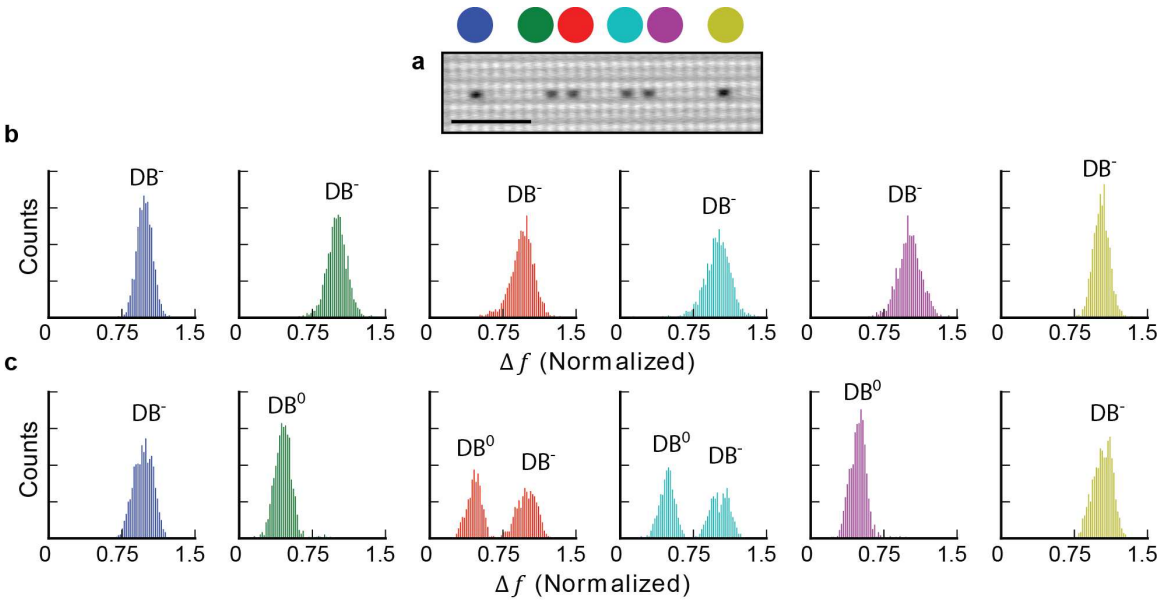

Figure 5.7: Histograms of the normalized Δf measured over each site in a symmetric six dangling bond structure at different tip heights. **(a)** Constant height Δf image of the structure. Histograms of the normalized Δf measured over each dangling bond at **(b)** z = −320 pm and **(c)** z = −270 pm. 1600 line scans at both heights were used to gather statistics. Each histogram has 75 equal width bins between Δf(normalized) = 0 and 1.5, and has an integrated area of 1.0. All the dangling bonds appear negatively charged in (b). In (c), the isolated dangling bonds on either end (blue and yellow) remain negatively charged while the outer atoms of each pair (green and purple) are neutral. In (c) the inner atoms (red and cyan) fluctuate between the neutral and negative charge states; the integrated area of each peak is approximately 0.5, indicating they are equally likely to be in the neutral or negative charge state. This can be seen directly in Fig. 5.2d where a single electron switches between these two dangling bonds.

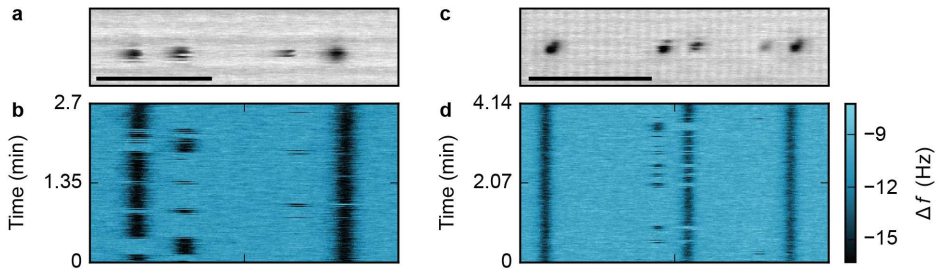

Figure 5.8: The influence of adding an isolated dangling bond on the polarization of dangling bond pairs. **(a)** Constant height Δf image of a symmetric structure composed of four dangling bonds. **(b)** A line scan map composed of two hundred sequential Δf line scans acquired over the structure demonstrate that it is naturally polarized. The negative charge confined to the left-hand pair favours the outer dangling bond but occasionally fluctuates to the inner dangling bond. The negative charge confined to the right-hand pair almost exclusively occupies the outer dangling bond. **(c)** An isolated dangling bond was added to the left of the same structure in (a) using STM lithography. **(d)** A line scan map composed of two hundred sequential Δf line scans acquired over the structure demonstrate the effect of this additional negative charge to the polarization of the structure. The right-hand pair remains polarized in the same way as (b). The polarization of the left-hand pair reverses compared to (b). This is easily rationalized by noting that the new dangling bond acts as a new local Coulombic bias. This demonstrates that local charges (*e.g.* negatively charged dangling bonds or ionized donors) can influence the distribution of charge states these structures display. The scale bars in (a) and (c) are 3 and 4 nm, respectively. The individual line scans acquired in (d) are longer than in (b) due to the increased distance the tip has to move. The Δf colour bar applies to both (b) and (d).

6 | Correlated Switching and Charge State Lifetime

6.1 | Correlated Switching

One aspect of the line scan maps not yet discussed is whether we observe any correlations between the sequence of charge configurations observed. For example, one might assume that in the sequential *write* then *read* experiments, (Figure 5.3 f,g,k,l) unsuccessful manipulations of the electrons might be correlated with abnormal scans recorded in the *write* phase. This could be investigated by comparing the digital states observed in the *write* and the following *read* phase. A correlation would be manifested by an increase of the counts of a specific charge configuration, relative to an experiment restricted to the *read* regime, when a deviant *write* scan preceded it.

As an example, we performed this analysis on Figure 5.3f. Unexpectedly, we found little evidence for a correlation between the 9% of deviant *write* scans (the structure did not appear fully occupied) and the *read* scans that followed. Analysis of the experiments depicted in 5.3g,k,l yielded the same. Unfortunately, it is difficult to ascribe whether the lack of correlation between deviant *write* and *read* scans is real, or simply a result of a small sample size (approximately 20 deviant scans per dataset). This motivates future experiments with larger datasets to determine if there is a correlation between unsuccessful charge manipulation and deviant *write* scans.

We also might expect to observe correlations between the charge configurations of subunits within large DB structures. If such correlations exist, they should be observed in structures with multiple pairs of DBs that each localize a single negative charge. As an example, the structure shown in Figure 6.1A was created by adding an isolated DB to the right of the structure shown in Figure 5.8c. Unlike the six DB structure studied in Figure 5.2, both pairs in this structure localize a negative charge. The linescan map depicted in Figure 6.1B was recorded in the *read* regime over a period of eleven minutes. It clearly shows that both of the interior charges fluctuate between the DBs of each pair (unlike in Fig. 5.8c) because the isolated DBs on either end act to balance the electrostatic perturbations experienced within the structure. It is important to note that the intrinsic polarization of the structure observed in Figure

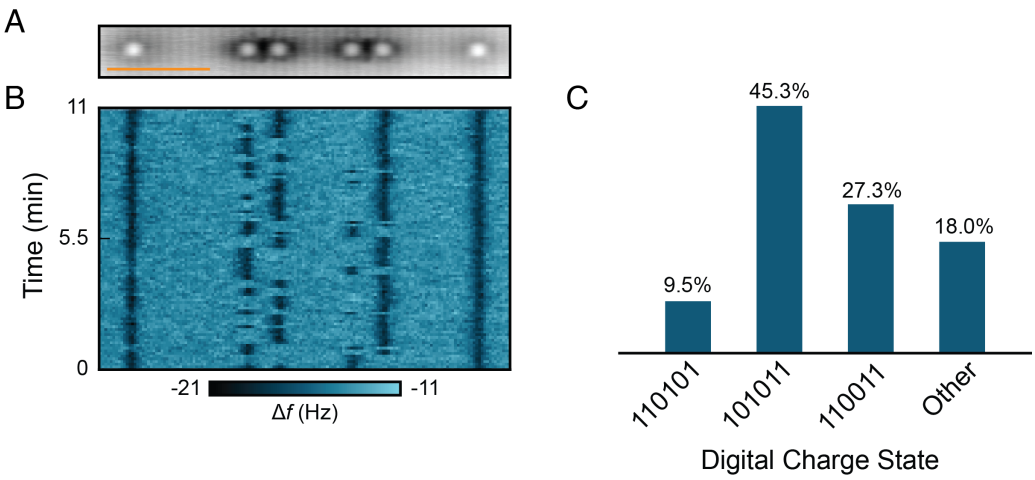

Figure 6.1: Charge switching in an asymmetric six DB structure. **(A)** A constant current STM image of the DB structure (1.3 V, 50 pA). Scale bar is 4 nm. **(B)** A linescan map in the *read* regime (0 V, −320 pm, 400 lines). **(C)** The occurrence rate of the dominant digital states observed in (A). Line scans were digitized according the procedure described in Figure 5.4. 1s correspond to negatively charged DBs, and 0s to neutral DBs.

5.8A persists (likely due to the influence of ionized subsurface donors [71, 72, 102]), with the negative charge of the right hand pair strongly preferring the right DB of the pair, but that the addition of the sixth DB on the right of the structure does weaken this effect because of its Coulombic influence.

By digitizing the data with the procedure described in Figure 5.4 we are able to compare the number of times each digital charge configuration was observed (Figure 6.1C). As expected, we do not observe many line scans where the two innermost DBs are both charged ($< 3\%$), likely because of the high Coulombic repulsion that would exist between the inner charges of such a state. If we restrict our attention to the four inner DBs, that leaves three other possible charge configurations (assuming that each DB pair always retains a single negative charge): the left DBs of both pairs can be negatively charged (observed in 9.5% of line scans), the right DBs of both pairs can be negatively charged (45.3%), or the outer DBs of both pairs can be negatively charged (27.3%).

It is of technological interest to design a structure where the only charge states are those where the left or right DBs of both pairs are negatively charged. If such a structure were to be extended to include many pairs, an electrostatic stimulus

applied at one end of the wire would be cascaded along the wire [2]. In this case, the polarization of the last pair would be an indication of the stimulus applied to the first. This is the idea behind the BASiL binary wire which is discussed further in Chapter 8. The structure in Figure 6.1 does not demonstrate the desired behaviour. Indeed, of the 85% of scans that had one negative charge per pair (*i.e.* not defined as errors) only 65% of the measurements corresponded to both the left or both the right DBs being charged. However, the experiment does demonstrate that Δf linescan maps can be used to characterize prototype BASiL wires.

6.2 | Charge State Lifetime

An obvious follow-up experiment to those depicted in Figure 5.3 is to determine the lifetime of the prepared charge states. This could be done in two ways. First, one could perform a *write* scan and apply a variable length delay before the follow-up *read* scan. Second, one could perform several *read* scans instead of just one, and count the number of *read* scans that the prepared state remains unchanged. In both cases one would expect that for short delays, the prepared charge state would remain relatively stable, but that as the delay was increased the likelihood of observing any given charge state would match their occurrence rate as observed in experiments restricted to the *read* regime.

It is interesting to note that while these two variations are similar to one another, the former could be used to provide evidence for whether or not a prepared charge state remains stable even in the absence of a tip. To achieve this, during the delay between the *write* and *read* scans the tip could be moved away from the structure. A lateral distance of 10 nm would be sufficient to eliminate the image charge band bending, but would likely be a small enough distance to guard against excessive piezo creep. This is an important aspect of these experiments that has not yet been explored, because if the image charge band bending is not required to stabilize the charge states these techniques should be suitable for preparing charge states on larger structures that will require the tip to move away from any given DB.

A limited version of the second experiment has already been performed in conjunction with the experiments depicted in Figure 5.3. In the commercial control software (Nanonis) for the microscope the default scan is comprised of both forward

and backward sweeps of the tip. Rather than program our entire control sequence from scratch, we utilized this basic feature. Therefore, the true scanning sequence of the experiments was a forward and backward sweep in the *write* regime, followed by a forward and backward sweep in the *read* regime. The schematics depicted in Figure 5.3b,c depict only the directly relevant components of this sequence, namely the two middle steps. Because the backward sweep in the *read* regime was recorded, however, it can be analysed independently.

We find that the state prepared in Figure 5.3f decays from 86% to 79.5% between the forward and backward linescans ($\sim$ 1 s delay). The other degenerate state sees an increase in occurrence from 7.5% in the forward scan to 15% in the backward scan, indicating that in most cases the electron simply switches to the other interior DB as expected. The behaviour observed for the experiment depicted in Figure 5.3g is similar.

It is more interesting to compare the forward and backward linescans for the experiments depicted in Figure 5.3k,l because the two dominant charge states are not degenerate in energy due to the structure's asymmetry. Here we find that the ground state prepared in Figure 5.3k decays from 93% to 82.4%, while the excited state prepared in Figure 5.3l decays from 67% to 51%. Notably, for the latter experiment the ground state surges from only 8% to 42% over the same period, indicating the excited charge states prepared by the *write* scan predominantly relax to the ground state.

With these approximate measures of how likely a prepared charge state is to decay within a 1 s period we can estimate their lifetimes if we assume two things: that each sequence of linescans is independent, and that the charge state switches as a result of the system traversing over an energy barrier. If we do so we can model the decay process as a zeroth order process, *i.e.* the probability of decaying in any given time is constant. In this case:

$$\frac{dN}{dt} = -\lambda N \tag{6.1}$$

where N is the population of the given state and λ is the decay constant. The solution of this first order differential equation is simply:

$$N(t) = N_0 e^{-\lambda t} \tag{6.2}$$

where N_0 is the population at $t = 0$. In this case λ can be found by comparing the populations at two moments in time:

$$\lambda = \frac{\ln\left(N(t_1)/N(t_2)\right)}{t_2 - t_1} \tag{6.3}$$

Using the values mentioned above for the symmetric structure we find λ is approximately equal to 0.08 s^{-1} and 0.12 s^{-1} for the degenerate ground states prepared in Figure 5.3 f and g, respectively. This corresponds to half-lives of 9 s and 6 s, respectively, which agree closely to the lifetimes inferred by counting the number of sequential read scans in in Figure 5.3e. For the asymmetric structure we find the λ for the ground and excited state to be 0.12 s^{-1} and 0.27 s^{-1} corresponding to half lives of 6 s and 3 s, respectively. While the half-life of the excited state is shorter than the ground state, it is of the same order of magnitude. This suggests that even though the excited charge state was more difficult to prepare, it did not decay much faster.

Finally, we can also use these measures to estimate how successful the initial state preparation is, because the *read* scans depicted in Figure 5.3 also take ~ 1 s to collect. For the symmetric structure the two states were initially prepared with 93% and 90% fidelity. For the asymmetric structure the ground and excited states were prepared with $> 99\%$ and 88% fidelity, respectively.

It is important to stress that for the analysis above it was assumed that a zeroth order process was a good model, and that the statistical significance of the measures used was low. This model could be validated in future experiments by verifying that the probability of observing a switch from a given charge state actually increases exponentially in time, by making many measurements of its lifetime with more time points.

7 The Switching Mechanism

After completing the experiments described in Chapter 5 there remained several important questions about the underlying physics that prevented their complete interpretation. First, it was unknown whether the electrons thermally hop between sites or tunnel. Second, it was unclear how strongly the tip interacts with the dangling bonds while in the *read regime*. These two questions are intimately related. If while in the *read regime* the tip is essentially non-interacting then the switching rate can be fully accounted for by only considering the physics of the surface. On the other hand, if the tip is interacting, even if it does so only weakly, then the observed switching rate would likely be affected.

First, we note that because the DBs are closely spaced, theory has predicted that electrons confined to the DBs should tunnel between the sites with THz rate [85,102]. Notably, however, this estimate is only valid in the absence of lattice relaxation. Because we observe switching rates on the order of seconds in experiment facile tunnelling cannot explain switching.

Because of this, in Chapter 5 it was suggested that the charge traps because of relaxation of the lattice. These relaxations have been predicted by theory [83,118,119] and have been observed directly in other material systems [23, 115]. The free energy associated with these lattice relaxations found by references [83,118,119] are for when a neutral dangling bond becomes negatively charged. This is clearly distinct from the energy barrier associated with switching which of two closely-spaced dangling bonds are negatively charged. For example, the change in the equilibrium position of atoms in close proximity to the pair may not change substantially between the two charge configurations, in which case the energy barrier would be a fraction of the lattice relaxation energies found by references [83, 118, 119]. If the barrier for switching were sufficiently small, thermal excitations could still be involved in the mechanism responsible for switching, even though they could not be responsible for the charging of an isolated dangling bond.

Still, because the experiments were performed at 4.5 K it is very unlikely that thermal excitation plays a significant role in the switching mechanism, because 4.5 K

corresponds roughly to 0.4 meV. It is therefore essential that we work to characterize the tip's influence on the types of measurements presented.

7.1 | Characterizing the Tip's Influence

Initially after performing the experiments in Chapter 5 we were optimistic that the tip was interacting weakly with the DB structures while in the *read regime*. If so, the switching we observed could reasonably be expected to occur even in the absence of the tip and our experiments could be used observe the *natural* switching that occurs among DBs.

There were two main reasons to be optimistic. First, the switching rate we observed was extremely slow relative to the oscillation rate of the cantilever and its movement across the structure. This is clearly distinct from the class of nc-AFM experiments where the tip is been used to drive the transition of single electrons between the bulk and the local structure, *e.g.* references [22, 120]. It is also distinct from the charge manipulation experiments of adsorbates on thin insulating films, because there the charge state of individual adsorbates remain stable during measurement, *e.g.* references [25, 26]. We therefore contend that if the tip were interacting strongly it would be unlikely for the charge states to persist over many consecutive measurements, as we observed. Second, theory suggests that at specific heights it is possible for the overall band bending beneath the tip to be negligible because of the opposing CPD and image charge contributions. Because in the *write regime* the tip had to be close enough for the image charge contribution to be dominant, it was reasonable to suspect that by withdrawing the tip to the *read regime* the overall band bending could be cancelled. To verify our hypotheses we performed several related experiments.

7.1.1 | Determining the Onset of the *Write Regime*

In the first experiment we looked to characterize the tip offset at which the *write regime* begins by varying the oscillation amplitude of the cantilever (Figure 7.1). To do so, we fabricated a pair of closely-spaced DBs, a structure that is known to hold a single negative charge. By withdrawing the tip 200 pm before beginning a $\Delta f(z)$ spectrum we hypothesized that the DB under the tip would become neutrally charged because the CPD would be larger than the image charge contribution. In this regime,

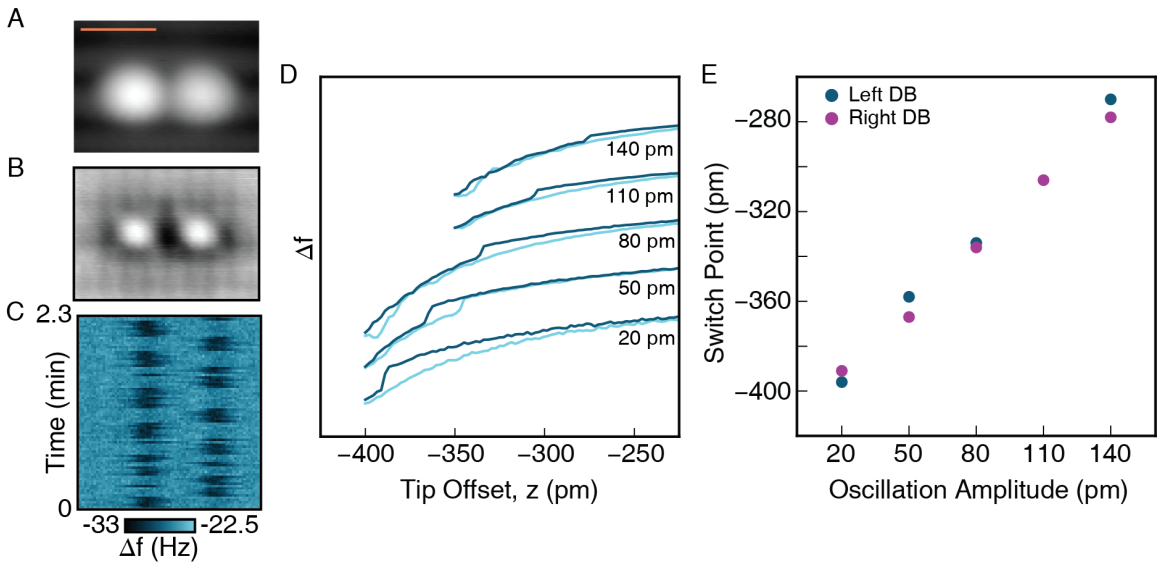

Figure 7.1: The effect of tip oscillation amplitude on the onset of the *write regime*. **(A,B)** Constant current STM images of a pair of DBs at -1.8 V and $+1.3$ V, respectively. The current setpoint was 50 pA for both. **(C)** A Δf line scan map of the pair in the *read regime* ($z = -300$ pm, $A = 50$ pm, 0 V) demonstrates that the pair equally share a single electron. The scale bar in (A) is 2 nm and applies for (A-C). **(D)** $\Delta f(z)$ spectra taken on top the DBs (spectra from right DB shown) demonstrate a large hysteretic step as the tip approaches the DB (tip approaching, dark blue, tip withdrawing, light blue). Labels correspond to the oscillation amplitude of the cantilever. Individual spectra are vertically offset for clarity. **(E)** Plots of the point at which the hysteretic steps from (D) occur as a function of the cantilever's oscillation amplitude for both the left (blue) and right (purple) DB reveal a linear relationship.

the electron would be repelled from the tip and preferentially occupy the other DB. In addition, we switched DBs for each $\Delta f(z)$ measurement, such that if we positioned the charge in the DB during the previous measurement, the next measurement would begin on a neutral DB. Hysteretic jumps in Δf were subsequently observed as the tip approached the sample. Because these jumps always resulted in increases to $|\Delta f|$ we conclude that they can be attributed to the DB under the tip becoming negatively charged as the tip passes into the *write regime* and attracts the electron to the DB beneath it.

By increasing the oscillation amplitude of the tip we found a corresponding decrease in the tip-offset required to observe the hysteretic jumps (Figure 7.1D,E). We note that by monitoring the pair of DBs from the *read regime* we found they appeared to share the single electron equally (Figure 7.1C). This is an important requirement for this and subsequent experiments because an external bias would make it easier to draw the electron to one DB and more difficult to draw it to the other. A plot of the tip-offset at which the hysteretic jumps occurred as a function of the oscillation amplitude reveals a linear dependence (Figure 7.1E) that is nearly identical for the left and right DBs (blue and purple dots, respectively).

That the slope observed in Figure 7.1E is almost exactly 1 is surprising. The oscillation amplitude of the tip is measured from the bottom of its motion to the top. If the closest approach of the tip was what determined the onset of the *write regime*, as we expected it would, the observed slope would have been 1/2. A future experiment could attempt to isolate the short range forces acting between the tip and cantilever by converting the $\Delta f(z)$ curve to force using the Sader-Jarvis method [121, 122]. If the image charge is responsible for the switching mechanism we would expect that the extracted short range force acting between the tip and sample would be fit best by a function with a z^{-2} dependence, and the overall short range force at the moment the charge enters the DB would scale as in Figure 7.1E. If the short range forces between the tip and sample have a different z dependence it would provide evidence that a mechanism other than the image charge is responsible for *writing*.

In Figure 7.1D there are two qualitatively different types of withdraw curves (light blue). For the spectrum taken with $A = 50$ pm the hysteresis is observed only over a small range of the tip offset near -350 pm, indicating that as the tip was

withdrawn the DB became neutrally charged. Each of the other withdraw curves slowly approaches the approach curve (dark blue), becoming indistinguishable at approximately −250 pm. These curves therefore suggest that the charge often remains in the DB beneath the tip even as it withdrawn from the *write regime* over a ~ 1 s period. These spectra also provides us a quick method to estimate the $|\Delta f|$ signal to noise ratio for distinguishing the DB^0 and DB^- states over a range of tip offsets.

7.1.2 | Finding the *Sweet Spot*

The *sweet spot* is the hypothesized tip offset at which the CPD directly counteracts the image charge field. If the *sweet spot* exists, it should be possible to place the tip above a DB and measure charge fluctuations without exerting any influence over them.[1]

To verify the *sweet spot's* existence we performed the series of experiments depicted in Figure 7.2. The idea underlying these experiments is that if the image charge contribution is dominant the overall band bending beneath the tip should be negative, and an electron should preferentially occupy the site beneath the tip. Likewise, if the CPD is dominant, upward band bending should preferentially stabilize an electron in a site not under the tip. Therefore, by measuring the time-averaged occupation of each DB in a symmetric pair, we should be able to conclude if the image charge or CPD fields are dominant. For example, in the case where the CPD is dominant, each of the DBs will hold a negative charge for $< 50\%$ of the time, and the overall time-averaged occupation of the structure will appear to be < 1. Only in the case of a balanced CPD and image charge field would one expect the time-averaged occupation of the whole structure to equal 1.

Figure 7.2A demonstrates two Δf telegraph noise traces obtained by holding the tip over the left DB from Figure 7.1 with a fixed tip offset. As expected, both traces demonstrate fluctuations between the DB^0 and DB^- states (DB^- demonstrate larger $|\Delta f|$). Both the average Δf and the difference in Δf for the two charge states is

[1] Ideally the *read regime* would correspond exactly to the *sweet spot*. We introduce the new terminology because in the previous experiments the *read regime* was determined by observing the time-averaged charge occupation of the structure, which was seen to transition sharply as the tip was withdrawn. This typically corresponded to retracting the tip ~ 50 pm. The theory that supports the hypothesized *sweet spot* followed the experiments, and therefore we did not explicitly attempt to balance the CPD and image charge contributions as we do in the following experiments.

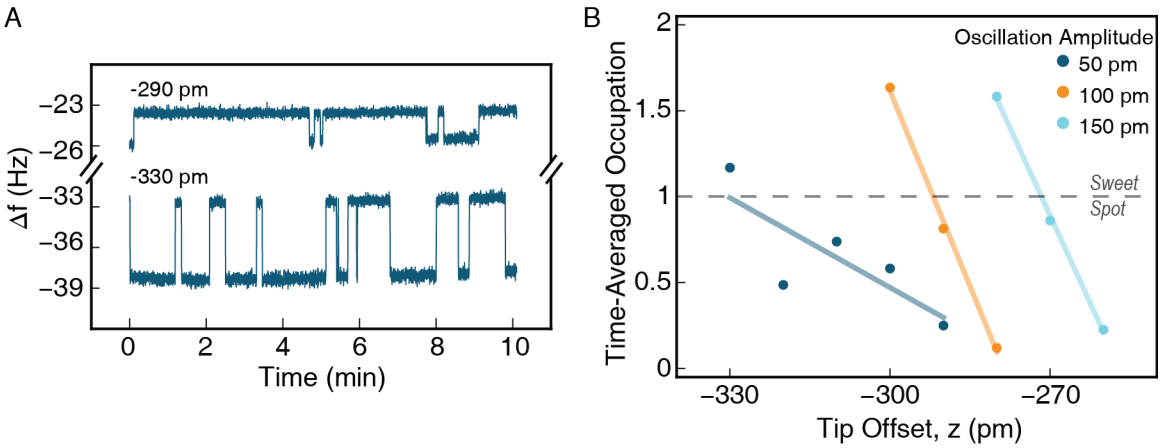

Figure 7.2: The effect of tip-offset on the time-averaged occupation of a two-DB structure. **(A)** Δf telegraph noise measurements taken above the left DB from Figure 7.1 demonstrate fluctuations between the DB^0 and DB^- states. The time-averaged occupation of the DB varies as a function of the tip offset (-290 pm and -330 pm traces labelled). The tip oscillation amplitude was 50 pm. **(B)** The time-averaged occupation of the two-DB structure is found by adding the time-averaged occupation obtained over each DB. The grey dashed line corresponds to the *sweet spot* where the time-averaged occupation of the structure is 1, indicating the tip is not attractive or repulsive to the negative charge in the structure. Coloured lines correspond to a linear fit of the data.

smaller for the trace obtained with a tip offset of -290 pm because the tip is further from the sample. Interestingly, at -290 pm the DB^0 state is observed for longer periods of time than the DB^- state, and the opposite is true for the trace taken at -330 pm.

Figure 7.2B presents the time-averaged occupation of the pair, which was obtained by taking Δf telegraph noise measurements above both DBs in the pair, calculating the ratio of time spent in the DB^- state, and adding them together. For all three of the tip oscillation amplitudes measured, the time-averaged occupation varies linearly over the range of tip offsets measured. Crucially, each of the fits pass through the *sweet spot*, indicating that in principle it is possible to set the tip offset such that the CPD is balanced by the image charge field.

One striking feature of 7.2B is that the slopes of the lines fit to the data vary dramatically between small and large oscillation amplitudes. Presently we do not have any explanation for this. What we do note is that it suggests that small oscillation amplitudes are preferable for experiments where one wants to be at the *sweet spot*,

because the experiment should be less sensitive to small deviations in tip offset.

7.1.3 | The Tip's Effect on the Switching Rate

To further elucidate the tip's influence we studied how the rate at which the negative charge switches between the dangling bonds of a pair is influenced by the scanning parameters.

To complete this analysis we used the Δf telegraph noise traces from the experiments displayed in Figure 7.2A. Whereas previously we calculated the ratio of time spent in the DB^- state, we now count the number of times the DB beneath the tip transitions between the DB^0 and DB^- states. We then calculate the time-averaged switch rate by dividing the number of switches by the length of time the experiment is run for (between 7 and 10 minutes). The data displayed in Figure 7.3 is the switch rate averaged between the left and right dangling bonds.

The switch rate is found to vary strongly with different tip oscillation amplitudes. With large tip oscillation amplitudes (100 pm and 150 pm) the switch rate varies strongly with the tip offset. As the tip approaches the sample the switch rate increases from < 1 to > 5 switches per minute. For small oscillation amplitudes (50 pm) the switch rate is rather insensitive to the tip offset, with an average of < 2 switches per minute.

These results can be rationalized when we take the total band bending predicted in Figure 5.2 into consideration. With large z the first derivative of band bending with respect to z is small. Therefore, even with large tip oscillation amplitudes the total field beneath the tip changes rather little, and always remains in the regime where the CPD is dominant. As a result, the switch rate is small. As the tip approaches the sample however, the first derivative becomes large because the image charge contribution strongly increases, surpassing the CPD. In this case, large oscillation amplitudes drive dramatic changes in the total band bending, transitioning between positive and negative values within each oscillation cycle. As a result, the switch rate sharply increases. Here it is worth noting that the switch rate for an oscillation amplitude of 150 pm appears to have a $1/z$ dependence, like the image charge contribution. In comparison, with an oscillation amplitude of 50 pm the field does not vary as strongly within each oscillation cycle. Consequently the switch-rate

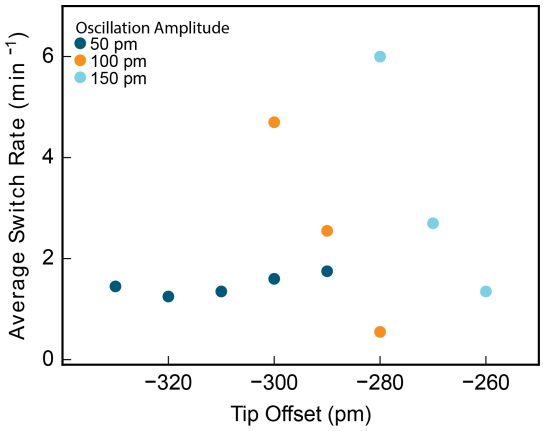

Figure 7.3: The effect of tip-offset on the switching rate of the negative charge in a two-DB structure. Δf telegraph noise measurements were taken by positioning the tip above the left and then right DB of a DB pair and collecting the Δf signal for a period of 7 to 10 minutes (two such traces are displayed in Figure 7.2a). The displayed switching rate corresponds to the time-averaged count of transitions between the DB^0 and DB^- states at each tip offset for the two DBs.

remains relatively constant.

These results strongly suggest that with large oscillation amplitudes the switching we observe is driven by the tip. Even so, it is worth noting that because the switching rate is five orders of magnitude smaller than the oscillation frequency of the tip we can conclude that the interaction between the tip and sample remains relatively weak. If it were stronger, we would expect the switching rate to be orders of magnitude larger, and as a result the Δf signal we would measure would be the time averaged Δf of the DB^0 and DB^- states. For smaller oscillation amplitudes we observe that the switching rate is constant with z, but we cannot conclude if the switching is tip driven or not. To do so would require knowledge of the intrinsic switching rate, which is impossible to estimate given our uncertainty for the switching mechanism. However, these results cast enough doubt to prevent us from claiming that the switching we observe at small oscillation amplitudes is intrinsic.

7.1.4 | Noise Characterization

There are two reasons why it is vital to characterize the sensor's noise. First, it can be used to provide an estimate of what SNR is required to effectively digitize a line scan,

and the operating conditions under which this can be achieved. Secondly, measuring how the sensor's noise correlates with experimental controls can be used to rule out or reinforce hypothesis for experimental observations.

Figure 7.4 presents a detailed noise analysis of a qplus AFM sensor. Data was collected by withdrawing the tip 10 nm from the surface and rastering it over a 5×5 nm^2 area with different tip oscillation amplitudes and scan speeds. Figure 7.4A depicts the Δf noise profiles obtained for a stationary tip (*i.e.* the scan speed was 0 nm/s). The noise profiles are all centred at 0 Hz because there is no tip-sample interaction. As predicted by both Equations 2.32 and 2.33 the noise scales according to $1/A$, with larger oscillation amplitudes having less noise [18]. This would at first suggest that we should scan with larger oscillation amplitudes to maximize our SNR. Instead, we purposefully restrict ourselves to small A specifically because it increases the signal strength. With larger oscillation amplitudes a greater proportion of the tip's motion occurs at heights with weaker tip-sample interactions, actually weakening our ability to distinguish the DB^0 and DB^- charge states. This can be seen in Figure 7.1D by noting that the visibility between the DB^0 and DB^- charge states at the switch point is the largest for the experiment with $A = 20$ pm, and smallest for the experiment with $A = 140$ pm. In addition, Figure 7.3 demonstrates that the tip's interactions with the charge states appears to be stronger with larger oscillation amplitudes, justifying our use of $A = 50$ pm for these experiments.

By fitting each noise profile with a Gaussian function and extracting the standard deviation (σ) we can easily compare the Δf noise for several scan speeds (Figure 7.4B). We find that the faster the tip is rastered the greater the Δf noise. While one would expect that the SNR would scale with the length of time the signal is integrated, this scaling of the Δf noise with the scan speed is an additional burden. As a result there is a clear trade off between the SNR and time resolution in our experiments. To maximize our SNR all of our experiments were performed with a scan speed of 10 nm/s, which is what limited our time resolution to ~ 1 s.

Next we characterized the noise in A. Figure 7.4C demonstrates that the absolute noise in A is rather insensitive to its setpoint. By fitting the noise profiles with Gaussian functions and extracting their standard deviations we can also effectively compare the noise in A at different scan speeds (Figure 7.4D). We see that even at

larger scan speeds the noise in A does not scale strongly with its setpoint. However, as with the noise in Δf the noise does increase with the scan speed. Because these experiments are extremely sensitive to the tip sample separation it is of crucial importance to minimize this noise. This noise analysis helps reinforce our hypothesis for the increase in the switching rate observed in Figure 7.3, even when we take into account the equilibrium offset of the cantilever. If the noise in A did scale with A, one could have explained the increased switching rate as a consequence of the increased uncertainty in the tip's position.

After performing these experiments we questioned whether the noise we observed could be minimized by disengaging the amplitude feedback controller and the phase locked loop. We repeated the experiments in Figure 7.4 with these controls disengaged (not displayed). We found that the Δf noise scaled in the same manner with A and the scan speed, but the standard deviation was ~ 1 Hz greater. Unlike the prior experiments, the noise in A did scale with its setpoint, and was also larger without the controllers engaged. As a result we recommend that these controllers remain engaged during future experiments.

7.2 | Next Steps

Multiple avenues of research should be pursued to conclusively identify the switching mechanism. First, a detailed modelling of charge state transitions, perhaps by time-dependent DFT, would be valuable. This could help provide a better estimate of the exact energy barrier associated with these transitions. Second, variable temperature experiments should be performed on a single structure. If thermal activation is involved in switching between charge configurations, the switching rate should increase dramatically with only modest increases to temperature. Finally, we have demonstrated that the tip is almost certainly involved in the switching process, but further characterization is required. Future experiments should attempt to better balance the tradeoffs associated with managing the Δf noise and the associated fluctuations in the total potential landscape.

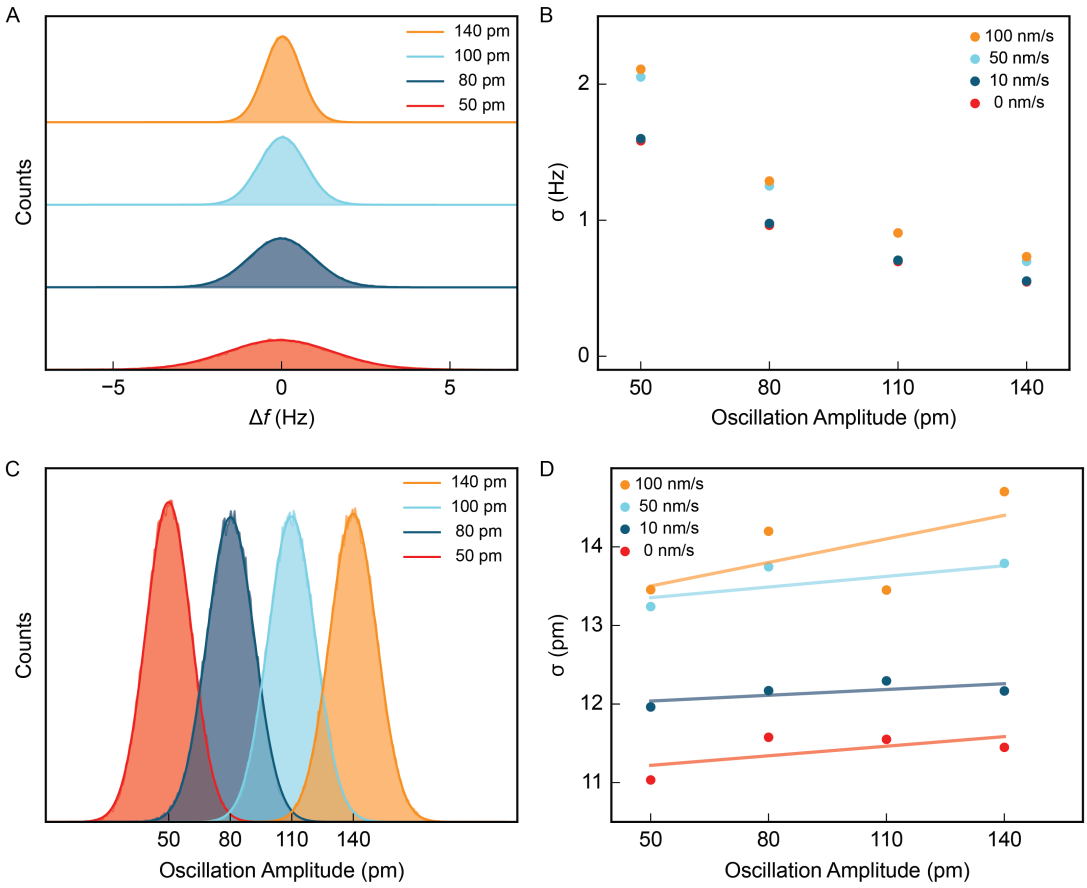

Figure 7.4: Characterization of Δf and amplitude noise. **(A)** Normalized Δf noise for several oscillation amplitudes of a stationary tip. Experimental data is the fill, envelopes are Gaussian fits. Plots are offset vertically for clarity. **(B)** The standard deviation of the Δf noise for several tip oscillation amplitudes and scan speeds. **(C)** Normalized amplitude noise for a stationary tip at several oscillation amplitudes. Experimental data is the fill, envelopes are Gaussian fits. **(D)** The standard deviation of the tip oscillation amplitude for several oscillation amplitudes and scan speeds. For all data the amplitude feedback controller and phase locked loop were engaged.

8 Characterization of a BASiL Gate

The linescan maps presented in the previous chapters can be employed in the characterization of atom-scale technologies. As was mentioned briefly in Section 4.4.5 our group has recently been working on Binary Atomic Silicon Logic (BASiL), [2] a technology that is derivative of quantum cellular automata [98]. In BASiL pairs of closely-spaced DBs form building blocks. As was demonstrated in Figure 5.1 these pairs localize a single negative charge to the left or right DB. The fundamental idea underlying BASiL is that the two distinct charge configurations of a pair may be considered a binary computational basis. Furthermore, as was demonstrated in Figure 5.7, the polarization of DB pairs can be strongly influenced by the addition of negatively charged DBs nearby. As such, these negatively charged DBs can be considered logical inputs, and by combining them with pairs of DBs the transmission and computation of binary information can be achieved.

Figure 8.1 depicts the transmission of binary information along a wire formed from nine pairs of DBs [2]. Because the left-most DB is unpaired and remains negatively charged, the lowest energy configuration for the structure is that in which the right DB of each pair is negatively charged. If the right-most pair is considered the wire's output, then in effect, the output of the wire was forced due to the wire's input (the isolated DB on the left). Crucially, the wire is also capable of transmitting binary information in the opposite direction (displayed in reference [2]) by instead patterning the input on the right-hand side of the structure, in which case the polarization of each pair is reversed compared to Figure 8.1.

In a similar manner a logical OR gate has already been successfully demonstrated, and it is anticipated that a computationally complete gate set is achievable [2]. One surprising aspect of Figure 8.1 is that unlike many of the AFM images seen throughout this thesis none of the DBs appear streaky. This suggests that the ground state charge configuration may be completely dominant for a carefully designed structure. Unfortunately, we do not currently have computational tools that are capable of predicting the ground charge configuration of large DB structures, or the ability to predict if charge switching will be observed in AFM. Similar tools do exist for

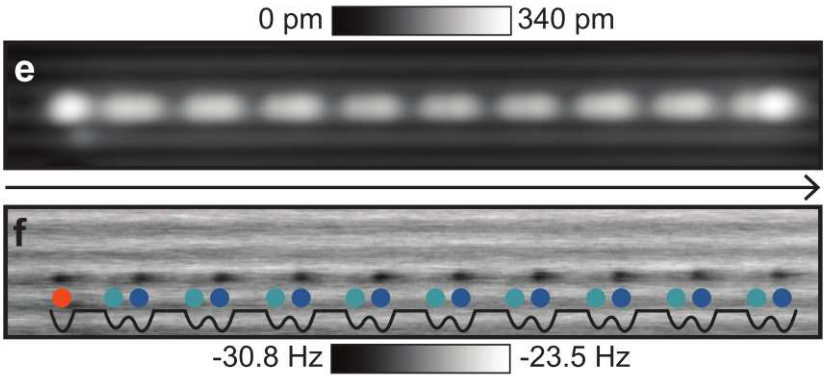

Figure 8.1: BASiL Binary Wire. **(e)** A constant current STM image of the wire taken at −1.8 V and 50 pA. There are nine pairs of DBs biased by a single unpaired DB on the left end of the structure. The DBs in each pair are separated by a single H atom, while the pairs are separated by four H atoms. **(f)** A constant height Δf image of the wire taken at 0 V and $z = -330$ pm. Teal and blue dots indicate the neutral and negatively charged DBs of each pair, respectively. The red dot indicates the negatively charged lone DB. The black line is a sketch of the potential energy landscape, which is polarized due to the isolated DB. Figure taken from [2].

QCA [123]. Until these tools are developed, linescan maps restricted to the *read* regime can be used to characterize DB structures and inform the design of future BASiL logic gates. The utility of this application of linescan maps rests on two critical assumptions: that the dominant charge configuration observed in a linescan map is the structure's lowest energy charge configuration; and if the ground charge configuration is well-separated from other configurations in energy, then few switching events will be observed.

Figure 8.2 is an example of this approach. The structure in 8.2A corresponds to three pairs of DBs. In accordance with the scheme described in Reference [2], the pair outlined in red is considered the gate's output and the pairs outlined in orange and yellow are the gate's two inputs. Each pair localizes a negative charge. For each pair, we define the charge configuration where the left (right) DB is negatively charged to be the 1 (0) state. We expect that for this configuration the output will rest in state 1 and the two inputs will rest in state 0, as a result of the mutual electrostatic repulsion between the three charges. Figure 8.2D,G show that the output and top input show the expected behaviour, while Fig. 8.2J shows that the lower input switched between both states.

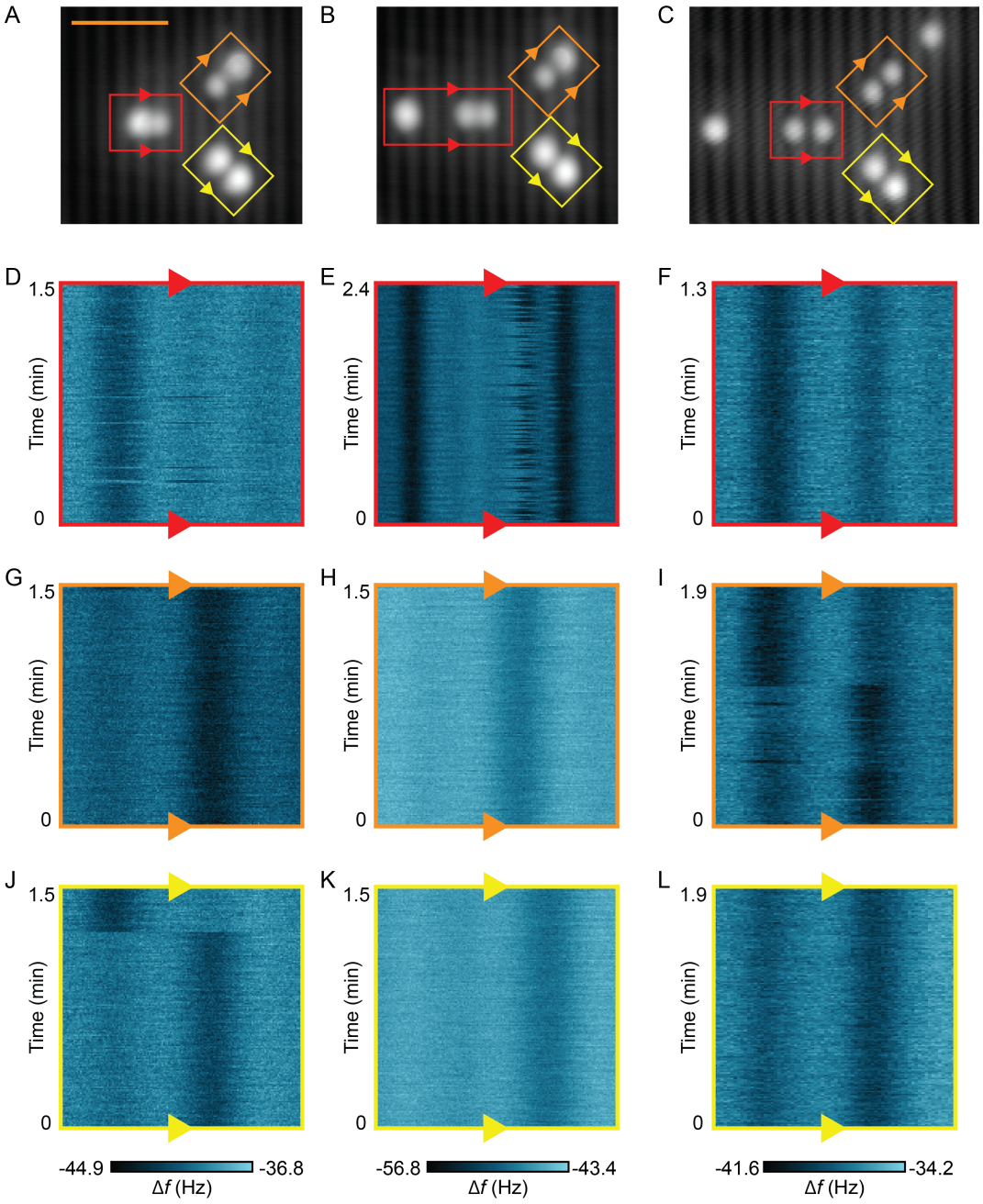

Figure 8.2: The use of linescan maps to evaluate a BASiL gate. (A-C) Constant current STM images of the gate structure (−1.8 V, 50 pA). Scale bar in (A) is 4 nm and applies to (A-C). **(D-L)** Δf linescan maps of the DBs composing the structure (0 V, −280 pm). Coloured borders in (D-L) indicate which DBs were scanned, and correspond to the coloured boxes superimposed in (A-C). Arrows on the coloured boxes indicate the scan direction. The Δf colour bars apply to the line scan maps of each column. The width of each linescan map is 3 nm, except for (E) which is 5.5 nm.

Table 8.1: The truth table for a logical OR gate.

Input	Output
00	0
01	1
10	1
11	1

In 8.2B we pattern a lone DB to the left of the gate's output. The purpose of this DB is to act a weak electrostatic stimulus to shift the gate's output, such that its default output state will be 0 [2]. This should also further stabilize the states of the inputs. The linescan maps in Figure 8.2E,H,K demonstrate the anticipated behaviour, namely that both the output and the two inputs are in state 0.

In 8.2C a lone DB is added close to the upper input. The purpose of this DB is to shift the upper input from state 0 to state 1. Because this additional DB is only close to the upper input gate, we expect that its influence will be largely limited to that pair. If the upper input does respond by shifting to state 1, it will exert a greater electrostatic stimulus on the output than if it were in state 0. Figure 8.2F confirms that the output does indeed respond by switching to state 1. Importantly though, panel I shows that the upper input does not show the anticipated behaviour because it switches between both 1 and 0.

We have observed this behaviour in several similar structures. What we believe is occurring is that by creating large structures with many interacting charges we create many possible charge configurations. If undesirable charge configurations have similar energies to the ground state, we expect from the previous experiments that they might nevertheless occur. What remains unclear to us in this moment is whether the observation of the undesirable charge configurations is only because of the presence of the tip. Because we know that the tip can induce switching, we might expect that without the tip present, the structure would not be capable of transitioning out of the ground state. On the other hand, if we can create structures where similar experiments only observe the desired state, it would provide convincing evidence that the logic gates are robust.

If we observe only the output pair, the structures in Figure 8.2 B and C achieve two of the four behaviours of a logical OR gate (the top two rows of Table 8.1). Unfortunately the other two possible input configurations could not be tested because the tip's quality unexpectedly deteriorated. What is important to highlight from these results, however, is that the linescan maps indicate that in some cases the charge in a pair was fluctuating between the DBs. As was mentioned earlier, this behaviour is

undesirable for the application of binary computation because the output of a gate or circuit should be fully determined by its inputs. Importantly though, this example demonstrates a method to characterize the operation of BASiL gates and it is clear that the information these types of experiments provide could be used to inform new gate designs.

9 Characterization of Subsurface Defects

There are several possible reasons why the gate designed in the previous chapter did not work as anticipated. The spacing of the constituent DBs may not have been optimal. Nearby surface defects may have strained the lattice or acted as electrostatic defects (the gate was patterned within 5 nm of a single atom step). Or perhaps the gate was patterned too closely to subsurface dopants, which distorted the local bands.

All of the experiments presented in this thesis were completed on samples annealed at 1250 °C. As described earlier, flashing the samples to these elevated temperatures results in the formation of a dopant depletion region [70]. In this region, which extends $\sim$ 100 nm beneath the surface, the concentration of dopants is two orders of magnitude lower than the bulk crystal. This is required to align the Fermi level close to the $DB^{0/-}$ level, such that the DBs can be neutral or negatively charged depending on their local environment (in samples without the dopant depletion region DBs are almost always negatively charged). The challenge with working on 1250 °C samples though, is that because the near-surface concentration of dopants is low, the proximity of surface DBs to subsurface dopants varies considerably. We have long suspected that this is ultimately responsible for the non-uniform I(V) properties of isolated DBs on 1250 °C samples [71, 72]. Unfortunately, because the properties of DBs are dependent on their proximity to dopants it is challenging to ascribe whether the undesired behaviour of DB structures is a result of a fundamental flaw in their design or to the existence of a local defect. It is therefore imperative to attempt to characterize the effects of dopants on DBs and map the local distribution of dopants before building a large DB structure.[1]

Subsurface dopants can be located by STM images of the surface [71, 124–128]. We were able to distinguish two dominant species on several crystals. The first cannot be distinguished from H-Si at typical scanning conditions but upon switching

[1] To avoid dopants altogether, members of our group are also currently working to grow epitaxial intrinsic silicon on the surface of highly-doped crystals. In this case, the electronic properties of the crystal would be similar to a crystal with a dopant depletion region, except that the concentration of dopants in the first $\sim$ 5 nm would be orders of magnitude lower. If a high-quality surface can be obtained without high-temperature annealing, which would induce dopant diffusion, this should greatly reduce the affect near-surface dopants have on our measurements.

to constant height mode, decreasing the tip-sample separation, and scanning at small positive sample biases they appear as large bright (conductive) features (Figure 9.1A). Because of this characteristic appearance we refer to them as 'bright defects.' The second appear as small bright features at -1.8 V and as small dark features at $+1.3$ V (Figure 9.1B,C), and we refer to them as 'dark defects.'

To study the bright defects we took $I(V)$ measurements on H-Si directly over the defects and compared them with identical measurements of H-Si with no visible underlying defects (Figure 9.1D). As expected, there were minor variations between measurements of different defects, but two characteristic features emerged. First, the conduction band edge appears at smaller positive biases over bright defects than over H-Si (in Figure 9.1D at ~ 100 meV *vs* ~ 220 meV). Second, there is a step-like turn-on in the tunnelling current at negative sample biases. In Figure 9.1 this step occurred near -1 V, but we observed the steps at biases as low as -375 meV. Crucially, these steps precede the valence band edge which onsets near -1.1 V [40, 71]. It is also important to note that we occasionally observed more than one step in the $I(V)$ spectra.

Both the images and $I(V)$ characteristics of the bright defects correspond strongly to the observations of arsenic dopants made in references [125–127], and so we assign their identity as such. The two characteristic features of $I(V)$ spectra can be rationalized as follows. The conduction band edge occurs earlier over As dopants because at 0 V and small positive biases the As atoms are positively charged under equilibrium conditions [126]. This is because the $As^{+/0}$ level is ~ 50 meV below the Si conduction band, and at small biases the upward band bending due to the CPD causes the dopants to ionize to the bulk [126]. Because the As atom is positively charged it bends the local bands downward (though not enough to counteract the CPD), and therefore smaller biases are required to align the Fermi level of the tip with the conduction band edge.

The steps in current observed at negative sample biases were attributed by Voisin *et al.* [127] to the alignment of the $As^{+/0}$ with the conduction band edge of the bulk *via* tip induced band bending (it is initially above due to upward band bending from the CPD). At this point, a new current channel opens, resulting in an increase to the tunnelling current. The variation in bias at which we observe these steps

can be explained by noting that we can observe As atoms several nm beneath the surface [127]. Because the field is screened by free carriers, a greater bias is required to align the $As^{+/0}$ level of donors deeper below the sample surface. Interestingly, the current typically does not increase substantially between the step and the Si valence band edge. Voisin *et al.* [127] have concluded this indicates the tunnelling current is rate limited by how quickly the As atom ionizes to the tip, rather than how efficiently it is neutralized by current from the bulk.

Here we note one discrepancy with the results of Voisin *et. al* and Salfi *et. al.* [126, 127]. In their work they attributed a second step in $I(V)$ at bias voltages close to -1.0 V to the alignment of the $As^{0/-}$ with the Fermi level of the tip (the first step occurred near -800 meV). While we did occasionally observe a second step in $I(V)$, we also observed species with only one, and in some cases more than two steps. We therefore suggest an alternative explanation for these steps, which is that the $As^{+/0}$ level of other nearby dopants are also brought into resonance with the bulk conduction band edge. Because Voisin *et. al.* [127] suggested that the $As^{0/-}$ level is only 2 meV below the conduction band edge we believe our inconsistent observation of a second step in $I(V)$ measurements provides reasonable evidence to suggest that the $As^{0/-}$ level is pushed above the conduction band edge for near surface donors.

In Figure 9.1E we compare the $I(V)$ spectra of the dark defect with H-Si. The two spectra match closely, with two slight deviations. At negative biases the conductance measured over the dark defect is greater than H-Si, while at positive biases it is less. These observations are consistent with the dark defect being negatively charged. At both positive and negative sample bias the dark defect's negative charge would push the local bands up. At negative sample biases this enhances the overlap of the sample's filled states and the tip's empty states, thereby increasing the conductance. At positive sample biases this has the opposite effect. Crucially, however, it does not change the bias at which the current onsets at negative sample bias, because local band bending does not change the bias at which the Fermi level of the tip aligns with the bulk's valence band.

Previous authors have suggested that these dark defects could be boron atoms [129] or negatively charged As atoms [125]. The former is highly unlikely because the concentration we observe experimentally is much greater than we would expect from

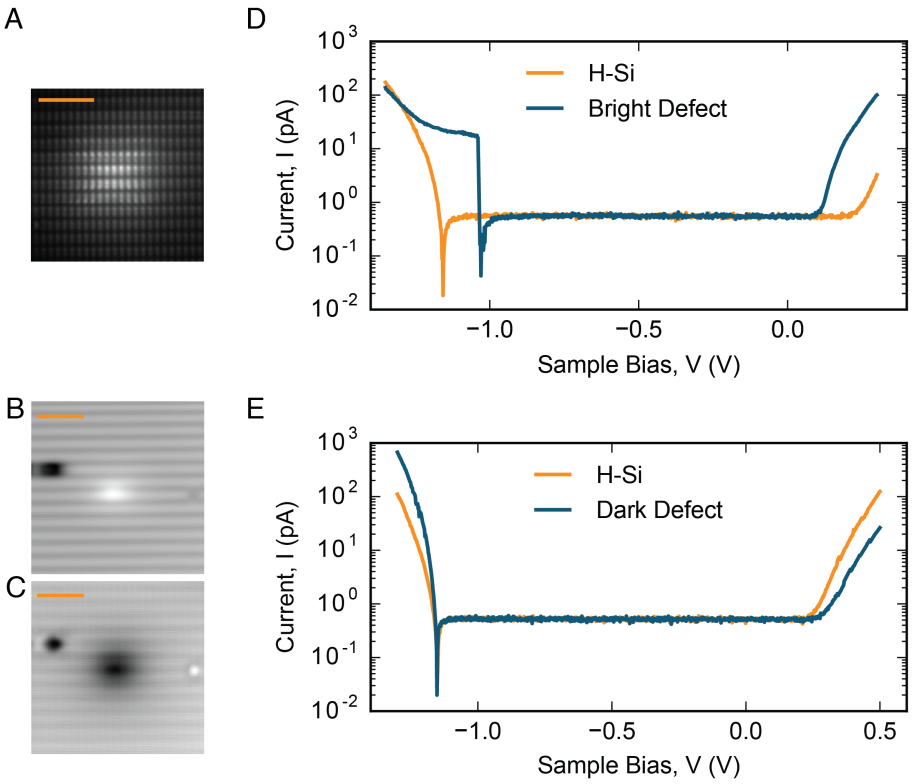

Figure 9.1: Characterization of dark and bright subsurface defects. **(A)** Constant height STM image of the bright defect acquired at $V = 300$ mV, $z = -250$ pm. The scale bar is 3 nm. **(B,C)** Constant current images of a dark defect obtained at -1.8 V and $+1.3$ V, respectively (50 pA). The scale bars are 2 nm. **(D)** A direct comparison of $I(V)$ spectra obtained above a bright defect and H-Si ($z = -350$ pm). **(E)** A direct comparison of $I(V)$ spectra obtained above a dark defect and H-Si ($z = -300$ pm).

a commercial grade Si sample (as suggested by Sinthiptharakoon *et. al.* [125]). Here we challenge the latter assignment by noting that our measurements above As donors suggest that the $As^{0/-}$ level is above the conduction band edge, or extremely close to it, such that the second electron would thermalize to the conduction band. We therefore suggest that these dark defects could also be negatively charged interstitial hydrogen atoms or subsurface silicon dangling bonds arising from a Si vacancy or an interstitial Si atom.

As a means of investigating dark defects we patterned DBs on the H-Si directly over them. Figure 9.2 demonstrates an interesting example. At 460 meV (Figure 9.2A) the DB appears as a small bright feature (high conductance) with the characteristic dark halo surrounding it. At 240 meV (Figure 9.2B) the conductance of the DB is similar to neighbouring H-Si and the halo has mostly disappeared. We note that the asymmetry in the appearance of the DB at this latter bias is unlikely due to an imperfect tip because similar features are not observed in the other atoms in the image. More likely, it is that the dark defect is not directly beneath the surface silicon atom.

Figure 9.2C shows $I(V)$ curves obtained on top of the DB at different tip offsets. As expected, as the tip approaches the sample the current increases exponentially. A notable and unexpected feature is the appearance of a peak at $\sim$ 375 meV. At small tip offsets this feature appears only as a shoulder on the $I(V)$ curve, but as the tip approaches the sample a local maximum and local minimum can be clearly differentiated. Figure 9.2D compares the currents of the local maxima and local minima over a range of tip offsets, and demonstrates that the visibility of the peak increases as the tip approaches the sample.

The decrease in tunnelling current as the bias is increased is a non-ohmic behaviour known as Negative Differential Resistance (NDR). Previously, our group has observed NDR on isolated DBs at negative biases [40]. In this case it was attributed to the complex interplay between the rate at which the $DB^{0/-}$ and $DB^{+/0}$ levels could be emptied by the tip and filled by the conduction and valence bands, but these explanations are completely unsuited to the phenomena observed in Figure 9.2. In this case, current is being injected into the DB by the tip, in which case the filling of the DB is almost certainly not rate limiting because the tip is extremely close to the

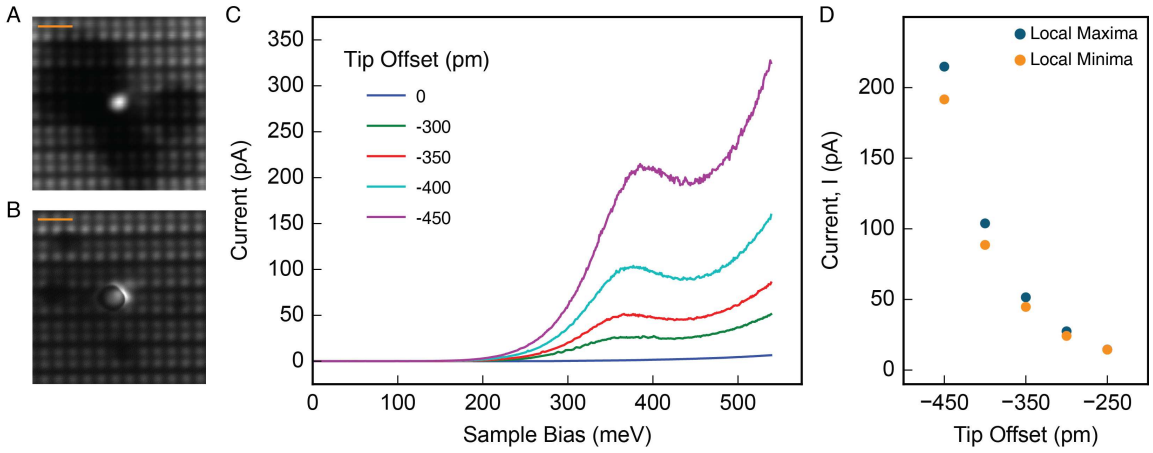

Figure 9.2: Negative differential resistance observed over a DB patterned close to a dark dopant. **(A)** Constant height STM image of the DB acquired at $V = 460$ mV, $z = -400$ pm. **(B)** Constant height STM image of the DB acquired at $V = 240$ mV, $z = -450$ pm. The scale bars are 1 nm. **(C)** $I(V)$ spectra acquired over the DB at different tip offsets. **(D)** The local minima (orange) and local maxima (blue) for the NDR features in (C) as a function of the tip offset.

sample.

Here we believe a simpler explanation of NDR is likely. At 0 V the Fermi level of the tip sits below the charge transition level of a mid gap state. As the bias is increased, the Fermi level of the tip becomes aligned with the state, which can be used as a stepping stone to source current to the conduction band. As the bias is increased further, the tip's Fermi level loses alignment with the mid gap state. Even though there are filled states of the tip aligned with the mid gap state, because tunnelling is elastic the electrons that can tunnel from the tip to the mid gap state nonetheless experience a larger barrier. As a result, the tunnelling current decreases until the tip can efficiently inject current directly into the conduction band. This explanation has been used to describe NDR in other material systems [130–132].

In the preceding discussion we referred to a mid-gap state, not the $DB^{0/-}$ level. Because we do not observe this NDR feature on typical DBs, we believe the mid gap state we sweep through is distinct from the $DB^{0/-}$ level we often refer to. Our explanation for this is as follows: the $DB^{0/-}$ level is very close in energy to the conduction band edge. When performing $I(V)$ spectroscopy on typical DBs we do not observe NDR at positive biases because when the Fermi level of the tip loses

alignment with the $DB^{0/-}$ level it can nevertheless efficiently inject current directly into the conduction band. Our observation of NDR therefore suggests that the mid gap state the Fermi level of the tip sweeps through must be lower in energy than the $DB^{0/-}$ level. One explanation for this is that the patterned DB hybridizes with the dark defect, creating a bonding state lower in energy than the $DB^{0/-}$ level. Further support of this explanation is that if this behaviour could be explained by a static shift of the local bands by a negatively charged defect, we would expect that DBs not patterned over dark defects would nonetheless occasionally display NDR at positive biases, due to local electrostatic perturbations. We do not observe this.

It is important to note that while we have observed this form of NDR several times it is not observed on every DB patterned directly on top of a dark defect. One possible explanation for this is that some dark defects are deeper below the surface than others and therefore cannot hybridize as strongly with the DB. Future investigators should compare the 'darkness' of these defects by measuring Δz in constant current mode, which may reveal a method to estimate their depth.

10 Conclusion and Outlook

The experiments described in this thesis are in many ways the natural extension of our group's recent experimental efforts. Empowered by the advances in STM H-lithography [28–30] we are becoming increasingly capable of studying precisely crafted DB structures.

The experiments presented in Chapters 5 - 7 advance our understanding of how AFM can be used to characterize DB structures, and several important conclusions can be drawn. First, the occupation of a structure may not correlate exactly with AFM images. This is because under appropriate conditions, the total band bending beneath the tip can become positive, thereby stabilizing charge in DBs beneath the tip. As a consequence, under these conditions the occupation of the structure will appear to be greater than it actually is. Fortunately we discovered that this is not simply a challenge, but can be utilized to our advantage. By dynamically switching between the *write* and *read* regimes we can prepare specific charge configurations of DB structures. Crucially, these charge states may remain stable for seconds, allowing us to observe them. This provides an opportunity to complete a host of interesting experiments that in the future may reveal more of the underlying physics of DB structures.

Our key priority for the future is to address the exact mechanism underlying the charge switching we observe. At this point it is clear that the tip likely plays a role, but further characterization is needed. Also of interest, but still largely unexplored, is to determine if there are correlations between the charge configurations of dangling bond structures. These relationships could exist between the configurations we observe in the *write* and *read* phases, but also between sequential states we observe in experiments restricted to the *read* regime, or among subunits of larger DB structures. The latter is of technological interest, as it suggests a method to determine the ideal repeating unit of a BASiL binary wire without having to build an extended structure.

The experiments presented in Section 8 demonstrate that the linescan map techniques developed in the previous chapters can be applied to technologically relevant problems. Specifically, they were used to assess the design and operation of a BASiL

logic gate. It is anticipated that these techniques can be used to help inform the design of future BASiL components.

Finally, the experiments presented in Section 9 present some of our ongoing efforts to fully characterize the H-Si surface. Opposing previous studies [126, 127] we suggest the steps seen at negative biases in $I(V)$ measurements taken over As donors correspond to the neutralization of additional donors, rather than the alignment of the tip's Fermi level with the $As^{0/-}$ level of a single donor. We have also continued to characterize dark defects, and suggest that they are likely negatively charged. Interestingly, we find that DBs patterned directly over these dark defects occasionally display negative differential resistance at positive biases, and we've presented a preliminary model to account for this behaviour. There is a clear potential for future time-resolved STM experiments to characterize any dynamics that may exist.

Bibliography

[1] Lucian Livadaru, Jason Pitters, Marco Taucer, and Robert A. Wolkow. Theory of nonequilibrium single-electron dynamics in STM imaging of dangling bonds on a hydrogenated silicon surface. *Physical Review B*, 84(20):205416, 2011.

[2] Taleana Huff, Hatem Labidi, Mohammad Rashidi, Roshan Achal, Lucian Livadaru, Thomas Dienel, Jason Pitters, and Robert A. Wolkow. Binary Atomic Silicon Logic. *arXiv*, 1706.07427, 2017.

[3] Mohammad Rashidi, Wyatt Vine, Thomas Dienel, Lucian Livadaru, Taleana Huff, Jacob Retallick, Konrad Walus, and Robert Wolkow. Initiating and monitoring the evolution of single electrons within atom-defined structures. *arXiv:1709.10091*, 2017.

[4] G. Binnig, H. Rohrer, Ch. Gerber, and E. Weibel. Tunneling through a controllable vacuum gap. *Applied Physics Letters*, 40(2):178–180, 1982.

[5] G. Binnig, H. Rohrer, Ch Gerber, and E. Weibel. 7x7 Reconstruction on Si(111) Resolved in Real Space. *Physical Review Letters*, 50(2):120–123, 1983.

[6] H. F. Hess, R. B. Robinson, R. C. Dynes, J. M. Valles, and J. V. Waszczak. Scanning-Tunneling-Microscope Observation of the Abrikosov Flux Lattice and the Density of States near and inside a Fluxoid. *Physical Review Letters*, 62(2):214–216, 1989.

[7] Christophe Berthod, Ivan Maggio-Aprile, Jens Bruér, Andreas Erb, and Christoph Renner. Observation of Caroli-de Gennes-Matricon Vortex States in YBa2Cu3O7-delta. *Physical Review Letters*, 119(23):237001, 2017.

[8] V Madhavan, W Chen, T Jamneala, and M F Crommie. Tunneling into a Single Magnetic Atom: Spectroscopic Evidence of the Kondo Resonance Tunneling into a Single Magnetic Atom : Spectroscopic Evidence of the Kondo Resonance. *Science*, 280:567–569, 1998.

[9] Taeyoung Choi, William Paul, Steffen Rolf-Pissarczyk, Andrew J. Macdonald, Fabian D. Natterer, Kai Yang, Philip Willke, Christopher P. Lutz, and Andreas J. Heinrich. Atomic-scale sensing of the magnetic dipolar field from single atoms. *Nature Nanotechnology*, 12:420–424, 2017.

[10] A. J. Heinrich, C. P. Lutz, J. A. Gupta, and D. M. Eigler. Molecule cascades. *Science*, 298(5597):1381–1387, 2002.

[11] Alexander Ako Khajetoorians, Jens Wiebe, Bruno Chilian, and Roland Wiesendanger. Realizing All-Spin Based Logic Operations Atom by Atom. *Science*, 332(6033):1062–1064, 2011.

[12] D. K. Schweizer and E. K. Eigler. Positioning single atoms with a scanning tunneling microscope, 1990.

[13] D. M. Eigler, C. P. Lutz, and W. E. Rudge. An atomic switch realized with the scanning tunnelling microscope. *Nature*, 352(6336):600–603, 1991.

[14] Martin Fuechsle, Jill A. Miwa, Suddhasatta Mahapatra, Hoon Ryu, Sunhee Lee, Oliver Warschkow, Lloyd C. L. Hollenberg, Gerhard Klimeck, and Michelle Y. Simmons. A single-atom transistor. *Nature Nanotechnology*, 7(4):242–246, 2012.

[15] H. C. Manoharan, C. P. Lutz, and D. M. Eigler. Quantum mirages formed by coherent projection of electronic structure. *Nature*, 403(6769):512–515, 2000.

[16] Robert Drost, Teemu Ojanen, Ari Harju, and Peter Liljeroth. Topological states in engineered atomic lattices. *Nature Physics*, 13:668–671, 2016.

[17] G. Binnig and C. F. Quate. Atomic Force Microscope. *Physical Review Letters*, 56(9):930–933, 1986.

[18] Franz J. Giessibl. Advances in atomic force microscopy. *Review of Modern Physics*, 75(3):949–983, 2003.

[19] C. Schonenberger and S. F. Alvarado. Single Charge Carriers by Force Microscopy. *Physical Review Letters*, 65(25):3162–3165, 1990.

[20] M. A. Eriksson, R. G. Beck, M. Topinka, J. A. Katine, R. M. Westervelt, K. L. Campman, and A. C. Gossard. Cryogenic scanning probe characterization of semiconductor nanostructures. *Applied Physics Letters*, 69(5):671–673, 1996.

[21] G. Finkelstein, P. I. Glicofridis, R. C. Ashoori, and M. Shayegan. Topographic Mapping of the Quantum Hall Liquid Using a Few-Electron Bubble. *Science*, 289(July):90–94, 2000.

[22] Michael T. Woodside and Paul L. McEuen. Scanned Probe Imaging of Single-Electron Charge States in Nanotube Quantum Dots. *Science*, 296(5570), 2002.

[23] Jascha Repp, Gerhard Meyer, Fredrik E Olsson, and Mats Persson. Controlling the charge state of individual gold adatoms. *Science*, 305(5683):493–495, 2004.

[24] Shadi Fatayer, Bruno Schuler, Wolfram Steurer, Ivan Scivetti, Jascha Repp, Leo Gross, Mats Persson, and Gerhard Meyer. Reorganization energy upon charging a single molecule on an insulator measured by atomic force microscopy. *Nature Nanotechnology*, 13:376–380, 2018.

[25] L. Gross, F. Mohn, P. Liljeroth, J. Repp, F. J. Giessibl, and G. Meyer. Measuring the Charge State of an Adatom with Noncontact Atomic Force Microscopy. *Science*, 324(5933):1428–1431, 2009.

[26] Wolfram Steurer, Shadi Fatayer, Leo Gross, and Gerhard Meyer. Probe-based measurement of lateral single-electron transfer between individual molecules. *Nature Communications*, 6:8353, 2015.

[27] M. Baseer Haider, Jason L. Pitters, Gino A. DiLabio, Lucian Livadaru, Josh Y. Mutus, and Robert A. Wolkow. Controlled Coupling and Occupation of Silicon Atomic Quantum Dots at Room Temperature. *Physical Review Letters*, 102(4):046805, 2009.

[28] Morten Moller, Samuel P. Jarvis, Laurent Guerinet, Peter Sharp, Richard Woolley, Philipp Rahe, and Philip Moriarty. Automated extraction of single H atoms with STM: Tip state dependency. *Nanotechnology*, 28(7):075302, 2017.

[29] Taleana R. Huff, Hatem Labidi, Mohammad Rashidi, Mohammad Koleini, Roshan Achal, Mark H. Salomons, and Robert A. Wolkow. Atomic White-Out: Enabling Atomic Circuitry through Mechanically Induced Bonding of Single Hydrogen Atoms to a Silicon Surface. *ACS Nano*, 11:8636–8642, 2017.

[30] Niko Pavliček, Zsolt Majzik, Gerhard Meyer, and Leo Gross. Tip-induced passivation of dangling bonds on hydrogenated Si(100)-2x1. *Appl. Phys. Lett.*, 111(053104):1–4, 2017.

[31] C. Julian Chen. *Introduction to Scanning Tunneling Microscopy.* Oxford University Press, Oxford, 2007.

[32] Alex D. Gottlieb and Lisa Wesoloski. Bardeen's tunnelling theory as applied to scanning tunnelling microscopy: a technical guide to the traditional interpretation. *Nanotechnology*, 17(8):R57–R65, 2006.

[33] J. Bardeen. Tunnelling from a Many-Particle Point of View. *Physical Review Letters*, 6(2):57–59, 1961.

[34] T. E. Feuchtwang. Tunneling theory without the transfer-Hamiltonian formalism. I. *Physical Review B*, 10(10):4121–4134, 1974.

[35] T. E. Feuchtwang. Tunneling theory without the transfer-Hamiltonian formalism. II. Resonant and inelastic tunneling across a junction of finite width. *Physical Review B*, 10(10):4135–4150, 1974.

[36] T. E. Feuchtwang. Tunneling theory without the transfer-Hamiltonian formalism. IV. The abrupt (zero-width) three-dimensional junction. *Physical Review B*, 13(2):517–530, 1976.

[37] J. B. Pendry, A. B. Pretre, and B. C. H. Krutzen. Theory of the scanning tunnelling microscope. *Journal of Physics: Condensed Matter*, 3(24):4313–4321, 1991.

[38] J. Tersoff and D. R. Hamann. Theory and Application for the Scanning Tunneling Microscope. *Physical Review Letters*, 50(25):1998–2001, 1983.

[39] B. C. Stipe, Robert J. Rezaei, and Ho. Single-Molecule Vibrational Spectroscopy and Microscopy. *Science*, 280(5370):1732–1735, 1998.

[40] Mohammad Rashidi, Marco Taucer, Isil Ozfidan, Erika Lloyd, Mohammad Koleini, Hatem Labidi, Jason L. Pitters, Joseph Maciejko, and Robert A. Wolkow. Time-Resolved Imaging of Negative Differential Resistance on the Atomic Scale. *Physical Review Letters*, 117(27):276805, 2016.

[41] T. R. Albrecht, P. Grütter, D. Horne, and D. Rugar. Frequency modulation detection using high-Q cantilevers for enhanced force microscope sensitivity. *Journal of Applied Physics*, 69(2):668–673, 1991.

[42] U. Dürig. Conservative and dissipative interactions in dynamic force microscopy. *Surface and Interface Analysis*, 27(5-6):467–473, 1999.

[43] P. Grütter, Y. Liu, P. LeBlanc, and U. Dürig. Magnetic dissipation force microscopy. *Applied Physics Letters*, 71(2):279, 1998.

[44] Winfried Denk and Dieter W. Pohl. Local electrical dissipation imaged by scanning force microscopy. *Applied Physics Letters*, 59(17):2171–2173, 1991.

[45] Franz J. Giessibl. Forces and frequency shifts in atomic-resolution dynamic-force microscopy. *Physical Review B - Condensed Matter and Materials Physics*, 56(24):16010–16015, 1997.

[46] U. Dürig, H. R. Steinauer, and N. Blanc. Dynamic force microscopy by means of the phase-controlled oscillator method. *Journal of Applied Physics*, 82(8):3641–3651, 1997.

[47] M. Nonnenmacher, M. P. O'Boyle, and H. K. Wickramasinghe. Kelvin probe force microscopy. *Applied Physics Letters*, 58(25):2921–2923, 1991.

[48] Wilhelm Melitz, Jian Shen, Andrew C. Kummel, and Sangyeob Lee. Kelvin probe force microscopy and its application. *Surface Science Reports*, 66(1):1–27, 2011.

[49] Leo Gross, Bruno Schuler, Fabian Mohn, Nikolaj Moll, Niko Pavliček, Wolfram Steurer, Ivan Scivetti, Konstantinos Kotsis, Mats Persson, and Gerhard Meyer.

Investigating atomic contrast in atomic force microscopy and Kelvin probe force microscopy on ionic systems using functionalized tips. *Physical Review B - Condensed Matter and Materials Physics*, 90(15):1–11, 2014.

[50] John A. Wood, Radovan Urban, Mark Salomons, Martin Cloutier, Robert A. Wolkow, and Jason L. Pitters. Iridium single atom tips fabricated by field assisted reactive gas etching. *Applied Surface Science*, 367:277–280, 2016.

[51] Hans-Werner Fink. Mono-atomic tips for scanning tunneling microscopy. *IBM Journal of Research and Development*, 30(5):460–465, 1986.

[52] Vu Thien Binh and J. Marien. Characterization of microtips for scanning tunneling microscopy. *Surface Science*, 202:L539–L549, 1988.

[53] Vu Thien Binh and N. García. On the electron and metallic ion emission from nanotips fabricated by field-surface-melting technique: experiments on W and Au tips. *Ultramicroscopy*, 42-44:80–90, 1992.

[54] K. Nagaoka, H. Fujii, K. Matsuda, M. Komaki, Y. Murata, C. Oshima, and T. Sakurai. Field emission spectroscopy from field-enhanced diffusion-growth nano-tips. *Applied Surface Science*, 182(1-2):12–19, 2001.

[55] A. I. Oliva, A. G. Romero, J. L. Peña, E. Anguiano, and M. Aguilar. Electrochemical preparation of tungsten tips for a scanning tunneling microscope Electrochemical preparation of tungsten tips for a scanning tunneling microscope. *Review of Scientific Instruments*, 67(5):1917–1921, 1996.

[56] Erwin W. Muller and Kanwar Bahadur. Field Ionization of Gases at a Metal Surface and the Resolution of the Field Ion Microscope. *Physical Review*, 102(3):624–631, 1956.

[57] Moh'd Rezeq, Jason Pitters, and Robert Wolkow. Tungsten nanotip fabrication by spatially controlled field-assisted reaction with nitrogen. *The Journal of Chemical Physics*, 124(20):204716, 2006.

[58] Erwin W. Muuller and Tien Tzou Tsong. *Field ion microscopy; principles and applications,*. American Elsevier Pub. Co, New York, 1969.

[59] Klaus D Rendulic and Zlatko Knor. Chemisorption and Gas-Promoted Field Evaporation. *Surface Science*, 7:205–214, 1967.

[60] Mohammad Rashidi and Robert A. Wolkow. Autonomous Scanning Probe Microscopy in-situ Tip Conditioning through Machine Learning. *arXiv*, 1803.07059, 2018.

[61] G. Binnig and D. P. E. Smith. Single-tube three-dimeonsional scanner for scanning tunneling microscopy. *Review of Scientific Instruments*, 57(8):1688–1689, 1986.

[62] Hewon Jung and Dae Gab Gweon. Creep characteristics of piezoelectric actuators. *Review of Scientific Instruments*, 71(4):1896–1900, 2000.

[63] John F. O'Hanlon. *A User's Guide to Vacuum Technology*. John Wiley & Sons, Inc., Hoboken, NJ, USA, 2003.

[64] Danial D. M. Wayner and Robert A. Wolkow. Organic modification of hydrogen terminated silicon surfaces. *Journal of the Chemical Society, Perkin Transactions 2*, 95(1):23–34, 2002.

[65] Franz J. Giessibl. High-speed force sensor for force microscopy and profilometry utilizing a quartz tuning fork. *Applied Physics Letters*, 73(26):3956, 1998.

[66] R. M. Tromp, R. J. Hamers, and J. E. Demuth. Si(001) Dimer Structure Observed with Scanning Tunneling Microscopy. *Physical Review Letters*, 55(12):1303–1306, 1985.

[67] Robert A. Wolkow. Direct observation of an increase in buckled dimers on Si(001) at low temperature. *Physical Review Letters*, 68(17):2636–2639, 1992.

[68] F. J. Morin and J. P. Maita. Electrical Properties of Silicon Containing Arsenic and Boron. *Physical Review*, 96(1):28–35, 1954.

[69] N.F. Mott and W.D. Twose. The theory of impurity conduction. *Advances in Physics*, 10(38):107–163, 1961.

[70] Jason L. Pitters, Paul G. Piva, and Robert A. Wolkow. Dopant depletion in the near surface region of thermally prepared silicon (100) in UHV. *Journal of Vacuum Science & Technology B*, 30(2):021806, 2012.

[71] Hatem Labidi, Marco Taucer, Mohammad Rashidi, Mohammad Koleini, Lucian Livadaru, Jason Pitters, Martin Cloutier, Mark Salomons, and Robert A Wolkow. Scanning tunneling spectroscopy reveals a silicon dangling bond charge state transition. *New Journal of Physics*, 17(7):073023, 2015.

[72] Mohammad Rashidi, Jacob A. J. Burgess, Marco Taucer, Roshan Achal, Jason L. Pitters, Sebastian Loth, and Robert A. Wolkow. Time-resolved single dopant charge dynamics in silicon. *Nature Communications*, 7:13258, 2016.

[73] F. Forstmann. The concepts of surface states. *Progress in Surface Science*, 42(1-4):21–31, 1993.

[74] M B Johnson and J M Halbout. Scanning Tunneling Microscopy and Spectroscopy for Studying Cross-Sectioned Si(100). *Journal of Vacuum Science & Technology B*, 10(1):508–514, 1992.

[75] Ch. Sommerhalter. Tunneling spectroscopy on semiconductors with a low surface state density. *Journal of Vacuum Science & Technology B: Microelectronics and Nanometer Structures*, 15(6):1876, 1997.

[76] Mohammad Rashidi, Wyatt Vine, Jacob A.J. Burgess, Marco Taucer, Roshan Achal, Jason L. Pitters, Sebastian Loth, and Robert A. Wolkow. All-electronic Nanosecond-resolved Scanning Tunneling Microscopy: Facilitating the Investigation of Single Dopant Charge Dynamics. *Journal of Visualized Experiments*, 131:e56861, 2018.

[77] S. M. Sze and Kwok Kwok Ng. *Physics of semiconductor devices*. Wiley-Interscience, 2007.

[78] R. M. Feenstra, Y. Dong, M. P. Semtsiv, and W. T. Masselink. Influence of tip-induced band bending on tunnelling spectra of semiconductor surfaces. *Nanotechnology*, 18(4):044015, 2007.

[79] Marco Taucer, Lucian Livadaru, Paul G. Piva, Roshan Achal, Hatem Labidi, Jason L. Pitters, and Robert A. Wolkow. Single-Electron Dynamics of an Atomic Silicon Quantum Dot on the H-Si(100)-(2x1) Surface. *Physical Review Letters*, 112(25):256801, 2014.

[80] Mohammad Rashidi, Erika Lloyd, Taleana R. Huff, Roshan Achal, Marco Taucer, Jeremiah J. Croshaw, and Robert A. Wolkow. Resolving and Tuning Carrier Capture Rates at a Single Silicon Atom Gap State. *ACS Nano*, 11:11732–11738, 2017.

[81] G. Binnig, N. Garcia, H. Rohrer, J. M. Soler, and F. Flores. Electron-metal-surface interaction potential with vacuum tunneling: Observation of the image force. *Physical Review B*, 30(8):4816–4818, 1984.

[82] Jason L. Pitters, Lucian Livadaru, M. Baseer Haider, and Robert A. Wolkow. Tunnel coupled dangling bond structures on hydrogen terminated silicon surfaces. *The Journal of Chemical Physics*, 134(6):064712, 2011.

[83] S. R. Schofield, P. Studer, C. F. Hirjibehedin, N. J. Curson, G. Aeppli, and D. R. Bowler. Quantum engineering at the silicon surface using dangling bonds. *Nature Communications*, 4:1649, 2013.

[84] John A Wood, Mohammad Rashidi, Mohammad Koleini, Jason L Pitters, and Robert A Wolkow. Multiple Silicon Atom Artificial Molecules. *arXiv*, page 1607.06050, 2016.

[85] Lucian Livadaru, Peng Xue, Zahra Shaterzadeh-Yazdi, Gino A. DiLabio, Josh Mutus, Jason L. Pitters, Barry C. Sanders, and Robert A. Wolkow. Dangling-bond charge qubit on a silicon surface. *New Journal of Physics*, 12(8):083018, 2010.

[86] M. Baseer Haider, Jason L Pitters, Gino A. DiLabio, Lucian Livadaru, Josh Y Mutus, and Robert A. Wolkow. Controlled Coupling and Occupation of Silicon Atomic Quantum Dots. *arXiv*, page 0807.0609, 2008.

[87] J. W. Lyding, T. Shen, J. S. Hubacek, J. R. Tucker, and G. C. Abeln. Nanoscale patterning and oxidation of H-passivated Si(100)-2x1 surfaces with an ultrahigh

vacuum scanning tunneling microscope. *Applied Physics Letters*, 64(118):2010 – 2012, 1994.

[88] R. S. Becker, G. S. Higashi, Y. J. Chabal, and A. J. Becker. Atomic-scale conversion of clean Si(111):H-1x1 to Si(111)-2x1 by electron-stimulated desorption. *Physical Review Letters*, 65(15):1917–1920, 1990.

[89] J. W. Lyding, T. C. Shen, G. C. Abeln, C. Wang, P. A. Scott, J. R. Tucker, Ph Avouris, and R. E. Walkup. Ultrahigh vacuum scanning tunneling microscope-based nanolithography and selective chemistry on silicon surfaces. *Israel Journal of Chemistry*, 36(1):3–10, 1996.

[90] Ph. Avouris, R.E. Walkup, A.R. Rossi, H.C. Akpati, P. Nordlander, T. C. Shen, G.C. Abeln, and J.W. Lyding. Breaking individual chemical bonds via STM-induced excitations. *Surface Science*, 363(1-3):368–377, 1996.

[91] Hatem Labidi, Mohammad Koleini, Taleana Huff, Mark Salomons, Martin Cloutier, Jason Pitters, and Robert A. Wolkow. Indications of chemical bond contrast in AFM images of a hydrogen-terminated silicon surface. *Nature Communications*, 8:14222, 2017.

[92] Supriyo Datta. *Quantum transport : atom to transistor*. Cambridge University Press, 2005.

[93] Leo P. Kouwenhoven, Gerd Schön, and Lydia L. Sohn. Introduction to Mesoscopic Electron Transport. In *Mesoscopic Electron Transport*, pages 105–214. Springer Netherlands, Dordrecht, 1997.

[94] Borislav Naydenov and John J. Boland. Engineering the electronic structure of surface dangling bond nanowires of different size and dimensionality. *Nanotechnology*, 24(27):275202, 2013.

[95] Mads Engelund, Nick Papior, Pedro Brandimarte, Thomas Frederiksen, Aran Garcia-Lekue, and Daniel Sánchez-Portal. Search for a Metallic Dangling-Bond Wire on n-Doped H-Passivated Semiconductor Surfaces. *The Journal of Physical Chemistry C*, 120(36):20303–20309, 2016.

[96] Marek Kolmer, Piotr Olszowski, Rafal Zuzak, Szymon Godlewski, Christian Joachim, and Marek Szymonski. Two-probe STM experiments at the atomic level. *J. Phys.: Condens. Matter*, 29:444004, 2017.

[97] Jason L. Pitters, Iana A. Dogel, and Robert A. Wolkow. Charge Control of Surface Dangling Bonds Using Nanoscale Schottky Contacts. *ACS Nano*, 5(3):1984–1989, 2011.

[98] C. S. Lent, P. D. Tougaw, W. Porod, and G. H. Bernstein. Quantum cellular automata. *Nanotechnology*, 4(1):49–57, 1993.

[99] N. Renaud and C. Joachim. Design and stability of NOR and NAND logic gates constructed with three quantum states. *Physical Review A*, 78(6):062316, 2008.

[100] Marek Kolmer, Rafal Zuzak, Ghassen Dridi, Szymon Godlewski, Christian Joachim, and Marek Szymonski. Realization of a quantum Hamiltonian Boolean logic gate on the Si(001):H surface. *Nanoscale*, 7:12325–12330, 2015.

[101] Zahra Shaterzadeh-Yazdi, Lucian Livadaru, Marco Taucer, Josh Mutus, Jason Pitters, Robert A. Wolkow, and Barry C. Sanders. Characterizing the rate and coherence of single-electron tunneling between two dangling bonds on the surface of silicon. *Physical Review B*, 89(3):035315, 2014.

[102] Zahra Shaterzadeh-Yazdi, Barry C. Sanders, and Gino A. DiLabio. Ab-initio characterization of coupling strength for all types of dangling-bond pairs on the hydrogen-terminated Si(100)-2x1 surface. *The Journal of Chemical Physics*, 148(15):154701, 2018.

[103] J. L. O'Brien, S. R. Schofield, M. Y. Simmons, R. G. Clark, A. S. Dzurak, N. J. Curson, B. E. Kane, N. S. McAlpine, M. E. Hawley, and G. W. Brown. Towards the fabrication of phosphorus qubits for a silicon quantum computer. *Physical Review B*, 64(16):161401, 2001.

[104] Y. Sugimoto, P. Pou, O. Custance, P. Jelinek, M. Abe, R. Perez, and S. Morita. Complex Patterning by Vertical Interchange Atom Manipulation Using Atomic Force Microscopy. *Science*, 322(5900):413–417, 2008.

[105] Marlou R. Slot, Thomas S. Gardenier, Peter H. Jacobse, Guido C. P. van Miert, Sander N. Kempkes, Stephan J. M. Zevenhuizen, Cristiane Morais Smith, Daniel Vanmaekelbergh, and Ingmar Swart. Experimental realization and characterization of an electronic Lieb lattice. *Nature Physics*, 13:672–676, 2016.

[106] Stefan Fölsch, Jesús Martínez-Blanco, Jianshu Yang, Kiyoshi Kanisawa, and Steven C. Erwin. Quantum dots with single-atom precision. *Nature Nanotechnology*, 9(7):505–508, 2014.

[107] F. E. Kalff, M. P. Rebergen, E. Fahrenfort, J. Girovsky, R. Toskovic, J. L. Lado, J. Fernández-Rossier, and A. F. Otte. A kilobyte rewritable atomic memory. *Nature nanotechnology*, 18:1–5, 2016.

[108] W. Steurer, J. Repp, L. Gross, I. Scivetti, M. Persson, and G. Meyer. Manipulation of the charge state of single au atoms on insulating multilayer films. *Physical Review Letters*, 114(3):1–5, 2015.

[109] Martin Sterrer, Thomas Risse, Umberto Martinez Pozzoni, Livia Giordano, Markus Heyde, Hans Peter Rust, Gianfranco Pacchioni, and Hans Joachim Freund. Control of the charge state of metal atoms on thin MgO films. *Physical Review Letters*, 98(9):1–4, 2007.

[110] Thomas Leoni, Olivier Guillermet, Hermann Walch, Véronique Langlais, Andrew Scheuermann, Jacques Bonvoisin, and Sébastien Gauthier. Controlling the charge state of a single redox molecular switch. *Physical Review Letters*, 106(21):4–7, 2011.

[111] Steven D. Bennett, Lynda Cockins, Yoichi Miyahara, Peter Grütter, and Aashish A. Clerk. Strong Electromechanical Coupling of an Atomic Force Microscope Cantilever to a Quantum Dot. *Physical Review Letters*, 104(1):017203, 2010.

[112] Liwei Liu, Thomas Dienel, Roland Widmer, and Oliver Gröning. Interplay between Energy-Level Position and Charging Effect of Manganese Phthalocyanines on an Atomically Thin Insulator. *ACS Nano*, 9(10):10125–10132, 2015.

[113] Fabian Schulz, Mari Ijäs, Robert Drost, Sampsa K. Hämäläinen, Ari Harju, Ari P. Seitsonen, and Peter Liljeroth. Many-body transitions in a single molecule visualized by scanning tunnelling microscopy. *Nature Physics*, 11(3):229–234, 2015.

[114] Sam Jarvis, Adam Sweetman, Joseph Bamidele, Lev Kantorovich, and Philip Moriarty. Role of orbital overlap in atomic manipulation. *Physical Review B - Condensed Matter and Materials Physics*, 85(23):1–5, 2012.

[115] F. E. Olsson, S. Paavilainen, M. Persson, J. Repp, and G. Meyer. Multiple Charge States of Ag Atoms on Ultrathin NaCl Films. *Physical Review Letters*, 98(17):176803, 2007.

[116] R. M. Feenstra. Electrostatic potential for a hyperbolic probe tip near a semiconductor. *Journal of Vacuum Science & Technology B: Microelectronics and Nanometer Structures*, 21(5):2080, 2003.

[117] Franz J. Giessibl. Atomic resolution on Si(111)-(7x7) by noncontact atomic force microscopy with a force sensor based on a quartz tuning fork. *Applied Physics Letters*, 76(11):1470, 2000.

[118] John E. Northrup. Effective correlation energy of a Si dangling bond calculated with the local-spin-density approximation. *Physical Review B*, 40(8):5875–5878, 1989.

[119] Hiroyo Kawai, Olga Neucheva, Tiong Leh Yap, Christian Joachim, and Mark Saeys. Electronic characterization of a single dangling bond on n- and p-type Si(001)-(2x1):H. *Surface Science*, 645:88–92, 2016.

[120] Romain Stomp, Yoichi Miyahara, Sacha Schaer, Qingfeng Sun, Hong Guo, Peter Grutter, Sergei Studenikin, Philip Poole, and Andy Sachrajda. Detection of Single-Electron Charging in an Individual InAs Quantum Dot by Noncontact Atomic-Force Microscopy. *Physical Review Letters*, 94(5):056802, 2005.

[121] John E. Sader and Suzanne P. Jarvis. Accurate formulas for interaction force and energy in frequency modulation force spectroscopy. *Applied Physics Letters*, 84(10):1801–1803, 2004.

[122] Joachim Welker, Esther Illek, and Franz J Giessibl. Analysis of force-deconvolution methods in frequency-modulation atomic force microscopy. *Beilstein journal of nanotechnology*, 3:238–48, 2012.

[123] K. Walus, T.J. Dysart, G.A. Jullien, and R.A. Budiman. QCADesigner: A Rapid Design and Simulation Tool for Quantum-Dot Cellular Automata. *IEEE Transactions On Nanotechnology*, 3(1):26–31, 2004.

[124] Lequn Liu, Jixin Yu, and J.W. Lyding. Subsurface dopant-induced features on the Si[100]2 1:H surface: fundamental study and applications. *IEEE Transactions On Nanotechnology*, 1(4):176–183, 2002.

[125] Kitiphat Sinthiptharakoon, Steven R. Schofield, Philipp Studer, Veronika Brázdová, Cyrus F. Hirjibehedin, David R. Bowler, and Neil J. Curson. Investigating individual arsenic dopant atoms in silicon using low-temperature scanning tunnelling microscopy. *Journal of Physics: Condensed Matter*, 26(1):012001, 2014.

[126] J. Salfi, J. A. Mol, R. Rahman, G. Klimeck, M. Y. Simmons, L. C. L. Hollenberg, and S. Rogge. Spatially resolving valley quantum interference of a donor in silicon. *Nature Materials*, 13(6):605–610, 2014.

[127] B. Voisin, J. Salfi, J. Bocquel, R. Rahman, and S. Rogge. Spatially resolved resonant tunneling on single atoms in silicon. *Journal of Physics-Condensed Matter*, 27(15):154203, 2015.

[128] E. Bussmann, M. Rudolph, G. S. Subramania, S. Misra, S. M. Carr, E. Langlois, J. Dominguez, T. Pluym, M. P. Lilly, and M. S. Carroll. Scanning capacitance microscopy registration of buried atomic-precision donor devices. *Nanotechnology*, 26(8):085701, 2015.

[129] Lequn Liu, Jixin Yu, and J. W. Lyding. Atom-resolved three-dimensional mapping of boron dopants in Si(100) by scanning tunneling microscopy. *Applied Physics Letters*, 78(3):386–388, 2001.

[130] J. Chen, M. A. Reed, A. M. Rawlett, and J. M. Tour. Large On-Off Ratios and Negative Differential Resistance in a Molecular Electronic Device. *Science*, 286:1550–1552, 1999.

[131] Yongqiang Xue, Supriyo Datta, Seunghun Hong, R. Reifenberger, Jason Henderson, and Clifford Kubiak. Negative differential resistance in the scanning-tunneling spectroscopy of organic molecules. *Physical Review B*, 59(12):R7852–R7855, 1999.

[132] M. Grobis, A. Wachowiak, R. Yamachika, and M. F. Crommie. Tuning negative differential resistance in a molecular film. *Applied Physics Letters*, 86(20):204102, 2005.